

## Simulations of interacting adsorbates

**Citation for published version (APA):**

Hermse, C. G. M. (2004). *Simulations of interacting adsorbates*. [Phd Thesis 1 (Research TU/e / Graduation TU/e), Chemical Engineering and Chemistry]. Technische Universiteit Eindhoven.  
<https://doi.org/10.6100/IR581077>

**DOI:**

[10.6100/IR581077](https://doi.org/10.6100/IR581077)

**Document status and date:**

Published: 01/01/2004

**Document Version:**

Publisher's PDF, also known as Version of Record (includes final page, issue and volume numbers)

**Please check the document version of this publication:**

- A submitted manuscript is the version of the article upon submission and before peer-review. There can be important differences between the submitted version and the official published version of record. People interested in the research are advised to contact the author for the final version of the publication, or visit the DOI to the publisher's website.
- The final author version and the galley proof are versions of the publication after peer review.
- The final published version features the final layout of the paper including the volume, issue and page numbers.

[Link to publication](#)

**General rights**

Copyright and moral rights for the publications made accessible in the public portal are retained by the authors and/or other copyright owners and it is a condition of accessing publications that users recognise and abide by the legal requirements associated with these rights.

- Users may download and print one copy of any publication from the public portal for the purpose of private study or research.
- You may not further distribute the material or use it for any profit-making activity or commercial gain
- You may freely distribute the URL identifying the publication in the public portal.

If the publication is distributed under the terms of Article 25fa of the Dutch Copyright Act, indicated by the "Taverne" license above, please follow below link for the End User Agreement:

[www.tue.nl/taverne](http://www.tue.nl/taverne)

**Take down policy**

If you believe that this document breaches copyright please contact us at:

[openaccess@tue.nl](mailto:openaccess@tue.nl)

providing details and we will investigate your claim.

# **SIMULATIONS OF INTERACTING ADSORBATES**

PROEFSCHRIFT

ter verkrijging van de graad van doctor  
aan de Technische Universiteit Eindhoven,  
op gezag van de Rector Magnificus,  
prof.dr. R.A. van Santen,  
voor een commissie aangewezen  
door het College voor Promoties  
in het openbaar te verdedigen  
op woensdag 1 december 2004 om 16.00 uur

door

**Chrétien Guillaume Maria Hermse**

geboren te Maastricht

Dit proefschrift is goedgekeurd door de promotoren:

prof.dr. R.A. van Santen  
en  
prof.dr. B.E. Nieuwenhuys

Copromotor:  
dr. A.P.J. Jansen

CIP-DATA LIBRARY TECHNISCHE UNIVERSITEIT EINDHOVEN

Hermse, Chrétien G. M.

Simulations of interacting adsorbates / by Chrétien G. M. Hermse. -  
Eindhoven : Technische Universiteit Eindhoven, 2004.  
Proefschrift. - ISBN 90-386-2716-5

NUR 913

Subject headings: surface chemistry / transition metal catalysts /  
adsorption ; lateral interaction / physicochemical simulation and  
modeling / density functional theory ; DFT / Monte Carlo simula-  
tion / reaction kinetics

Trefwoorden: oppervlaktechemie / overgangsmetaal-katalysatoren /  
adsorptie ; laterale interactie / fysisch-chemische simulatie en model-  
lering / dichtheidsfunctionaaltheorie ; DFT / Monte Carlo simulatie /  
reactiekinetiek

Printed at *Universiteitsdrukkerij*, Eindhoven University of Technology.

*The work described in this thesis has been carried out at the Schuit Institute of Catalysis (part of NIOK, the Netherlands School for Catalysis Research), Eindhoven University of Technology, The Netherlands. Financial support has been supplied by the Netherlands Research School Combination-Catalysis (NRSC-C).*

“I want to see the chieftains.  
I’ve brought omens from the desert.”  
*P. Coelho, The Alchemist*



# CONTENTS

1	INTRODUCTION	1
1.1	Models of molecules at surfaces . . . . .	1
1.2	Site approximation . . . . .	1
1.3	...and lateral interactions . . . . .	3
1.4	Catalysts . . . . .	4
1.5	Single crystal surfaces . . . . .	4
1.6	What we did . . . . .	4
2	METHODS	9
2.1	The lattice gas . . . . .	9
2.2	The chemical Master Equation . . . . .	12
2.3	Towards an algorithm . . . . .	13
2.4	The First Reaction Method . . . . .	16
2.5	Time-dependent transition probabilities . . . . .	17
2.6	Lateral interactions . . . . .	19
2.7	Other algorithms . . . . .	22
2.8	How to get transition probabilities . . . . .	24
2.9	Evolutionary Strategy optimisation . . . . .	24
3	ADSORPTION AND REACTION OF NO ON Rh(111)	33
3.1	Introduction . . . . .	33
3.2	Model and methods . . . . .	34
3.3	Calculation of the interactions . . . . .	38
3.4	Ordering of the NO adlayer . . . . .	42
3.5	Temperature programmed desorption . . . . .	46
3.6	Discussion . . . . .	53
3.7	Conclusions . . . . .	53
4	CHIRAL DOMAINS: TARTARIC ACID ON Cu(110)	57
4.1	Introduction . . . . .	57
4.2	Model and methods . . . . .	61
4.3	Determination of the important interactions . . . . .	67

vi CONTENTS

4.4	Ordering of the adlayer . . . . .	71
4.5	Discussion . . . . .	75
4.6	Conclusions . . . . .	77
5	MODELLING THE BUTTERFLY: BRIDGE-BOUND ANIONS	83
5.1	Introduction . . . . .	83
5.2	Model . . . . .	85
5.3	Linear sweep voltammetry and ordering . . . . .	88
5.4	Comparison to experiment . . . . .	103
5.5	Conclusions . . . . .	106
6	LATERAL INTERACTIONS AND MULTI-ISOTHERMS	111
6.1	Introduction . . . . .	111
6.2	Model . . . . .	112
6.3	Optimisation techniques . . . . .	119
6.4	The multi-isotherm . . . . .	121
6.5	Discussion . . . . .	132
6.6	Conclusions . . . . .	134
7	CONCLUDING REMARKS	139
7.1	Achievements . . . . .	139
7.2	Shortcomings . . . . .	140
7.3	Question marks . . . . .	141
7.4	Final thoughts . . . . .	141
	SUMMARY	143
	SAMENVATTING	145
	LIST OF PUBLICATIONS	147
	DANKWOORD	149
	CURRICULUM VITAE	151

# CHAPTER 1

## INTRODUCTION

### 1.1 MODELS OF MOLECULES AT SURFACES

In this thesis we are primarily interested in describing the kinetics of molecules on a well-defined surface; we want to know how they move around, interact, and react in each other's presence. We do this by simulating a system with a statistically significant number of molecules (at least one thousand) on a piece of the surface during experimental time scales (seconds to minutes). The dimension of the surface we simulate is schematically shown in the left part of Figure 1.1. In view of the size of our system we do not look at individual atoms, instead we take one step back. We take entire molecules to be the fundamental building blocks in our model, and we study their movement through time. This type of modelling, which efficiently describes large chunks of a material over longer periods, is generally referred to as mesoscale modelling [1–4]. These systems of molecules on surfaces are the subject of both experimental and theoretical research. Our mesoscopic models connect the fundamental microscopic events -movements of individual molecules- to the macroscopic properties, like coverages and reaction rates. These models enable us to validate assumptions regarding reaction mechanisms, and understand and sometimes even predict experimental behaviour.

### 1.2 SITE APPROXIMATION

The common way to describe adsorption on surfaces is based on the definition of sites. A site is a particular position with respect to the surface atoms where an adsorbate (adsorbed molecule) can chemisorb. Since an adsorbate strongly binds to its adsorption site, it usually resides there (Figure 1.2). Only occasionally does the adsorbate really leave that preferential position: it moves to a neighbouring similar position which also binds the adsorbate strongly, a neighbouring site [5, 6].

For a physisorbed (weakly bonding) adsorbate one does not expect great abso-



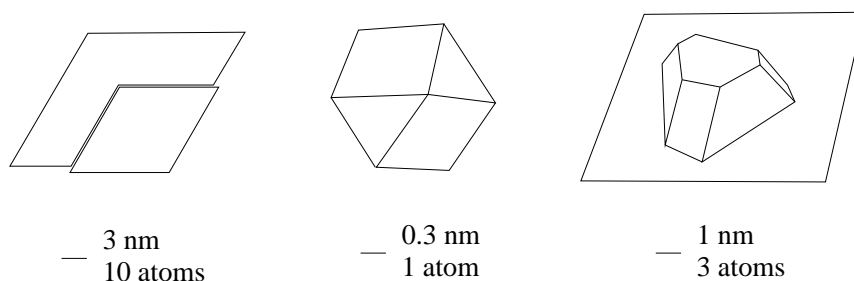


Figure 1.1: Left: part of the surface of a metal single crystal with a monatomic step. The entire single crystal typically measures 1 cm in diameter. Middle: tiny equilibrium-shaped metal particle. Right: larger metal particle on a support. The unsupported metal particle in the middle has a shape which is distinctly different from the shape of the supported one. Typical catalyst particles range between 1 and 100 nm in diameter.

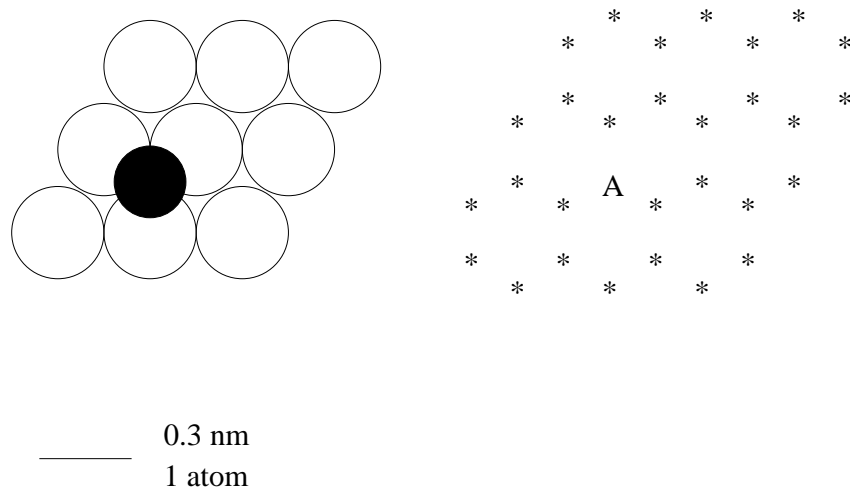


Figure 1.2: Left: close up view of a metal surface with an adsorbate (in black) binding between three metal atoms (in white). This position is referred to as a threefold site. Right: representation in our model of the system on the left in terms of unoccupied positions between three metal atoms (indicated with  $*$ ) and occupied positions (indicated by the A).

lute differences in the interaction of the adsorbate with the surface depending on its position on the surface. In this case the site approximation does not hold, since a weak interaction with the surface also implies that the binding energy does not vary much while travelling across the surface. Note that though the absolute difference in interaction energy is small, the relative difference in interaction energy may still be considerable.

For a more strongly bound adsorbate, like for example CO and NO, the stronger interaction with the surface implies a larger difference in binding energy for the various types of sites. This kind of adsorbate therefore preferentially resides at certain positions on the surface, and the site approximation holds. But the difference in bonding energy for the various types of sites is still reasonably small, and as a result one can still find the adsorbates in several types of sites.

There is a real preference for one type of site only when the interaction with the surface becomes really strong, like for nitrogen and oxygen atoms on the surface. This situation then conforms to the simple single-site lattice gas description of an adsorbate on a surface.

### 1.3 ...AND LATERAL INTERACTIONS

Unfortunately, there can be a contradiction in the model described, since while assuming that the site approximation holds people often assume there is no interaction between the adsorbates. We have just shown that the site approximation only really works if the interaction with the surface is strong. If the interaction with the surface is really strong, it is also very likely that the bonding of adsorbates close by is influenced by other adsorbates present, and that therefore through-surface lateral interactions do exist [7,8]. Secondly, the size of the adsorbed molecule usually is larger than the spacing between the sites on the surface. In addition to the through-surface interactions, this causes direct interactions between the molecules if they bind to neighbouring sites. These lateral adsorbate interactions may be attractive, causing the adsorbates to join and form islands of adsorbates. The lateral adsorbate interactions can also be repulsive, so that the adsorbates will tend to stay away from each other.

Thus, the fact that the site approximation holds, implies that there is a strong interaction with the surface. This, combined with the small spacing between the sites, implies that lateral adsorbate interactions are very likely to be present too. A complete description of adsorbates on surfaces includes more than adsorbates fixed on sites, since sites imply lateral interactions. For weakly bound adsorbates the site approximation does not hold and a continuum model is needed. Through-surface interactions can be neglected; the behaviour then is determined by direct adsorbate-adsorbate interactions only.

## 1.4 CATALYSTS

The relevance of these adsorbates-on-metal-surface systems lies in their relation to catalysts. Transition-metal-based catalysts consist of small metal particles dispersed on a high surface area support [9]. The surfaces of these particles are able to bond molecules strongly. Breaking bonds in a molecule normally is very difficult. The metal surface can stabilise the molecule during a bond-breaking process by forming strong molecule-metal bonds. A molecule adsorbed to the metal surface can therefore more easily be transformed into another molecule compared to being in the gas phase. The surface, after transformation of the molecule and desorption of the product, remains unaltered, and can therefore repeat the cycle. This process is referred to as catalysis [10–12].

The catalytic chemistry of supported catalysts is complicated [13, 14]. The small metal particles have different facets (with each a different surface structure) on which a reaction can take place [15–17]. The ratio of the size of the different facets present is influenced by the support and the adsorbates bonding to it (Figure 1.1, middle and right part), and may therefore change during the reaction [18–20]. The surface structure of a facet can be strained [21–23], reconstructed [24–29] or oxidised [30–32] under reaction conditions. It is also very common to use additional chemicals, called promoters, to improve the catalyst performance [33, 34].

## 1.5 SINGLE CRYSTAL SURFACES

The situation described above for real catalysts is far too complicated for study at a molecular level. If we want to better understand what happens with such surfaces that catalyse reactions, we need to characterise [35, 36] and simplify our catalyst [37, 38]. The usual approach is to eliminate the support and use only one type of surface, for example a single crystal surface. Because we now have a bare metal surface, we can also much more easily do measurements of the adsorbates on the surface. We do not have to probe through the support. Even more analysis techniques are available for studying the metal surface under vacuum conditions [36].

The downside of course is that by eliminating the support we can not investigate support effects. Neither do we know for certain that the surface we are studying is the one that is present and reactive in the real catalyst. Finally, by working under vacuum conditions we may be looking at a different surface than the actual one: the stable surface in the presence of high pressures of reactants may be different from the one found under vacuum conditions. These differences between ‘real’ and model catalysts are usually referred to as the materials and pressure gap [39, 40].

## 1.6 WHAT WE DID

In this thesis we extend the classic lattice gas description of non-interacting adsorbates on surfaces by including lateral adsorbate-adsorbate interactions. We discuss the ef-

fects of these interactions for three different single-crystal systems. The first system discusses nitrogen species on rhodium. Rhodium is commonly used to remove NO from automotive exhaust gases. The second system discusses the ordering of (*R,R*)-tartaric acid (a chiral molecule) on a metal surface. Preadsorption of this molecule has been used to perform enantioselective catalysis with ordinary heterogeneous catalysts. The final system involves the adsorption of the sulfate or bisulfate anion. This anion is commonly used as an electrolyte, and profoundly influences the electrochemical properties of the metal surface it binds to. In general, we show the influence of lateral adsorbate interactions for these systems on the type of site that is occupied by the adsorbate. Next to that, we show that lateral interactions can cause ordering of the adsorbates on the surface. Finally, we show how lateral adsorbate interactions influence reaction rates, like adsorption, desorption and dissociation. Welcome to my thesis.

## 6 REFERENCES

- [1] A. M. Stoneham and J. H. Harding; Not too big, not too small: the appropriate scale; *Nature Materials*, 2(2): 77–83, 2003.
- [2] J. H. Harding; Mesoscopic modelling; *Curr. Opin. Solid State and Mat. Sci.*, 2(6): 728–732, 1997.
- [3] F. Starrost and E. A. Carter; Modelling the full monty: baring the nature of surfaces across time and space; *Surf. Sci.*, 500(1–3): 323–346, 2002.
- [4] V. P. Zhdanov; Impact of surface science on the understanding of kinetics of heterogeneous catalytic reactions; *Surf. Sci.*, 500: 966–985, 2002.
- [5] R. I. Masel, editor; *Principles of Adsorption and Reaction on Solid Surfaces*; Wiley series in chemical engineering. Wiley, New York, 1996.
- [6] A. P. J. Jansen; An introduction to Monte Carlo simulations of surface reactions; <http://arXiv.org/>, paperno. cond-mat/0303028, 2003.
- [7] M. L. Merrick, W. Luo and K. A. Fichthorn; Substrate-mediated interactions on solid surfaces: theory, experiment, and consequences for thin-film morphology; *Progr. Surf. Sci.*, 72: 117–134, 2003.
- [8] J. K. Nørskov; *Coadsorption, promoters and poisons*, volume 6 of *The chemical physics of solid surfaces*, chapter 1 Adsorbate-adsorbate interactions on metal surfaces, pages 1–27; Elsevier, 1993.
- [9] Other materials often used in catalysis are metal oxides, metal sulfides and zeolites. In solution metal ions (usually in a metal-ligand complex) and peptides are used.
- [10] B. Lindström and L. J. Pettersson; A brief history of catalysis; *CATTECH*, 7(4): 130–138, 2003.
- [11] I. Chorkendorff and J. W. Niemantsverdriet; *Concepts of modern catalysis and kinetics*; Wiley-VCH, Weinheim, 2003.
- [12] E. G. Derouane; Catalysis in the 21st century - lessons from the past, challenges for the future; *CATTECH*, 5(4): 214–225, 2001.
- [13] M. Bowker, L. J. Bowker, R. A. Bennett, P. Stone and A. Ramirez-Cuesta; In consideration of precursor states, spillover and Boudart’s ‘collection zone’ and of their role in catalytic processes; *J. Molec. Catal. A*, 163: 221–232, 2000.
- [14] M. Bowker, R. D. Smith and R. A. Bennett; Anisotropic spillover from elongated particles; *Surf. Sci. Lett.*, 478: L309–L312, 2001.
- [15] Q. Ge and M. Neurock; Structure dependence of NO adsorption and dissociation on platinum surfaces; *J. Am. Chem. Soc.*, 126: 1551–1559, 2004.
- [16] H.-J. Freund, J. Libuda, M. Bäumer and A. Carlsson; Cluster, facets, and edges: site-dependent selective chemistry on model catalysts; *Chem. Rec.*, 3: 181–200, 2003.
- [17] D. P. Woodruff; Solved and unsolved problems in surface structure determination; *Surf. Sci.*, 500: 147–171, 2002.
- [18] T. Visart de Bocarmé, T. Bär and N. Kruse; Field ion microscopy study of the structural changes in Rh crystals during the reaction of oxygen-hydrogen gas mixtures; *Surf. Sci.*, 454–456: 320–325, 2000.
- [19] P. L. Hansen, J. B. Wagner, S. Helveg, J. R. Rostrup-Nielsen, B. S. Clausen and H. Topsoe; Atom-resolved imaging of dynamic shape changes in supported copper nanocrystals; *Science*, 295: 2053–2055, 2002.
- [20] H. Graoui, S. Giorgio and C. R. Henry; Shape variations of Pd particles under oxygen adsorption; *Surf. Sci.*, 417: 350–360, 1998.
- [21] M. S. Chen and D. W. Goodman; The structure of catalytically active Au on titania; Submitted, 2004.

- [22] A. Logadottir and J. K. Nørskov; The effect of strain for N<sub>2</sub> dissociation on Fe surfaces; *Surf. Sci.*, 489: 135–143, 2001.
- [23] N. Lopez, T. V. W. Janssens, B. S. Clausen, Y. Xu, M. Mavrikakis, T. Bligaard and J. K. Nørskov; On the origin of the catalytic activity of gold nanoparticles for low-temperature CO oxidation; *J. Catal.*, 223: 232–235, 2004.
- [24] S. Olivier, A. Saul and G. Treglia; Relation between surface stress and (1x2) reconstruction for (110) fcc transition metal surfaces; *Appl. Surf. Sci.*, 212–213: 866–871, 2003.
- [25] P. Broekmann, M. Wilms, A. Spaenig and K. Wandelt; Morphological aspects of sulfate-induced reconstruction of Cu(111) in sulfuric acid solution: in situ STM study; *Prog. Surf. Sci.*, 67: 59–77, 2001.
- [26] G. A. Somorjai; The flexible surface. Correlation between reactivity and restructuring ability.; *Langmuir*, 7: 3176–3182, 1991.
- [27] M. Bowker and R. A. Bennett; The flexible surface or the rigid surface?; *Topics in Catal.*, 14(1–4): 85–94, 2001.
- [28] Q. Chen and N. V. Richardson; Surface facetting induced by adsorbates; *Prog. Surf. Sci.*, 73: 59–77, 2003.
- [29] P. van Beurden, B. S. Bunnik and G. J. Kramer; Mechanism and dynamics of the CO-induced lifting of the Pt(100) surface reconstruction; *Phys. Rev. Lett.*, 90(6): 066106 1–4, 2003.
- [30] H. Over, Y. D. Kim, A. P. Seitsonen, S. Wendt, E. Lundgren, M. Schmid, P. Varga, A. Morgante and G. Ertl; Atomic-scale structure and catalytic reactivity of the RuO<sub>2</sub>(110) surface; *Science*, 287: 1474–1476, 2000.
- [31] M.-L. Bocquet, P. Sautet, J. Cerda, C. I. Carlisle, M. J. Webb and D. A. King; Specific ethene surface activation on silver oxide covered Ag(111) from the interplay of STM experiment and theory; *J. Am. Chem. Soc.*, 125: 3119–3125, 2003.
- [32] B. L. M. Hendriksen and J. W. M. Frenken; CO oxidation on Pt(110): scanning tunneling microscopy inside a high-pressure flow reactor; *Phys. Rev. Lett.*, 89(4): 046101 1–4, 2002.
- [33] J. J. Mortensen, B. Hammer and J. K. Nørskov; Alkali promotion of N<sub>2</sub> dissociation over Ru(0001); *Phys. Rev. Lett.*, 80(19): 4333–4336, 1998.
- [34] D. A. King and D. P. Woodruff, editors; *Coadsorption, promoters and poisons*, volume 6 of *The chemical physics of solid surfaces*; Elsevier, 1993.
- [35] J. H. G. J. Janssens; De waterstofadsorptie aan een chromoxide-silica katalysator; Master's thesis, Technische Hogeschool Eindhoven, 1972.
- [36] J. W. Niemantsverdriet; *Spectroscopy in catalysis: an introduction*; Wiley-VCH, Weinheim, second, completely revised edition, 2000.
- [37] H.-J. Freund, M. Bäumer and H. Kuhlenbeck; Catalysis and surface science: what do we learn from studies of oxide-supported cluster model systems?; *Adv. Catal.*, 45: 333–384, 2000.
- [38] J. H. Sinfelt; Role of surface science in catalysis; *Surf. Sci.*, 500(1–3): 923–946, 2002.
- [39] H.-J. Freund, H. Kuhlenbeck, J. Libuda, G. Rupprechter, M. Bäumer and H. Hamann; Bridging the pressure and materials gap between catalysis and surface science: clean and modified oxide surfaces; *Topics in Catal.*, 15(2–4): 201–209, 2001.
- [40] H.-J. Freund, N. Ernst, T. Risse, H. Hamann and G. Rupprechter; Models in heterogeneous catalysis: surface science quo vadis?; *Phys. Stat. Sol. (a)*, 187(1): 257–274, 2001.

## 8 REFERENCES

## CHAPTER 2

# METHODS

We introduce here the type of model used to simulate our systems of adsorbates on a surface, the so-called lattice-gas approximation. Next we introduce the Master Equation, which expresses the temporal evolution of a system in terms of a probability to find a system in some configuration, and transition probabilities which transform the current configuration into other configurations. Some kinetic Monte Carlo algorithms which are used to solve this Master Equation are then discussed, in connection to various forms of the transition probabilities.\* We end this chapter by discussing an algorithm which can be used to extract information on these transition probabilities from experiments.

### 2.1 THE LATTICE GAS

The size of the time step, and with this the computational cost, in simulations of the motion of atoms and molecules is determined by the fast vibrations of chemical bonds. Because the activation energy barriers of chemical reactions are generally much larger than the thermal energies, chemical reactions take place on a time scale that is many orders of magnitude larger. If one wants to study the kinetics of molecules on surfaces, then one needs a method that does away with the fast motions of these molecules.

The method that we present here does this by using the concept of *sites*. The forces working on an atom or a molecule that adsorbs on a surface force it to well-defined positions on the surface. These positions are called sites. They correspond to minima on the potential-energy surface for the adsorbate. Most of the time adsorbates stay very near these minima. Only when they diffuse from one site to another or during a reaction will they, for a very short time, not be near a minimum. Instead of specifying the precise positions, orientations and configurations of the adsorbates we will only specify for each site its occupancy. A reaction or a diffusion from one

---

\* This chapter is largely based on Ref. 1



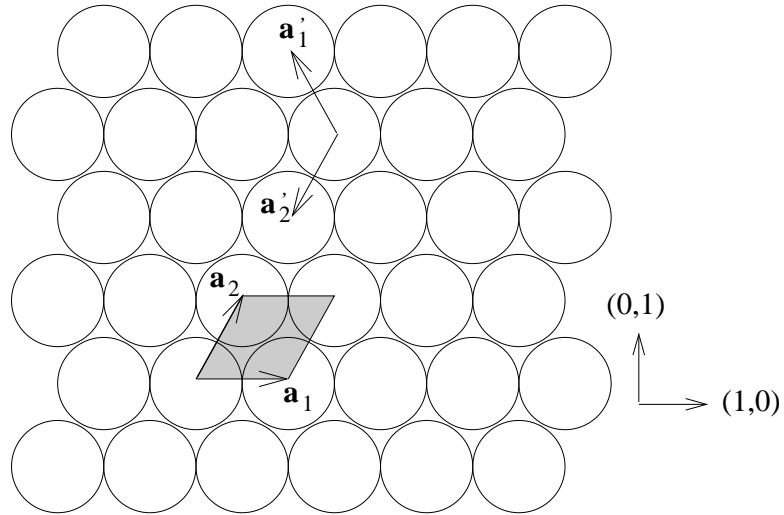


Figure 2.1: The (111) surface of an fcc metal. Different primitive vectors  $\mathbf{a}_1$ ,  $\mathbf{a}_2$ ,  $\mathbf{a}'_1$ , and  $\mathbf{a}'_2$  are indicated by the arrows. A unit cell is indicated in grey.

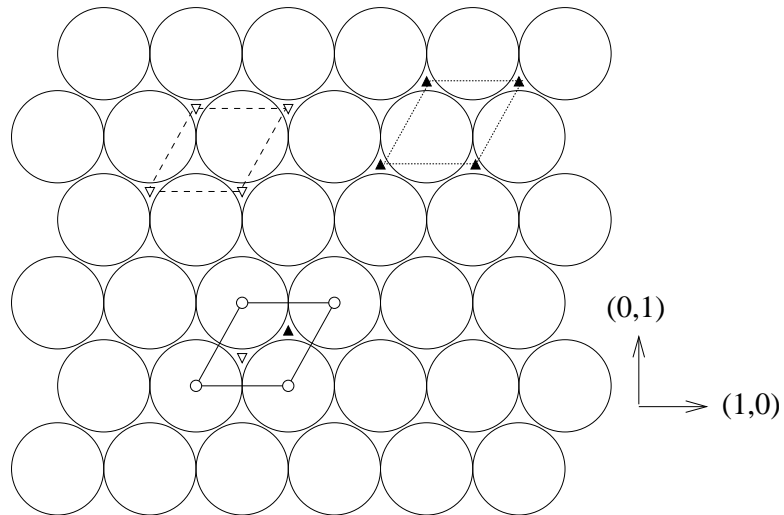


Figure 2.2: Different sites on the (111) surface of an fcc metal: on top (indicated by circles), fcc hollow (open triangles) and hcp hollow (filled triangles). Each site forms a sublattice with the same unit cell, they are only translated with respect to each other.

site to another will be modelled as a sudden change in the occupancy of the sites involved. Because the elementary events are now the reactions and the diffusion steps, the time that a system can be simulated is no longer determined by the fast motions of the adsorbates. The separation between the sites is larger than the amplitude of the vibrations of the adsorbed molecules. So we can simulate a much larger time scale by taking the separation between the sites as our fundamental (and therefore smallest) unit of length. Note that we have now eliminated not only the fast internal motions of the adsorbate, but also the surface-adsorbate vibrations and the vibrations of the surface.

If the surface has two-dimensional translational symmetry, or when it can be modelled as such, the sites form a regular grid or lattice. Our model is then a so-called *lattice-gas* model. If the surface has two-dimensional translational symmetry, then there are two vectors,  $\mathbf{a}_1$  and  $\mathbf{a}_2$ , with the property that when the surface is translated over one or both of these vectors the result is indistinguishable from the situation before translation. It is said that the system is *invariant* under translation over these vectors. The vectors  $\mathbf{a}_1$  and  $\mathbf{a}_2$  are called *primitive* vectors. In fact the surface is invariant under translation for any vector of the form

$$\mathbf{x} = n_1 \mathbf{a}_1 + n_2 \mathbf{a}_2, \quad (2.1)$$

where  $n_1$  and  $n_2$  are integers. These vectors are called the *lattice vectors*. The primitive vectors  $\mathbf{a}_1$  and  $\mathbf{a}_2$  are not uniquely defined. For example a (111) surface of an fcc metal (Figure 2.1) is translationally invariant for  $\mathbf{a}_1 = a(1, 0)$  and  $\mathbf{a}_2 = a(1/2, \sqrt{3}/2)$ , where  $a$  is the lattice spacing. But one can just as well choose  $\mathbf{a}_1 = a(-1/2, \sqrt{3}/2)$  and  $\mathbf{a}_2 = a(-1/2, -\sqrt{3}/2)$ . The area defined by

$$\mathbf{x} = x_1 \mathbf{a}_1 + x_2 \mathbf{a}_2, \quad (2.2)$$

with  $x_1, x_2 \in [0, 1)$  is called the *unit cell*. The whole system is retained by tiling the plane with the contents of a unit cell.

Expression 2.1 defines a *simple lattice*, *Bravais lattice*, or *net*. Simple lattices have just one lattice point, or grid point, per unit cell. It is also possible to have more than one lattice point per unit cell. The full lattice is then given by all

$$\mathbf{x} = \mathbf{x}_0^i + n_1 \mathbf{a}_1 + n_2 \mathbf{a}_2, \quad (2.3)$$

with  $i = 0, 1, \dots, (N_{\text{sub}} - 1)$ .  $N_{\text{sub}}$  is the number of lattice points per unit cell. Each  $\mathbf{x}_0^i$  is a different vector in the unit cell. The set  $\mathbf{x} = \mathbf{x}_0^i + n_1 \mathbf{a}_1 + n_2 \mathbf{a}_2$  for a particular value  $i$  forms a *sublattice*. This sublattice is a simple lattice, i.e., it has only one lattice point per unit cell. There are  $N_{\text{sub}}$  sublattices, and they all are equivalent; they are only translated with respect to each other.

Looking again at the (111) surface of an fcc metal (Figure 2.2), we see in the solid unit cell three lattice points indicated ( $N_{\text{sub}} = 3$ ): one on top of a metal atom (indicated by an open circle), and two in between three metal atoms (indicated by an open and filled triangle respectively). These are known as the fcc and hcp sites. As

indicated by the solid, dashed and dotted unit cell, these on top, fcc and hcp sites each form a simple lattice, and their unit cells are identical in size and shape, but translated with respect to each other. If we choose the first sublattice ( $i = 0$ ) to be the one of the on top sites and assign it  $\mathbf{x}_0^0 = (0, 0)$ . This yields for the fcc site ( $i = 1$ ) the vector  $\mathbf{x}_0^1 = (1/2, \sqrt{3}/6)$  and for the hcp site ( $i = 2$ ) the vector  $\mathbf{x}_0^2 = (1, \sqrt{3}/3)$ .

We assign a *label* to each lattice point. The lattice points correspond to the sites on the surface, and the labels specify the the properties of the sites. The most common property that one wants to describe with the label is occupancy of the site. For example, the short-hand notation  $(n_1, n_2/s : A)$  can be interpreted as that the site of sublattice  $s$  at position  $\mathbf{x}_0^s + n_1\mathbf{a}_1 + n_2\mathbf{a}_2$  is occupied by a molecule A. The labels can also be used to specify the reactions. A reaction is nothing but a change in the labels. An extension to the short-hand notation  $(n_1, n_2/s : A \rightarrow B)$  indicates that during a reaction the occupancy of the site at  $\mathbf{x}_0^s + n_1\mathbf{a}_1 + n_2\mathbf{a}_2$  changes from A to B. If more than one site is involved in a reaction then the specification will consist of a set of changes of the form  $(n_1, n_2/s : A \rightarrow B)$ . A lattice with labels for all its lattice points is called a *configuration*; a reaction transforms one configuration into another one.

The lattice-gas model is simple yet very powerful, as it allows us to model a large variety of systems and phenomena. Yet not everything can be modelled with it. If the surface reconstructs, it can not be described by a single ordered lattice. This is the case at high temperatures or when the surface atoms have very low coordination. Also, if the adsorbates do not reside in sites, but may bind at any position on the surface, the lattice-gas does not work. The second case is referred to as *incommensurate adsorption*, and is generally related to a small interaction of the adsorbate with the surface, yielding also a small corrugation of the potential energy surface. In that case the interactions between the adsorbates can be comparable to or larger than the differences in binding energies at different positions on the surface. This causes the position of the adsorbate not to be at a certain specific site, but to be determined by the packing with neighbouring adsorbates.

## 2.2 THE CHEMICAL MASTER EQUATION

The evolution of a system as a function of (real) time can be described by means of the chemical Master Equation, which can be derived from first principles [2, 3]:

$$\frac{dP_\alpha}{dt} = \sum_{\beta \neq \alpha} [W_{\alpha\beta}P_\beta - W_{\beta\alpha}P_\alpha]. \quad (2.4)$$

In this set of equations,  $P_\alpha$  denotes the probability to find the system in configuration  $\alpha$  at time  $t$ ;  $W_{\alpha\beta}$  is the transition probability per unit time of the reaction that transfers configuration  $\beta$  into  $\alpha$ . These transition probabilities per unit time in our case specify the rate at which the layer of adsorbates on the surface changes due to reactions. The Master Equation is a gain-loss equation. The first term on the right stands for increases in  $P_\alpha$  due to reactions that change other configurations  $\beta$  into the configuration  $\alpha$  of the adsorbates on the surface. The second term stands for all reactions that convert the

current configuration  $\alpha$  of the adsorbates on the surface into some other configuration  $\beta$ .

The Master Equation can be derived from first principles (as shown elsewhere [2]), and hence forms a solid base for all subsequent work. Many different Monte Carlo algorithms are known. Those that are derived from the Master Equation give necessarily results that are statistically identical. Those that cannot be derived from the Master Equation conflict with first principles and should be discarded. The Monte Carlo algorithms below are one way to solve the Master Equation, but there are also other ways. The Master Equation can, for example, also be used to derive the macroscopic rate equation. For most systems of interest, however, it is impossible to derive analytical results from the Master Equation without making approximations. For these systems one can resort to Monte Carlo simulations to get a statistically correct solution.

## 2.3 TOWARDS AN ALGORITHM

The idea of the kinetic Monte Carlo method (also known as the dynamic Monte Carlo method) is not to compute the probabilities  $P_\alpha(t)$  explicitly, but to start with some particular configuration, representative for the initial state of the experiment one wants to simulate, and then generate a sequence of other configurations with the correct probability. The Master Equation expresses the probabilities as a function of time.

What we need are typical times for a reaction to take place. To get an expression for these typical times we leave the general case for many configurations  $\alpha$  and many possible reactions described by the Master Equation. We restrict ourselves to deriving a solution for only one configuration  $a$ , and only one reaction  $a \rightarrow b$  that transforms the current configuration  $a$  in an other configuration  $b$ . The Master Equation then simplifies to

$$\frac{dP_a}{dt} = -W_{ba}P_a. \quad (2.5)$$

This is the equation we are going to invert to get typical times for a reaction. So if we are currently at time  $t$  we can determine the chance that at time  $t_{ba}$  we are still in configuration  $a$  by solving

$$P_a(t_{ba}) = \exp \left[ - \int_t^{t_{ba}} W_{ba}(t') dt' \right]. \quad (2.6)$$

The solution for time-independent  $W_{ba}$  is discussed first. The more general case where  $W_{ba}$  is time dependent is slightly more difficult, and will be discussed further on. If the transition probability  $W_{ba}$  is time-independent, the equation can be solved analytically. The solution is

$$P_a(t_{ba}) = \exp[-W_{ba}(t_{ba} - t)]. \quad (2.7)$$

This gives the chance that at  $t_{ba}$  we are still in configuration  $a$ . The chance that at  $t_{ba}$  the system has reacted and is now in configuration  $b$  is given by:

$$P_b(t_{ba}) = 1 - P_a(t_{ba}) \quad (2.8)$$

$$= 1 - \exp[-W_{ba}(t_{ba} - t)], \quad (2.9)$$

since the system in our example is either in configuration  $a$  or in configuration  $b$ . If we rewrite this equation, we can get the average time for the reaction  $a \rightarrow b$  when the chance that the reaction has occurred equals  $P_b$ :

$$t_{ba}(P_b) = t - \frac{1}{W_{ba}} \ln(-P_b + 1) \quad (2.10)$$

We have now inverted Eqn. 2.5, which expresses a probability in time, into an equation that expresses a time in a probability. This expression writes the average time till the reaction occurs  $t_{ba}$  as a function of the probability  $P_b$  that the system is in state  $b$ . The domain of the function is  $P_b \in [0, 1]$ . The range of the function is  $t_{ba} \in [t, \infty)$ , given that  $W_{ba}$  is real and non-zero. Eqn. 2.10 may seem odd at first, but the characteristic (chance-averaged) time for the reaction  $a \rightarrow b$  produced by this expression still is

$$\tau_{ba} = \frac{1}{W_{ba}}. \quad (2.11)$$

This result can be obtained by determining the average of  $t_{ba} - t$  over  $P_b$ :

$$\tau_{ba} = \int_0^1 ((t_{ba}(P_b) - t) dP_b \quad (2.12)$$

$$= \int_0^1 \left(-\frac{1}{W_{ba}} \ln(-P_b + 1)\right) dP_b \quad (2.13)$$

$$(2.14)$$

Substituting  $P_b$  by  $x = (1 - P_b)$  yields

$$\tau_{ba} = \frac{1}{W_{ba}} \int_1^0 \ln(x) dx \quad (2.15)$$

which can be integrated to

$$\tau_{ba} = \frac{1}{W_{ba}} [x \ln(x) - x]_{x=1}^{\lim_{x \rightarrow 0^+}} \quad (2.16)$$

We can get the value of the limit  $\lim_{x \rightarrow 0^+} x \ln(x)$  by rewriting

$$\lim_{x \rightarrow 0^+} x \ln(x) = \lim_{x \rightarrow 0^+} \frac{\ln(x)}{\frac{1}{x}} \quad (2.17)$$

$$= \lim_{x \rightarrow 0^+} \frac{f(x)}{g(x)}. \quad (2.18)$$

Since  $f(x)$  and  $g(x)$  respectively go to minus and plus infinity for  $x \rightarrow 0^+$ , we can invoke the rule of de l'Hospital and write:

$$\lim_{x \rightarrow 0^+} \frac{f(x)}{g(x)} = \lim_{x \rightarrow 0^+} \frac{f'(x)}{g'(x)} \quad (2.19)$$

$$= \lim_{x \rightarrow 0^+} \frac{\frac{1}{x}}{-\frac{1}{x^2}} \quad (2.20)$$

$$= \lim_{x \rightarrow 0^+} -x = 0 \quad (2.21)$$

Filling in this limit in Eqn. 2.16 leads to

$$\tau_{ba} = \frac{1}{W_{ba}} [(0 - 0) - (0 - 1)] = \frac{1}{W_{ba}}. \quad (2.22)$$

This is exactly what we expected.

In a Monte Carlo simulation we do not want to look at average times, but at a single time for one single reaction  $a \rightarrow b$ . This time has a certain probability distribution. We can generate such times by taking a uniform random number  $r$  on the interval  $[0,1]$  and equating this to the probability that the reaction has occurred; i.e.,

$$r = P_b, \quad (2.23)$$

and then calculating the corresponding time according to Eqn. 2.10

$$t_{ba} = t - \frac{1}{W_{ba}} \ln(-r + 1). \quad (2.24)$$

$r$  is a random number on the interval  $[0,1]$ , so  $-r + 1$  is an other random number on the same interval. We can therefore replace  $-r + 1$  by  $r$  and write

$$t_{ba} = t - \frac{1}{W_{ba}} \ln(r). \quad (2.25)$$

The reasoning above shows that for one single reaction  $a \rightarrow b$  we can generate a tentative time  $t_{ba}$ . The derivation above does not prove that if there are more reactions  $a \rightarrow c$ ,  $a \rightarrow d$  we can generate independently tentative times  $t_{ca}$ ,  $t_{da}$ . Neither is the equation above a general solution to the Master Equation, since we have confined ourselves to a single configuration  $a$  and a single reaction  $a \rightarrow b$ . The proof that different tentative times can be generated independently and that the times generated by Eqn. 2.25 yield an evolution of the system that obeys the general Master Equation is reported elsewhere [4]. Based on this proof we can write

$$t_{\beta\alpha} = t - \frac{1}{W_{\beta\alpha}} \ln(r) \quad (2.26)$$

for the time-independent case, even if more reactions  $\alpha \rightarrow \beta'$ ,  $\alpha \rightarrow \beta''$  are possible, and we can also generate tentative times  $t_{\beta'\alpha}$  and  $t_{\beta''\alpha}$  for these reactions. The actual reaction that will take place is the one with the smallest tentative time. For the new configuration one can again determine all possible reactions, calculate the tentative times, and perform the reaction with the smallest tentative time. In this way we can describe the evolution of our system as a function of time.

## 2.4 THE FIRST REACTION METHOD

The method of generating for each reaction a tentative time, performing the reaction with the smallest tentative time and thus describing the evolution of a system is known as the First Reaction Method. A more detailed description of the algorithm is given below [1].

### 1. Initialise

Generate an initial configuration  $\alpha$ .

Set the time  $t$  to some initial value.

Make a list  $L_{rx}$  containing all reactions.

Generate for each reaction  $\alpha \rightarrow \beta$  in  $L_{rx}$  a time of occurrence

$$t_{\beta\alpha} = t - \frac{1}{W_{\beta\alpha}} \ln(r),$$

with  $W_{\beta\alpha}$  the rate constant for the reaction and  $r$  a random deviate on the unit interval.

Choose conditions when to stop the simulation.

### 2. Reaction

Take the reaction  $\alpha \rightarrow \alpha'$  with  $t_{\alpha'\alpha} \leq t_{\beta\alpha}$  for all  $\beta$ .

If the reaction is possible go to step 3. If not go to step 4.

### 3. Enabled update

Change the configuration to  $\alpha'$ .

Change the time to  $t \rightarrow t_{\alpha'\alpha}$ .

Remove the reaction  $\alpha \rightarrow \alpha'$  from  $L_{rx}$ .

Add new enabled reactions to  $L_{rx}$  and generate for each reaction  $\alpha' \rightarrow \beta$  a time of occurrence

$$t_{\beta\alpha'} = t - \frac{1}{W_{\beta\alpha'}} \ln(r).$$

Skip to step 5.

### 4. Disabled update

Do not change the configuration:  $\alpha'$  is the same as  $\alpha$ .

Remove the disabled reaction from  $L_{rx}$ .

### 5. Continuation

If the stop conditions are fulfilled then stop.

If not set  $\alpha$  to  $\alpha'$  and repeat at step 2.

This algorithm is called Discrete Event Simulation in computer science. The bottleneck of the First Reaction Method is the determination of the reaction with the smallest time of occurrence. Scanning a list of all reactions for each new reaction scales as  $O(S)$ , where  $S$  is the length of the list. More efficient is to make the list of

all reactions an ordered one, and keep it ordered during a simulation. Getting the next reaction scales then as  $O(1)$ , but inserting reactions in  $L_{rx}$  scales as  $O(\log S)$ . This is not as good as constant time, but not particularly bad either.

When a reaction has been performed, the reaction list has to be updated. Some new reactions have become possible, and these reactions together with their times have to be added to the list. Many other reactions were possible in the old configuration, and are still possible in the new configuration, since a reaction usually only changes a configuration locally. The entries for these reactions in the reaction list can be maintained. Some reactions which were possible in the old configuration are not possible anymore in the new configuration. These reactions are referred to as *disabled*. Removing these disabled reactions from the reaction list requires searching through the entire list, which is computationally expensive ( $O(S)$ ). If, instead, we leave these disabled reactions in the reaction list, and remove them when we encounter them, the algorithm is much more efficient. We then need to check whether the reaction in the reaction list is still enabled (possible) before we perform it. This check is implemented in point 2 of the algorithm.

Also note that that we only have to generate the reaction times for the new enabled reactions. Times for reactions already in  $L_{rx}$  need not be generated again. This can be seen by considering the following. Suppose that at time  $t = t_1$  a time has been generated for a reaction with rate constant  $W$ . The probability distribution for that time is  $W \exp[-W(t - t_1)]$ . Now assume that at time  $t = t_2 > t_1$  the reaction has not occurred. We might generate a new time using the new probability distribution  $W \exp[-W(t - t_2)]$ . However, the ratio of the values of these probability distributions for times  $t > t_2$  is  $W \exp[-W(t - t_2)] / W \exp[-W(t - t_1)] = \exp[W(t_2 - t_1)]$  is a constant. Hence relative probabilities for the times  $t > t_2$  that the reaction can occur are the same for both probability distributions, and no new time need to be generated.

## 2.5 TIME-DEPENDENT TRANSITION PROBABILITIES

The determination of a tentative time in the case of time-dependent transition probabilities  $W_{\beta\alpha}$  amounts to solving

$$r = \exp \left[ - \int_t^{t_{\beta\alpha}} W_{\beta\alpha}(t') dt' \right]. \quad (2.27)$$

This can be seen by realising that for the time-independent case we equated the probability that a reaction has occurred  $P_b$  to a random number  $r$ ,

$$r = P_b, \quad (2.23)$$

expressed  $P_b$  in  $P_a$

$$P_b(t_{ba}) = 1 - P_a(t_{ba}), \quad (2.8)$$

and determined  $P_a$  by integrating the transition probability over the time:

$$P_a(t_{ba}) = \exp \left[ - \int_t^{t_{ba}} W_{ba}(t') dt' \right]. \quad (2.6)$$



Combining these three equations yields

$$-r + 1 = \exp \left[ - \int_t^{t_{ba}} W_{ba}(t') dt' \right], \quad (2.28)$$

where  $-r + 1$  can again be replaced by  $r$ , and the result can be proven to be valid as well for many reactions and configurations, yielding equation 2.27. Whether Eqn. 2.27 can be solved depends entirely on the form of  $W_{\beta\alpha}(t)$ . As an example, the transition probability for adsorption on a surface may be modulated by playing with the gas phase reactant pressure.

Common experiments to study adsorption, desorption and reaction on surfaces include temperature-programmed desorption and reaction, and cyclic voltammetry. In temperature-programmed desorption and reaction experiments, the temperature is linearly increased with time

$$T = T_0 + Bt'. \quad (2.29)$$

Here  $T_0$  is the temperature at  $t' = 0$  s and  $B$  is the heating rate in K/s. If the transition probability is given in the form of an Arrhenius-like rate constant [5]

$$W_{\beta\alpha} = \nu \exp \left[ - \frac{E_{act}}{RT} \right], \quad (2.30)$$

with  $E_{act}$  an activation energy,  $\nu$  a pre-exponential factor and  $R$  the gas constant, then the integral to be solved in equation 2.27 becomes

$$\int_t^{t_{\beta\alpha}} \nu \exp \left[ - \frac{E_{act}}{R(T_0 + Bt')} \right] dt' = \Omega(t_{\beta\alpha}) - \Omega(t) \quad (2.31)$$

where

$$\Omega(t') = \frac{\nu}{B} (T_0 + Bt') E_2 \left( \frac{E_{act}}{R(T_0 + Bt')} \right), \quad (2.32)$$

where  $E_2(\chi)$  is an exponential integral of second order with argument  $\chi$ :

$$E_2(\chi) = \int_1^\infty \frac{\exp(-\chi t')}{t'^2} dt'. \quad (2.33)$$

Expressed in  $\Omega(t')$ , the equation to be solved becomes

$$\Omega(t_{\beta\alpha}) = \Omega(t) - \ln(r). \quad (2.34)$$

Standard methods, such as the Newton-Rhapson method, can be used to solve this equation [6].

In cyclic voltammetry experiments, the potential of the surface is linearly increased with time

$$\Phi = \Phi_0 + Ct'. \quad (2.35)$$

Here  $\Phi_0$  is the potential at  $t' = 0$  s and  $C$  is the sweep rate in V/s. The transition probability for a reaction that involves the transfer of an electron has the form

$$W_{\beta\alpha} = k_0 \exp[-D\Phi], \quad (2.36)$$

with  $k_0$  the transition probability at zero potential and  $D$  a constant determined by a so-called transfer coefficient, the number of electrons that are transferred, and the temperature.  $D$  can be negative or positive, depending on whether an electron is transferred from the adsorbate to the surface or the other way around. If  $D$  is negative, the transition probability increases with time, and a time  $t_{\beta\alpha}$  can be determined for any value of the random number  $r$ .

Interestingly, if  $D$  is positive, the transition probability decreases with time. Eqn. 2.27 may in that case have no solution  $t_{\beta\alpha}$  for certain values of  $r$ . The reason for this is that the integral in Eqn. 2.27 does not go to infinity for  $D > 0$ . The physical interpretation of the observation that Eqn. 2.27 has no solution  $t_{\beta\alpha}$  for certain values of  $r$  is that there is a finite probability that the reaction will never occur. Eqn. 2.27 only has a solution for any value of  $r$  if the integral goes to infinity. This is the case when  $W_{\beta\alpha}$  goes slower to zero than  $1/t$ , or does not go to zero at all.

If the integration in Eqn. 2.27 is not easy to solve, then one may attempt to approximate  $t_{\beta\alpha}$  by taking  $W_{\beta\alpha}$  constant for a small time step  $\delta t$ . If the reaction occurs within the small time step  $\delta t$ , then the time is updated to  $t_{\beta\alpha}^{\text{appr}}$ , where  $t_{\beta\alpha}^{\text{appr}}$  is now an approximate value of the ‘real’  $t_{\beta\alpha}$ . If the reaction has not taken place within the small time step, and is still enabled, then one can redetermine the value for the transition probability for this time  $W_{\beta\alpha}(t + \delta t)$  and generate a new estimate for the tentative time  $t_{\beta\alpha}^{\text{appr}}$ . This approach can be used if the time scale on which the transition probability changes is much larger than the time scale on which a reaction occurs. It reduces computational effort at the cost of accuracy.

## 2.6 LATERAL INTERACTIONS

We have already discussed some forms of the transition probabilities. These transition probabilities are not only influenced by external factors like temperature, reactant pressure, and the potential of the surface. The presence or absence of adsorbates on neighbouring sites may also influence the transition probability. This effect is referred to as a *lateral interaction*. These lateral interactions are usually divided into two classes, direct and indirect. The second class is also referred to as through-surface. The direct interactions are subdivided into electrostatic interactions (due to Coulomb repulsion between neighbouring dipoles) and hybridisation between neighbouring adsorbates (due to overlap between wave functions). The indirect interactions are subdivided into electronic through-surface interactions (due to sharing of substrate atoms by the adsorbates) and elastic interactions (due to an adsorbate-induced change in the substrate geometry). This is extensively discussed in Ref. 7 and 8. Here we discuss

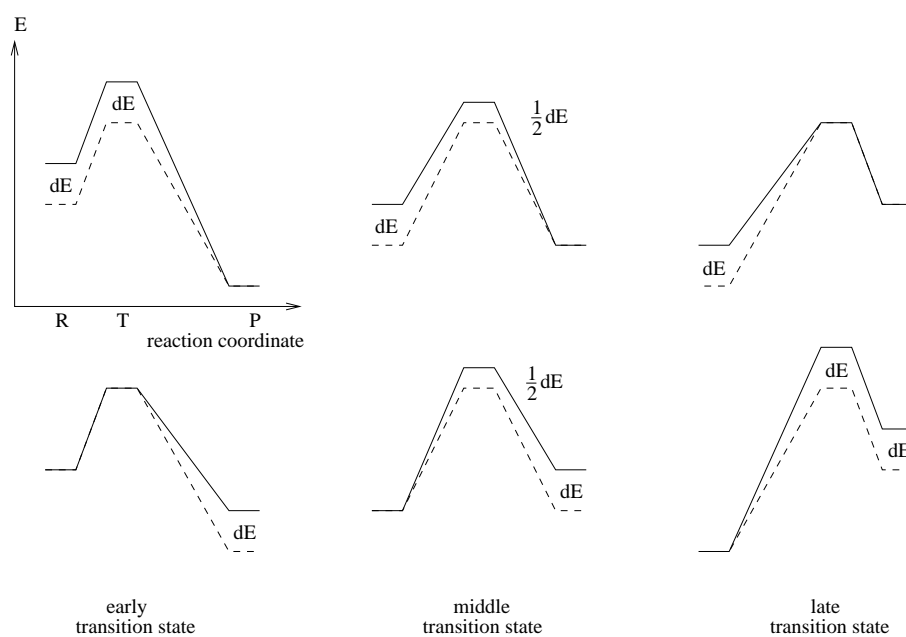


Figure 2.3: Illustration of the shifts in energy of the transition state (T) caused by upward shifts of the product (P, lower panel) or reactant (R, upper panel) states, as a function of the type of transition state: early (left), middle (centre) and late (right). Dashed line: original reaction path, solid line: modified reaction path. Shifts were determined according to the Brønsted-Evans-Polanyi relation. This scheme shows that lateral interactions do not alter the activation energy for an early transition state. Lateral interactions moderately and strongly alter the activation energy for respectively a middle and late transition state.

the influence of lateral interactions on transition probabilities of the Arrhenius form

$$W_{\beta\alpha} = \nu \exp \left[ -\frac{E_{\text{act}}}{RT} \right]. \quad (2.30)$$

In this case the presence of neighbouring adsorbates causes a change in the activation energy  $E_{\text{act}}$ . Calculating activation energies, and shifts in activation energies due to co-adsorbates using for example density-functional theory is quite laborious and involves many calculations. One can estimate the influence of other adsorbates on the activation energy by means of the Brønsted-Evans-Polanyi relation [9–12] which holds provided that the energy changes are small ( $\delta E < E_{\text{act}}^0$ ) and the reaction mechanism does not change:

$$E'_{\text{act}} = E_{\text{act}}^0 + \alpha \delta E \quad (2.37)$$

where  $E'_{\text{act}}$  ( $E_{\text{act}}^0$ ) is the activation energy with (without) lateral interactions,  $\alpha$  is the Brønsted-Evans-Polanyi coefficient ( $\alpha \in [0, 1]$ ) and  $\delta E$  is the change in reaction energy caused by lateral interactions,

$$\delta E = (E'_{\text{prod}} - E'_{\text{react}}) - (E_{\text{prod}}^0 - E_{\text{react}}^0), \quad (2.38)$$

where  $E'_{\text{react}}$  ( $E_{\text{react}}^0$ ) equals the energy of the reactants with (without) lateral interactions and  $E'_{\text{prod}}$  ( $E_{\text{prod}}^0$ ) equals the energy of the products with (without) lateral interactions. This can also be written as

$$\delta E = (E'_{\text{prod}} - E_{\text{prod}}^0) - (E'_{\text{react}} - E_{\text{react}}^0). \quad (2.39)$$

If the interactions are assumed to be pairwise additive, we can write

$$E'_{\text{react}} - E_{\text{react}}^0 = \sum_i \varphi_{\text{react}}(i), \quad (2.40)$$

and a similar expression for the products. The sum is over all pair interactions and  $\varphi(i)$  is the corresponding energy. To calculate  $\delta E$  we only have to include terms that change. Both experimental measurements and DFT calculations confirm that lateral interactions are principally pairwise in nature; three-particle interactions do not play a large role [13–18].

The Brønsted-Evans-Polanyi coefficient  $\alpha$  defines the type of transition state (Figure 2.3). If  $\alpha = 0$ , there is an early barrier and the transition state shifts with the reactant state. Lateral interactions therefore do not influence the activation energy. If  $\alpha = 1$ , there is a late barrier and the transition state shifts with the product state. In this case (and any other case in which  $\alpha > 0$ ) lateral interactions do influence the activation energy. The type of transition state is known to correlate with the exothermicity of the reaction: a strongly exothermic reaction often corresponds to an early transition state, a strongly endothermic reaction to a late transition state. The transition state of an athermic reaction has characteristics of both reactant and product states [19, 20].

The difference of the activation energies of the forward and the backward reaction is always equal to the difference in energy between the reactant and the product state. This implies that

$$\alpha_{\text{forward}} = 1 - \alpha_{\text{backward}}. \quad (2.41)$$

At sufficiently high temperatures a correct Gibbs distribution will therefore be reached. Note that in this section we have equated the transition probability to an Arrhenius *rate constant*. In general the transition probabilities can indeed be seen as microscopic rate constants. We will therefore usually refer to the transition probabilities as rate constants when describing our results.

## 2.7 OTHER ALGORITHMS

The disadvantage of the First Reaction Method (FRM) algorithm lies in the fact that maintaining the time-ordered reaction list  $L_{\text{rx}}$  scales as  $O(\log S)$ . Other algorithms do not require such an event list and may therefore be more efficient [1, 21].

The Variable Step Size Method (VSSM) is one example of an algorithm that does not require an event list. It generates a time interval  $\Delta t$  when no reaction takes place

$$\Delta t = \frac{1}{\sum_{\beta} W_{\beta\alpha}} \ln(r), \quad (2.42)$$

where  $r$  is again a random deviate on the unit interval, and  $\sum_{\beta} W_{\beta\alpha}$  is the sum of all the transition probabilities that transform the current configuration  $\alpha$  in some other configuration. So, instead of having a time generated for each possible reaction as in the FRM algorithm, we here have one time generated for all possible reactions together, and after this time one of the possible reactions has occurred.

Next a reaction  $\alpha \rightarrow \alpha'$  is chosen that takes place at this time  $\Delta t$  by randomly selecting it with probability

$$\frac{W_{\alpha'\alpha}}{\sum_{\beta} W_{\beta\alpha}}, \quad (2.43)$$

and the configuration is updated. A new time step  $\Delta t$  can be generated, and again a reaction can be performed. The tricky point in this algorithm is related to the fact that  $\sum_{\beta} W_{\beta\alpha}$  needs to be calculated. This still requires a list to be made with all possible reactions, but it need not be time-ordered like in the FRM algorithm.

In principle this list needs to be updated after each reaction: new reactions need to be added, and disabled ones need to be removed, otherwise the time step generated in the algorithm will be incorrect. In FRM we also had to update our list, but in practice we only needed to add the new reactions, we did not need to remove the disabled ones.

This same trick works for VSSM as well. It can be proven that if the disabled reactions are not removed from the list in VSSM, the probability distribution for the time that the first *enabled* reaction occurs does not change. We can therefore use an approximate event list, which contains the desired enabled reactions and disabled

reactions, and still get a correct evolution of our system with time. The scaling of the VSSM algorithm with the approximate reaction list is  $O(1)$ , better than FRM.

A third algorithm to solve the Master Equation is the Random Selection Method (RSM). In this algorithm even less bookkeeping is done: the time, the site where the reaction takes place, and the type of reaction are generated individually. In VSSM the site where the reaction takes place and the type of the reaction are combined; the time is generated separately. In FRM all three are stored together in the event list. The RSM algorithm uses a technique called *oversampling* and assumes that all reactions are possible on any site. The advantage of taking all reactions possible on any site is that the reaction list remains the same over the entire simulation. This assumption, like in the previous cases for FRM and VSSM where disabled reactions need not be removed from the reaction list, simplifies the algorithm, but still yields the correct evolution of our system with time.

A time step  $\Delta t$  is generated

$$\Delta t = -\frac{1}{NW_{\max}} \ln(r), \quad (2.44)$$

where  $N$  is the total number of sites, and  $W_{\max}$  is the largest transition probability in the simulation. Next, a site is picked randomly, and a reaction is picked randomly. The randomly picked reaction  $\alpha \rightarrow \beta$  at that certain site is accepted if it is possible on that site, and even then only with a chance

$$\frac{W_{\beta\alpha}}{W_{\max}}, \quad (2.45)$$

where  $W_{\max}$  is again the largest transition probability in the simulation. This algorithm is efficient if the acceptance rate in the previous equation is reasonable, i.e., if the rates of the different processes in our simulation do not differ by many orders of magnitude.

The VSSM and RSM algorithm perform well for large system sizes  $S$  (because they scale well) and for few transition probabilities  $W_{\beta\alpha}$  (since then the acceptance rate is large). The cases discussed in this thesis often include lateral interactions, which give rise to many transition probabilities  $W_{\beta\alpha}$ . We also often encounter time-dependent transition probabilities. These also undo most of the advantages of the VSSM and RSM algorithm. The simulations in this thesis are therefore all performed using the FRM algorithm. Note that in principle these different algorithms can be used together in one simulation, as long as each algorithm is associated with a different reaction. The algorithms mentioned above have been implemented in the program CARLOS [22]. The implementation of the FRM algorithm allows inclusion of time-dependent rate constants and lateral interactions. Other *equilibrium* Monte Carlo algorithms are also known, these can generate typical configurations  $\alpha$  for a certain system. But these algorithms are (by definition) not able to describe the time-evolution of a system. Therefore, no information on, for example, reaction rates can be derived by using these equilibrium Monte Carlo algorithms.

## 2.8 HOW TO GET TRANSITION PROBABILITIES

To do an actual simulation of a system, all the transition probabilities need to be known. These transition probabilities can be obtained from both experiments and from theory. The most common ways are to get them from temperature programmed desorption (TPD) experiments [23–26], scanning tunnelling microscopy (STM) [13, 14, 27–29], single crystal adsorption calorimetry [30–32], laser desorption spectroscopy [33–35], rate theory [36, 37], bond order conservation theory [38–40], and by solving the Schrödinger equation [15, 41–44]. These different techniques can yield information on desorption rate constants, lateral interactions, diffusion rate constants, and rate constants for dissociation and recombination. It needs to be mentioned that the estimates for these kinetic parameters are usually only obtained after assuming a certain model.

If the information from these techniques is insufficient to determine all transition probabilities, or if one wants an independent approach to finding the values of these transition probabilities, then one needs to fit the experiment directly. This involves doing a simulation with approximate values for the transition probabilities and comparing the results to the experiment. Based on the difference between the two one can adapt the estimates for the transition probabilities and try again. This procedure can be performed manually, but it can also be automated. If it is automated, then one refers to it as a closed loop learning algorithm. One example of such algorithm is the Evolutionary Strategy type algorithm.

## 2.9 EVOLUTIONARY STRATEGY OPTIMISATION

The Evolutionary Strategy optimisation algorithm, implemented in PLATYPUS [45], works as follows. We will be looking for a set of kinetic parameters (lateral interactions, prefactors, activation energies, etc.) which define the transition probabilities.

### 1. Initialisation.

We define the set of  $n$  kinetic parameters we want to optimise. For each of these kinetic parameters we specify a range. We can then generate a starting parameter set, or *chromosome*, by specifying a value for each kinetic parameter in the parameter set. The value of each kinetic parameter is randomly generated, but within the range of that kinetic parameter. To start the optimisation we make a group of chromosomes, that is, a group of  $\mu$  randomly generated parameter sets. This group of chromosomes is called the *parent generation*. We assign a reference (e.g., an experiment), to which we are going to compare the results of our simulations.

### 2. Variation.

We now generate  $\lambda$  new chromosomes, with  $\lambda \geq \mu$ , from the  $\mu$  old chromosomes. This new set of chromosomes is referred to as the *offspring*. New chromosomes are generally generated in two ways, by mutation and crossover. These are defined below.

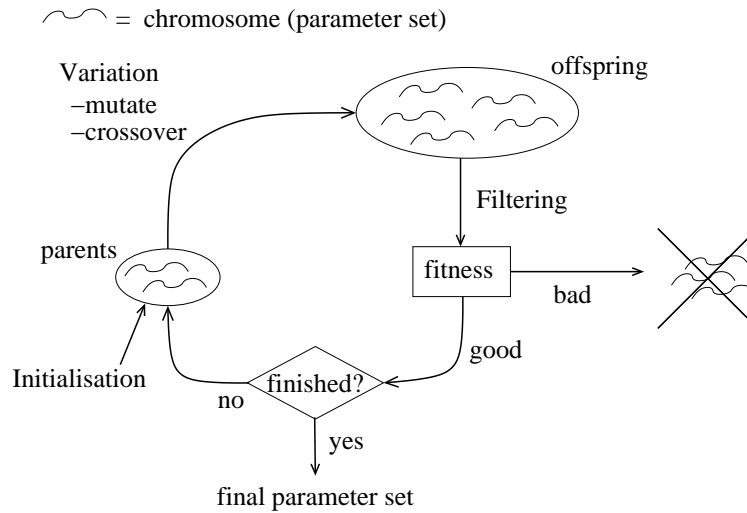


Figure 2.4: Schematic depiction of the Evolutionary Strategy optimisation algorithm.

### 3. Filtering.

We run a simulation for each chromosome (parameter set). We compare the result of the simulation for each chromosome to the reference. Based on the likeness between the simulation and the reference, we grade each chromosome. The grade is referred to as the *fitness*. Next, we retain only the  $\mu$  best of the  $\lambda$  offspring.

### 4. Termination.

If a certain number of generations has been evaluated, if the fitness of some chromosome supersedes some critical value, or if the fitness of a population does not change during several successive cycles, the optimisation is terminated. The chromosome(s) with the best fitness can then be inspected to see whether they correspond to a physically sound description of the system. If so, the parameter set is accepted. If not, we repeat at 2.

The fact that only parameter sets are maintained which have a good fitness is similar to Darwinian evolution theory in biology, where only species that are well adapted to their surroundings will survive. Hence the name Evolutionary Strategy optimisation [46, 47]. The encoding of the parameter set in a chromosome, and the generation of new chromosomes by mutation and crossover has many similarities to biological genetics. A parameter encoded in a chromosome is therefore also referred to as a *gene*. Similar optimisation algorithms with genes that can only have the value 1 or 0 are therefore known as Genetic Algorithms [48, 49].



The process of *mutation* involves randomly changing the value of one of the kinetic parameters (or genes) in the parent chromosome, thus yielding a new chromosome. Mutation in a Genetic Algorithm corresponds to a bit flip: a zero is converted into one, or the other way around. For the case of Evolutionary Strategies, the mutation is more complicated, since each gene may have any value. One therefore stores not only the value of a gene  $x_i$ , but also a mutation parameter (called  $\sigma_i$ ) which indicates how much the value of that gene is changed upon mutation. The change of the value of the gene is then calculated by drawing a random number from a Gaussian distribution with width  $\sigma_i$ .

The process of *crossover* involves the use of two parent chromosomes to generate a new chromosome. The new chromosome may inherit some kinetic parameters from one parent chromosome, and the others from the other parent chromosome. Another possibility is that the new chromosome is constructed by taking for each kinetic parameter the average of the values of the two parent chromosomes. Note that usually the choice is made that chromosomes of the parent generation are not allowed to pass on to the offspring unchanged. This prevents premature convergence if, at the beginning of the optimisation, one chromosome is far superior to all the others.

The algorithm requires the assignment of a fitness to each chromosome. Defining such a fitness can be very complicated, since a good kinetic parameter set reproduces the experiment *and* is physically sound. The resemblance to the experiment can easily be calculated by taking the difference between the experimental and the simulated value. The judgement whether the kinetic parameter set is physically meaningful is often much more difficult to determine automatically. The fitness is therefore often determined only by the resemblance of the simulation to the experiment. One then decides only after the optimisation has finished whether the optimum found is the one one was looking for. This is why in the termination part of the algorithm there is an explicit manual check to see whether the optimum found is physically sound.

Most conventional optimisation algorithms operate in a serial way. The old parameter set is evaluated, and based on the outcome for this parameter set (and possibly others), the values for the parameters in the new parameter set are determined. This implies that the new parameter set can only be evaluated after the previous parameter set has been evaluated. The optimisation procedure can therefore not be efficiently divided over different computers to speed up the optimisation. On the other hand, the evaluation of the fitness of the chromosomes in the Evolutionary Strategy algorithm can be performed in parallel, since the chromosomes are determined independently. By dividing the evaluation of the chromosomes over different computers we can therefore significantly reduce the total time needed to optimise the parameter set.

Since the Evolutionary Strategy algorithm starts out with many randomly chosen start parameter sets, the optimum found is less likely to be a local optimum. In a conventional optimisation algorithm, the parameter set is usually very efficiently optimised to the nearest optimum, but there is no guarantee that this nearest optimum is the best. There is no such guarantee either in the case of the Evolutionary Strategy algorithm, but the overall odds of finding the global optimum are better since we start out with many randomly chosen start parameter sets instead of one. If there is

more than one global optimum, then this can also be detected using an Evolutionary Strategy algorithm.

The Evolutionary Strategy algorithm does not look at local gradients to approach the optimum, instead it relies on the small random changes to guide it to the desired optimum. This makes the algorithm also suitable to optimise noisy functions, i.e., functions with rapidly varying gradients. It also makes optimisation possible for functions for which no gradient can be defined. For the case of our kinetic Monte Carlo simulations, the outcome does show noise since it is a stochastic simulation. Determining the gradient by taking a slightly different parameter set can therefore give widely differing outcomes depending on which simulations are compared. These two points also favour the use of the Evolutionary Strategy algorithm over a conventional optimisation algorithm.

To run an Evolutionary Strategy optimisation, we need to fix the number of chromosomes in the parent generation ( $\mu$ ) and the number of chromosomes in the offspring ( $\lambda$ ). We need to decide how to encode the kinetic parameters to become the genes of each chromosome. We need to specify how we will determine the fitness of a chromosome. We need to specify how often a gene will mutate, and the size of the mutation. We need to specify how cross-over takes place, and how often.

To summarise, Evolutionary Strategy algorithms are suitable to optimise large parameter sets, for which each parameter can take many values. This is especially the case if no derivative can be determined, and if there are many local optima. Small parameter sets, or near-optimal parameter sets are better optimised using conventional algorithms. Evolutionary Strategy optimisation algorithms have been successfully applied in numerous fields. In the chemistry field they have been amongst others applied to optimise femtosecond laser beams used to excite molecules [50–55], to design combinatorial libraries [56, 57], to construct quantitative structure-property relationships [58–61], and to optimise the geometry of heterogeneous bimetallic catalyst models [62, 63]. They have very recently also been used to optimise heterogeneous catalysts [64–72].

- [1] A. P. J. Jansen; An introduction to Monte Carlo simulations of surface reactions; <http://arXiv.org/>, paperno. cond-mat/0303028, 2003.
- [2] R. J. Gelten, R. A. van Santen and A. P. J. Jansen; *Molecular dynamics. From Classical to Quantum Methods*, volume 7 of *Theoretical and Computational Chemistry*, chapter Dynamic Monte Carlo Simulations of Oscillatory Heterogeneous Catalytic Reactions, pages 737–784; Elsevier Science B.V., 1999.
- [3] N. G. van Kampen, editor; *Stochastic Processes in Physics and Chemistry*; North-Holland, Amsterdam, 1992.
- [4] John Segers; *Algorithms for the simulation of surface processes*; PhD thesis, Eindhoven University of Technology, 1999.
- [5] I. Chorkendorff and J. W. Niemantsverdriet; *Concepts of modern catalysis and kinetics*; Wiley-VCH, Weinheim, 2003.
- [6] A. P. J. Jansen; Monte carlo simulations of chemical reactions on a surface with time-dependent reaction-rate constants; *Comput. Phys. Commun.*, 86: 1–12, 1995.
- [7] J. K. Nørskov; *Coadsorption, promoters and poisons*, volume 6 of *The chemical physics of solid surfaces*, chapter 1 Adsorbate-adsorbate interactions on metal surfaces, pages 1–27; Elsevier, 1993.
- [8] M. L. Merrick, W. Luo and K. A. Fichthorn; Substrate-mediated interactions on solid surfaces: theory, experiment, and consequences for thin-film morphology; *Progr. Surf. Sci.*, 72: 117–134, 2003.
- [9] M. G. Evans and M. Polanyi; Inertia and driving force of chemical reactions; *Trans. Faraday. Soc.*, 34: 11–29, 1938.
- [10] J. N. Brønsted; Acid and basic catalysts; *Chem. Rev.*, 5: 231–338, 1928.
- [11] R. I. Masel, editor; *Principles of Adsorption and Reaction on Solid Surfaces*; Wiley series in chemical engineering. Wiley, New York, 1996.
- [12] G. Ertl, H. Knoezinger and J. Weitkamp, editors; *Handbook of Heterogeneous Catalysis*, volume 3; Weinheim, New York, 1997.
- [13] L. Österlund, M. Ø. Pedersen, I. Stensgaard, E. Lægsgaard and F. Besenbacher; Quantitative determination of adsorbate-adsorbate interactions; *Phys. Rev. Lett.*, 83(23): 4812–4815, 1999.
- [14] J. Trost, T. Zambelli, J. Wintterlin and G. Ertl; Adsorbate-adsorbate interactions from statistical analysis of STM images: N/Ru(0001); *Phys. Rev. B*, 54(24): 17850–17857, 1996.
- [15] C. Stampfl, H. J. Kreuzer, S. H. Payne, H. Pfnür and M. Scheffler; First-principles theory of surface thermodynamics and kinetics; *Phys. Rev. Lett.*, 83(15): 2993–2996, 1999.
- [16] H. Tang, A. van der Ven and B. L. Trout; Lateral interactions between oxygen atoms adsorbed on platinum (111) by first principles; *Mol. Phys.*, 102(3): 273–279, 2004.
- [17] D. Curulla, A. P. van Bavel and J. W. Niemantsverdriet; Adsorbate-adsorbate lateral interactions. Testing the pairwise additive potential approximation using DFT. Case study: coadsorption of CO and N on Rh(100); 2004.
- [18] W. K. Offermans and A. P. J. Jansen; Determination of lateral interactions with ab initio calculations; 2004.
- [19] J. E. Leffler; Parameters for the description of transition states; *Science*, 117: 340–341, 1953.
- [20] G. S. Hammond; A correlation of reaction rates; *J. Am. Chem. Soc.*, 77: 334–338, 1955.
- [21] J. J. Lukkien, J. P. L. Segers, P. A. J. Hilbers, R. J. Gelten and A. P. J. Jansen; Efficient Monte Carlo methods for the simulation of catalytic surface reactions; *Phys. Rev. E*,

- 58(2): 2598–2610, 1998.
- [22] CARLOS is a general-purpose program, written in C, for simulating reactions on surfaces that can be represented by regular grids; an implementation of the First-Reaction Method and the Variable Stepsize Method, written by J. J. Lukkien.
- [23] C. M. Chan, R. Aris and W. H. Weinberg; An analysis of thermal desorption mass spectra.I.; *Appl. Surf. Sci.*, 1: 360–376, 1978.
- [24] A. M. de Jong and J. W. Niemantsverdriet; Thermal desorption analysis: comparative test of ten commonly applied procedures; *Surf. Sci.*, 233: 355–365, 1990.
- [25] A. M. de Jong and J. W. Niemantsverdriet; Comparative test of procedures for thermal desorption analysis; *Vacuum*, 41(1–3): 232–233, 1990.
- [26] D. L. S. Nieskens, A. P. van Bavel and J. W. Niemantsverdriet; The analysis of temperature-programmed desorption experiments of systems with lateral interactions; implications of the compensation effect; *Surf. Sci.*, 546: 159–169, 2003.
- [27] T. Zambelli, J. Trost, J. Wintterlin and G. Ertl; Diffusion and atomic hopping of N atoms on Ru(0001) studied by scanning tunneling microscopy; *Phys. Rev. Lett.*, 76(5): 795–798, 1996.
- [28] S. Renisch, R. Schuster, J. Wintterlin and G. Ertl; Dynamics of adatom motion under the influence of mutual interactions: O/Ru(0001); *Phys. Rev. Lett.*, 82(19): 3839–3842, 1999.
- [29] J. Wintterlin, J. Trost, S. Renisch, R. Schuster, T. Zambelli, and G. Ertl; Real-time STM observations of atomic equilibrium fluctuations in an adsorbate system: O/Ru(0001); *Surf. Sci.*, 394: 159–169, 1997.
- [30] L. Vattuone, Y. Y. Yeo and D. A. King; Adatom bond energies and lateral interaction energies from calorimetry: NO, O-2, and N-2 adsorption on Ni{100}; *J. Chem. Phys.*, 104(20): 8096–8102, 1996.
- [31] R. Kose, W. A. Brown and D. A. King; Role of lateral interactions in adsorption kinetics: CO/Rh{100}; *J. Phys. Chem. B*, 103: 8722–8725, 1999.
- [32] Q. Ge, R. Kose and D. A. King; Adsorption energetics and bonding from femtomole calorimetry and from first principles theory; *Adv. Catal.*, 45: 207–259, 2000.
- [33] E. G. Seebauer, A. C. F. Kong and L. D. Schmidt; Investigations of adsorption on Pt and Rh by laser-induced desorption; *J. Vac. Sci. Tech. A*, 5(4): 464–468, 1987.
- [34] E. G. Seebauer, A. C. F. Kong and L. D. Schmidt; Surface diffusion of hydrogen and CO on Rh(111): laser-induced thermal desorption studies; *J. Chem. Phys.*, 88(10): 6597–6604, 1988.
- [35] E. G. Seebauer and C. E. Allen; Estimating surface diffusion coefficients; *Progr. Surf. Sci.*, 49(3): 265–330, 1995.
- [36] V. P. Zhdanov, J. Pavlicek and Z. Knor; Preexponential factors for elementary surface processes; *Catal. Rev.-Sci. Eng.*, 30(4): 501–517, 1988.
- [37] V. P. Zhdanov; Arrhenius parameters for rate processes on solid surfaces; *Surf. Sci. Rep.*, 12(5): 183–242, 1991.
- [38] E. Shustorovich and H. Sellers; The UBI-QEP method: a practical theoretical approach to understanding chemistry on transition metal surfaces; *Surf. Sci. Rep.*, 31(1–3): 5–119, 1998.
- [39] E. W. Hansen and M. Neurock; Modelling surface kinetics with first-principles-based molecular simulation; *Chem. Eng. Sci.*, 54: 3411–3421, 1999.
- [40] S. P. Baranov, L. A. Abramova, A. V. Zeigarnik and E. Shustorovich; Monte carlo modeling of O-2 adsorption kinetics on unreconstructed fcc(100) surfaces of metals using

- UBI-QEP coverage-dependent energetics; *Surf. Sci.*, 555(1–3): 20–42, 2004.
- [41] E. W. Hansen and M. Neurock; First-principles-based Monte-Carlo methodology applied to O/Rh(100); *Surf. Sci.*, 464: 91–107, 2000.
- [42] E. Hansen and M. Neurock; Predicting lateral surface interactions through density functional theory: application to oxygen on Rh(100); *Surf. Sci.*, 441: 410–424, 1999.
- [43] K. Honkala, P. Pirilä and K. Laasonen; Coadsorption of CO and NO on the Pd(111) surface: combined ab initio and Monte Carlo study; *Phys. Rev. Lett.*, 86(26): 5942–5945, 2001.
- [44] B. Hammer; Adsorption, diffusion and dissociation of NO, N and O on flat and stepped Ru(001); *Surf. Sci.*, 459: 323–348, 2000.
- [45] PLATYPUS is an optimisation program for problems that can be handled by Genetic Algorithms (GA) or Evolutionary Strategies (ES). It is written in C++ by A. P. J. Janssen.
- [46] Z. Michalewicz; *Genetic Algorithms + Data Structures = Evolution Programs*; Springer, Berlin, 3rd edition, 1996.
- [47] H.-P. Schwefel; *Evolution and optimum seeking*; Sixth generation computer technology series. John Wiley & Sons, 1995.
- [48] L. Davis; *Handbook of Genetic Algorithms*; Van Nostrand Reinhold, New York, 1991.
- [49] D. E. Goldberg; *Genetic algorithms in search, optimization, and machine learning*; Addison-Wesley, Amsterdam, 1989.
- [50] D. Zeidler, S. Frey, K.-L. Kompa and M. Motzkus; Evolutionary algorithms and their application in optimal control studies; *Phys. Rev. A*, 64: 023420–1–13, 2001.
- [51] J. L. Herek, W. Wohlleben, R. J. Cogdell, D. Zeidler and M. Motzkus; Quantum control of energy flow in light harvesting; *Nature*, 417: 533–535, 2002.
- [52] T. Brixner, N. H. Damrauer, P. Niklaus and G. Gerber; Photosensitive adaptive femtosecond quantum control in the liquid phase; *Nature*, 414: 57–60, 2001.
- [53] H. Rabitz, R. de Vivie-Riedle, M. Motzkus and K. Kompa; Whither the future of controlling quantum phenomena; *Science*, 288: 24–28, 2000.
- [54] A. Assion, T. Baumert, M. Bergt, T. Brixner, B. Kiefer, V. Seyfried, M. Strehle and G. Gerber; Control of chemical reactions by feedback-optimized phase-shaped femtosecond laser pulses; *Science*, 282: 919–922, 1998.
- [55] R. S. Judson and H. Rabitz; Teaching lasers to control molecules; *Phys. Rev. Lett.*, 68(10): 1500–1503, 1992.
- [56] R. P. Sheridan, S. G. SanFeliciano and S. K. Kearsly; Designing targeted libraries with genetic algorithms; *J. Mol. Graphics Mod.*, 18: 320–334, 2000.
- [57] R. D. Brown and Y. C. Martin; Designing combinatorial library mixtures using a genetic algorithm; *J. Med. Chem.*, 40: 2304–2313, 1997.
- [58] K. Hasegawa, Y. Miyashita and K. Funatsu; GA strategy for variable selection in QSAR studies: GA-based PLS analysis of calcium channel antagonists; *J. Chem. Inf. Comput. Sci.*, 37: 306–310, 1997.
- [59] D. Rogers and A. J. Hopfinger; Application of genetic function approximation to quantitative structure-activity relationships and quantitative structure-property relationships; *J. Chem. Inf. Comput. Sci.*, 34: 854–866, 1994.
- [60] H. Gao, M. S. Lajiness and J. Van Drie; Enhancement of binary QSAR analysis by a GA-based variable selection method; *J. Mol. Graphics Mod.*, 20: 259–268, 2002.
- [61] K. Hasegawa, T. Kimura and K. Funatsu; GA strategy for variable selection in QSAR studies: enhancement of comparative molecular binding energy analysis by a GA-based PLS method; *Quant. Struct.-Act. Relat.*, 18: 262–272, 1999.

- [62] A. S. McLeod and L. F. Gladden; Heterogeneous catalyst design using stochastic optimization algorithms; *J. Chem. Inf. Comput. Sci.*, 40: 981–987, 2000.
- [63] A. S. McLeod, M. E. Johnston and L. F. Gladden; Development of a genetic algorithm for molecular scale catalyst design; *J. Catal.*, 167: 279–285, 1997.
- [64] J. M. Serra, A. Chica and A. Corma; Development of a low temperature light paraffin isomerization catalysts with improved resistance to water and sulphur by combinatorial methods; *Appl. Catal. A*, 239: 35–42, 2003.
- [65] D. Wolf, O. V. Buyevskaya and M. Baerns; An evolutionary approach in the combinatorial selection and optimization of catalytic materials; *Appl. Catal. A*, 200: 63–77, 2000.
- [66] G. Kirsten and W. F. Maier; Strategies for the discovery of new catalysts with combinatorial chemistry; *Appl. Surf. Sci.*, 223: 87–101, 2004.
- [67] G. Frubert, E. Kondratenko, S. Kolf, M. Baerns, P. van Geem and R. Parton; Fundamental insights into the oxidative dehydrogenation of ethane to ethylene over catalytic materials discovered by an evolutionary approach; *Catal. Today*, 81: 337–345, 2003.
- [68] K. Huang, X.-L. Zhan, F.-Q. Chen and D.-W. Lü; Catalyst design for methane oxidative coupling by using artificial neural network and hybrid genetic algorithm; *Chem. Eng. Sci.*, 58: 81–87, 2003.
- [69] J. N. Cawse, M. Baerns and M. Holena; Efficient discovery of nonlinear dependencies in a combinatorial catalyst data set; *J. Chem. Inf. Comput. Sci.*, 44: 143–146, 2004.
- [70] U. Rodemerck, M. Baerns, M. Holena and D. Wolf; Application of a genetic algorithm and a neural network for the discovery and optimization of new solid catalytic materials; *Appl. Surf. Sci.*, 223: 168–174, 2004.
- [71] A. Corma, J. M. Serra and A. Chica; Discovery of new paraffin isomerization catalysts based on  $\text{SO}_4^{2-}/\text{ZrO}_2$  and  $\text{WO}_x/\text{ZrO}_2$  applying combinatorial techniques; *Catal. Today*, 81: 495–506, 2003.
- [72] T. Umegaki, Y. Watanabe, N. Nukui, K. Omata and M. Yamada; Optimization of catalyst for methanol synthesis by a combinatorial approach using a parallel activity test and genetic algorithm assisted by a neural network; *Energy & Fuels*, 17: 850–856, 2003.

32 REFERENCES

## CHAPTER 3

# ADSORPTION AND REACTION OF NO ON Rh(111)

We present a model that reproduces the experimentally observed adsorption and reaction behaviour of NO on Rh(111). The model describes the adsorption of NO on threefold sites at low coverages, and the subsequent ordering into a  $c(4 \times 2)$ -2NO structure. It describes the occupation of top sites next to threefold sites as a result from adsorbate-adsorbate interactions at higher coverages. It yields at saturation a  $(2 \times 2)$ -3NO ordered structure with in each unit cell two threefold bound and one top bound NO. Simulations of the temperature-programmed reaction were able to explain the attenuation of the dissociation rate due to the presence of other adsorbed species, i.e., NO and its dissociation products atomic nitrogen and atomic oxygen. The attenuation of the dissociation rate is due to a lack of accessible sites on the surface, that is, sites where a molecule can bind without experiencing large repulsions with neighbouring adsorbates.

### 3.1 INTRODUCTION

The ability of Rh to efficiently dissociate NO makes it the most suitable metal for the removal of nitrogen oxides from automotive exhaust gases in catalytic converters. The system of NO on Rh(111) has subsequently been extensively studied under UHV conditions. Adsorption of NO is molecular below 275 K, and two ordered structures can be formed depending on the temperature, one at around 0.50 ML, and one at close to 0.75 ML [1, 2]. These structures have been deduced from LEED measurements. The structure at 0.50 ML is thought to consist of three types of domains which are rotated 120 degrees with respect to each other. It is known as the  $c(4 \times 2)$ -2NO structure. A similar  $c(4 \times 2)$  structure is also known for NO on Ni(111) and for both NO and CO on Pd(111) [3–6]. The  $(2 \times 2)$ -3NO saturation structure is only formed at



temperatures above 225 K. At lower temperatures the saturation coverage decreases to 0.68 ML [7]. The configuration of the adlayer at these lower temperatures is still unclear. The  $(2 \times 2)$  saturation structure is known for NO on Pt(111) and Ru(001), and for both NO and CO on Pd(111) and Rh(111) [4–6, 8–11].

In TPD experiments, it was found that there are three distinct coverage regions displaying differing behaviour [12]. Below 0.25 ML all NO dissociates between 275 and 325 K, indicating sufficient accessible sites on the surface. The N adatoms formed in the dissociation recombine in a second order peak between 450 and 650 K. The oxygen adatoms recombine at temperatures above 900 K. At intermediate coverages (between 0.25 and 0.50 ML), part of the NO is thought to dissociate (above 300 K), filling the empty available threefold sites on the surface. When all empty sites are filled, the dissociation is inhibited till the desorption of NO. Above 400 K, part of the remaining NO desorbs, while another part dissociates after all. Nitrogen gas is formed in two peaks, one of which coincides with the NO desorption peak, the other one is at higher temperatures. At coverages above 0.50 ML the top sites become occupied as well, resulting in an additional NO desorption peak at 380 K. Dissociation of NO is totally inhibited up to over 400 K, when the threefold bound NO starts desorbing. These different types of behaviour are all related to the interactions between the adsorbates; because of the repulsion reactions can be suppressed or enhanced, while different sites may be occupied to prevent strong repulsion.

All these observations ask for a better view of the adsorbate distribution on the single crystal surface. In this chapter we introduce a three-site Monte Carlo model with lateral interactions in order to get a deeper insight into how the adsorbates, NO, N and O in particular, are distributed on the catalytically active Rh(111) surface. A similar study for the (100) surface of rhodium has been conducted in parallel, and is reported elsewhere [13].

## 3.2 MODEL AND METHODS

### 3.2.1 THE REACTION MODEL

Our model consists of a lattice of top, fcc and hcp sites. These three sites form a regular grid (Figure 3.1) with a spacing of  $1/\sqrt{3} d_{\text{Rh-Rh}}$ , where the grid unit cell vectors ( $\mathbf{c}_1$  and  $\mathbf{c}_2$ ) are at a 30 degree angle with the primitive lattice vectors ( $\mathbf{a}_1$  and  $\mathbf{a}_2$ ) of the (111) surface. Every site is labelled t, f or h according to its type, with a prefix to indicate the type of adsorbate: NO, N, O or \* (the last stands for an empty site).

Based on the results from the DFT-calculations, which are presented in the Results and Discussion section, we have excluded the sites nearest to an adsorbate from occupation (at distance  $|\mathbf{c}|$ , see Figure 3.1). Two other kinds of lateral interactions have been taken into account: one at the next-nearest neighbour site (one lattice vector,  $|\mathbf{a}|$ , or  $d_{\text{Rh-Rh}}$ , apart), the other one at the next-next-nearest neighbour site ( $2/\sqrt{3}$  lattice vector or  $2|\mathbf{c}|$  apart).

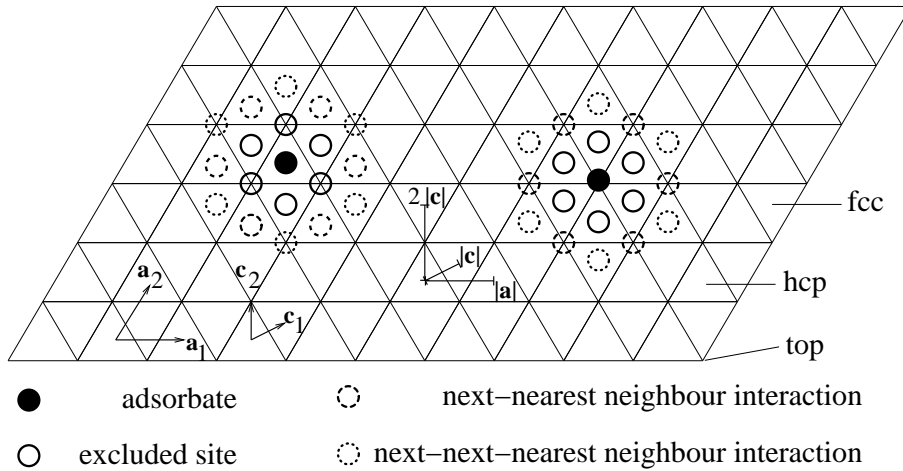


Figure 3.1: Excluded sites and lateral interactions in the three-site model. The lateral interactions for an adsorbate bound to the fcc site are similar to the ones for an adsorbate bound to the hcp site, and are therefore not displayed.

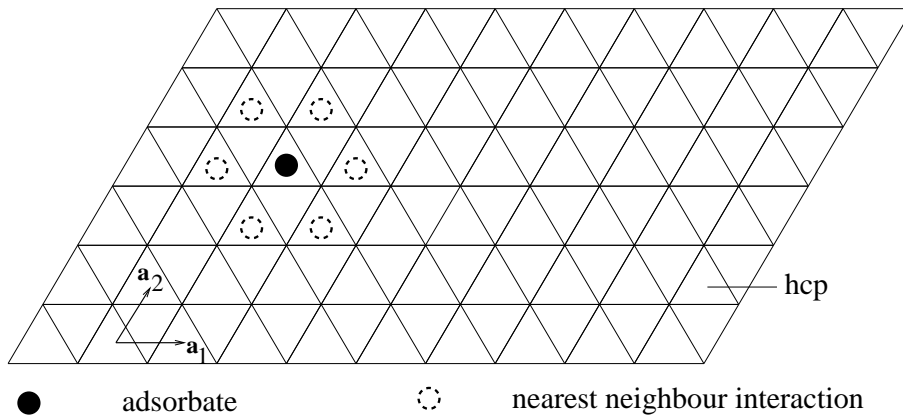
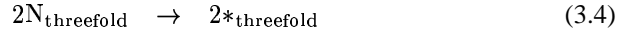
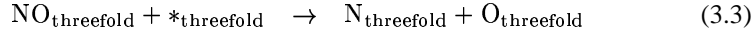
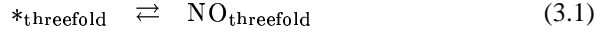


Figure 3.2: Lateral interactions in the single-site model. The adsorbates only bind to the hcp site, and therefore only experience interactions from adsorbates bound to neighbouring hcp sites. The fcc and top site are not included.

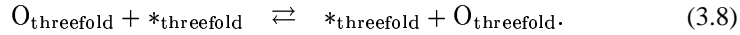
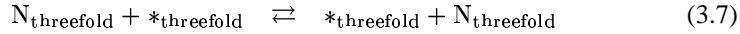
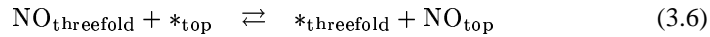
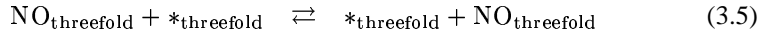
Table 3.1: Kinetic parameters for NO on Rh(111).

	$\nu$ (s <sup>-1</sup> )	$E_{\text{act}}$ (kJ/mol)	Notes
<b>NO Adsorption</b>			
NO adsorption	0.01	—	Ref. 14
NO diffusion:			
threefold $\rightarrow$ threefold	10 <sup>9</sup> –10 <sup>13</sup>	22.5	This work
threefold $\rightarrow$ top	10 <sup>9</sup> –10 <sup>13</sup>	47	This work
top $\rightarrow$ threefold	10 <sup>9</sup> –10 <sup>13</sup>	0	This work
<b>NO TPD/TPR</b>			
Diffusion:			
NO, N and O	1000	—	
NO dissociation	10 <sup>11</sup>	65	Ref. 12
NO desorption:			
from top site	10 <sup>13.5</sup>	129	Ref. 12, adapted
from threefold site	10 <sup>13.5</sup>	133	Fitted
N <sub>2</sub> formation	10 <sup>10</sup>	120	Ref. 12

We have included the following reactions:



and diffusion of NO, N and O:



We did not include the bridge site in our model, despite the fact that it has an adsorption energy which lies between the values for the threefold and the top site. The reason for not including the bridge site stems from the observation by means of XPS [15] and EELS [1, 16] that NO on Rh(111) occupies only two kinds of sites, which were later identified as top and threefold [2, 17]. Probably the bridge sites do not allow for a favourable distribution of adsorbates avoiding lateral interactions, and are therefore not significantly occupied.

The kinetic parameters we have used are listed in Table 3.1. Most have been adopted from Ref. 12. Diffusion was modelled with Arrhenius-type rate constants for the low-temperature adsorption simulations, with prefactors between 10<sup>9</sup> and 10<sup>13</sup>

$\text{s}^{-1}$  and the activation energies derived from the differences in binding energies between top, bridge and threefold sites in the DFT calculations. For simplicity we have treated the threefold sites as equivalent in our kMC model, though a difference in binding energy of typically 10 kJ/mol was observed between fcc and hcp sites. Diffusion was not modelled with Arrhenius-type rate constants for the TPD/TPR simulations because it increases with several decades over the simulated temperature range. Instead, rate constants for diffusion were set to  $1000 \text{ s}^{-1}$ , modified by lateral interactions and differences in site adsorption energies:

$$k_{\text{threefold} \rightarrow \text{threefold}} = 1000 \text{ s}^{-1} \times \exp\left(\frac{\alpha \delta E}{RT}\right) \quad (3.9)$$

$$k_{\text{threefold} \rightarrow \text{top}} = 1000 \text{ s}^{-1} \times \exp\left(\frac{\alpha' \delta E - 0.5 \Delta E_b}{RT}\right) \quad (3.10)$$

$$k_{\text{top} \rightarrow \text{threefold}} = 1000 \text{ s}^{-1} \times \exp\left(\frac{(1 - \alpha') \delta E + 0.5 \Delta E_b}{RT}\right), \quad (3.11)$$

where  $\delta E$  equals the shift in energy of the reactants and products due to lateral interactions,  $\Delta E_b$  is the difference in binding energy between the top and the threefold site;  $\alpha$  and  $\alpha'$  are the Brønsted-Evans-Polanyi coefficients for threefold to threefold site and threefold to top site diffusion respectively. Tests with various prefactors have shown that the reduction of nitrogen diffusion only slightly lowers the rate of nitrogen formation. The reduction of other diffusion rates did not cause significantly differing behaviour. So our modelling of the diffusion yields an adlayer at equilibrium without too much computer time spent on diffusion. The desorption of top bound NO is reasonably well-defined, since it occurs from an ordered structure (the  $(2 \times 2)$ -3NO structure). Desorption of threefold NO on the other hand only happens when the surface is filled with N and O atoms. The measured activation energy of desorption is dependant on the lateral interactions with the N and O atoms present. The spatial distribution of these atoms is unknown; we have therefore not used the activation energy of desorption from threefold sites that has been reported in literature (Ref. 12), but fitted the value using the prefactor for top bound NO desorption. The oxygen atom formed in the dissociation reaction was deposited  $2/\sqrt{3}$  lattice vectors away from the nitrogen, nitrogen formation was allowed at a distance of  $3/\sqrt{3}$  lattice vectors. Precursor adsorption of NO [18] was not included in the model, since we are mainly interested in the ordering on the surface, and not in the adsorption process itself. Since dioxygen formation only takes place above 900 K, it was also left out of the model. The grid sizes used were  $132 \times 132$  for the adsorption simulations and  $264 \times 264$  for the TPD/TPR simulations.

In view of the difference in energy between reactant and product we have taken desorption to be a late transition state (and therefore adsorption to be an early transition state), NO dissociation and N recombination to be late transition states ( $\alpha = 1$ ), and diffusion to be a middle transition state ( $\alpha = 0.5$ ).

A simpler model with only one type of site, which was described previously [14, 19], was also considered. This model consists of a lattice of threefold sites; one site

per metal atom, so either fcc or hcp. A nearest-neighbour interaction has been taken into account (Figure 3.2). Note that the nearest neighbour in this single-site model is the *next*-nearest neighbour in the three-site model, one lattice vector or  $|\mathbf{a}|$  apart. Reactions described in equations (3.1), (3.3), (3.4), and diffusion of all species (Eq. (3.5), (3.7), (3.8)) were included. The kinetic parameters used were the same as for the three-site model, except for the desorption of NO, for which the prefactor and activation energy were fitted to  $10^{12.5} \text{ s}^{-1}$  and 118 kJ/mol. Similar models but with fewer types of adsorbates were previously published by Honkala *et al.*, Stampfl *et al.* and Hansen *et al.* [20–22].

### 3.2.2 DFT METHODOLOGY

The VASP code [23, 24] allows periodic DFT calculations (Perdew and Wang functional [25]) with a plane wave basis set and the ultrasoft pseudopotentials introduced by Vanderbilt [26] and generated by G. Kresse and J. Hafner [27]. The surfaces were modelled by a supercell containing a five-layer slab and 13.5 Å of vacuum between the surfaces. For all the calculations the energy cut-off for the plane wave basis set was set to 400 eV as it corresponds to the value for which all the ultrasoft pseudopotentials are converged. The k-point sampling was done following the Monkhorst-Pack procedure, with  $5 \times 5 \times 1$  grids for the  $(2 \times 2)$  and  $c(4 \times 2)$  cells and a  $3 \times 3 \times 1$  grid for the  $(3 \times 3)$  cell, gaussian smearing ( $\alpha = 0.2 \text{ eV}$ ) was applied to the electronics levels. Adsorption was done on both sides of the slab, with at least an inversion centre (no spurious dipole-dipole interactions) and depending on the starting geometry additional symmetry operations were used. A complete geometry optimisation was performed for each configuration. All the parameters (k-points, FFT grids, numerical approximations) were extensively tested and the energies are converged within 3 kJ/mol. Various coverages (0.11, 0.25, 0.50 and 0.75 ML) with different structures ( $(3 \times 3)$ ,  $(2 \times 2)$  and  $c(4 \times 2)$ ) were considered to determine the lateral interactions. Gas phase molecules (NO, O<sub>2</sub> and N<sub>2</sub>) were calculated in the  $(3 \times 3)$  cell, spin polarisation was included for NO and O<sub>2</sub> but was disregarded for adsorption as calculations showed that the spin disappears upon adsorption.

## 3.3 CALCULATION OF THE INTERACTIONS

Some lateral interactions could be extracted from the data presented in Ref. 28 but the data set was not sufficient for extrapolating a full set of pairwise lateral interactions for the three species (O, N and NO) adsorbed simultaneously. We have therefore done additional calculations, presented in Tables 3.2-3.4.

An important point in viewing these Tables concerns the accuracy of the DFT calculations (i.e. the DFT functionals) with some systems and particularly for the adsorption of NO on metals. Microcalorimetry experiments have shown an overestimation of the calculated adsorption energies [29]. The absolute adsorption energies have therefore not been used as an estimate of the activation energy for desorption. Table 3.2 lists the adsorption energies at low coverages. A  $p(2 \times 2)$  and a  $p(3 \times 3)$  unit

Table 3.2: Adsorption energies on Rh(111). Energies are in kJ/mol relative to the molecular gas phase species (i.e. O<sub>2</sub> for O and N<sub>2</sub> for N).

Site	Coverage (ML)	NO	O	N
fcc	0.11	-245	-195	-23
	0.25	-230	-195	-11
hcp	0.11	-248	-189	-37
	0.25	-238	-185	-20
bridge	0.11	-224	-147	-17
	0.25	-218		
top	0.11	-187		
	0.25	-184		

Table 3.3: Adsorption energies per adsorbate (averaged, kJ/mol) on Rh(111) for different ordered structures. The coverage is 0.50 ML unless otherwise stated. Energies are relative to the molecular gas phase species (i.e. O<sub>2</sub> for O and N<sub>2</sub> for N).

	NO hcp	O fcc	N hcp
p(2 × 1) rows	-212	-170	+20
	NO fcc+hcp	O fcc+hcp	N fcc+hcp
c(4 × 2) zig-zag	-232	-163	+6
(2 × 2) honeycomb	-233		
	NO fcc+hcp+top		
(2 × 2)-3NO 0.75ML	-208		

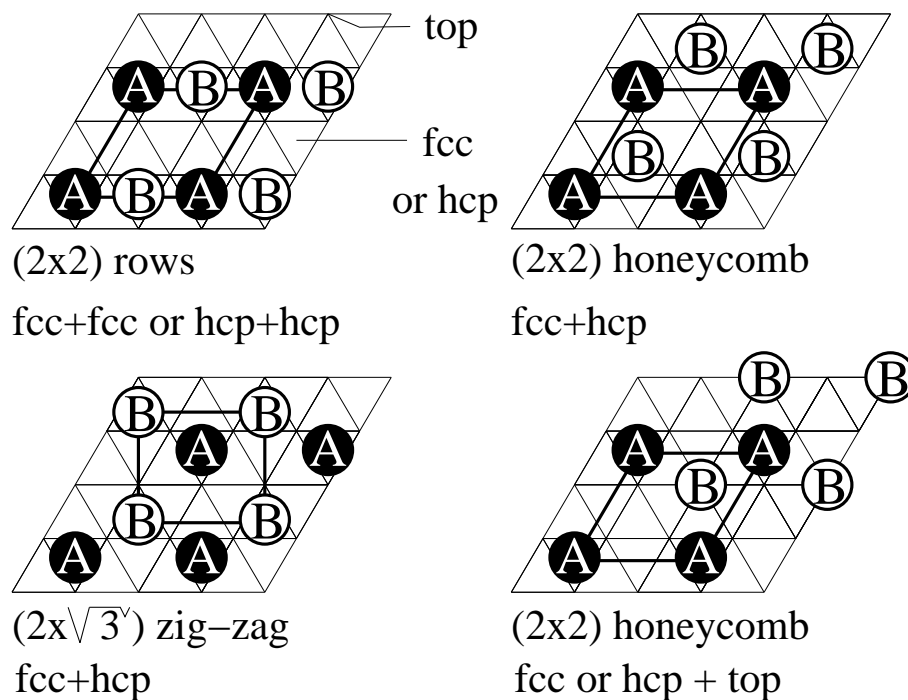


Figure 3.3: Coadsorption structures simulated using DFT.

Table 3.4: Summed adsorption energies (kJ/mol) per unit cell on Rh(111) for different ordered coadsorbed structures at 0.50 ML coverage. Each unit cell contains two (different) adsorbates. Energies are relative to the molecular gas phase species (i.e.  $O_2$  for O and  $N_2$  for N).

	NO fcc+O fcc	NO hcp+N hcp	O fcc+N fcc
(2 × 2) rows	-223	-211	-107
	NO hcp+O fcc	NO fcc+N hcp	O fcc+N hcp
(2 × $\sqrt{3}$ ) zig-zag	-403	-218	-165
	NO top+O fcc	NO top+N hcp	
(2 × 2) honeycomb	-363	-205	

Table 3.5: Lateral interactions for NO on Rh(111) (kJ/mol) at  $1 d_{\text{Rh-Rh}}$  (next-nearest neighbour) and  $2/\sqrt{3} d_{\text{Rh-Rh}}$  (next-next-nearest neighbour); three-site model using DFT-results. Since the interactions are pairwise, the lower left part of the table is identical to the upper right part. We have therefore only reported the lower left part.

	NO threefold		$(\varphi_{\text{NNN}}, \varphi_{\text{NNNN}}; \text{kJ/mol})$	
NO threefold	26, 0	NO top		
NO top	—, 5	0, —	N threefold	
N threefold	24, 16	—, 0	40, 22	O threefold
O threefold	101, 15	—, 7	46, 25	26, 26

cell were used to get the 0.25 and 0.11 ML coverage. The difference in the adsorption energy for the two different coverages is small for the top and bridge site, while the difference is in general larger for adsorbates in the threefold sites. This is due to the way the rhodium atoms settle around the adsorbate. If the difference in adsorption energy is treated as a pairwise interaction, it amounts to less than 5 kJ/mol. Because of the large separation, and the many other interactions possible at closer range, these interactions were not taken into consideration in our kMC model. As the difference in adsorption energies between threefold and bridge sites is not large it is clear that diffusion of all listed adsorbates is fast.

Table 3.3 lists the adsorption energies for higher coverages. The listed structures were chosen in such a way that the interactions could be easily determined. If more structures and a least-squares fit are used for determining the lateral interactions, they remain essentially the same. The comparison of the values in Table 3.3 with the values in Table 3.2 yields the pairwise lateral interactions for each adsorbate  $i$ :

$$\varphi(i) = (E_{\text{ads,coadsorbed}} - E_{\text{ads,alone}})/n \quad (3.12)$$

where  $n$  is the number of pairwise interactions per adsorbate in the coadsorbed structure. The pairwise additivity of the interactions is a good approximation provided that the adsorption geometry does not change much (due to lateral interactions) and the interaction energy is much smaller than the adsorption energy ( $\varphi \ll E_{\text{ads}}$ ). For example, to calculate the next-nearest neighbour interaction for O, we take the difference of the  $p(2 \times 1)$  adsorption energy (-170 kJ/mol) and the  $p(2 \times 2)$  fcc site adsorption energy (-195 kJ/mol), and divide that by the number of pair interactions at next-nearest-neighbour distance in the  $p(2 \times 1)$  structure (1). The result, 26 kJ/mol, is listed in Table 3.5. Similarly for the next-next-nearest neighbour interaction of O we take the difference between the  $c(4 \times 2)$  zig-zag adsorption energy (-163 kJ/mol) and the average  $p(2 \times 2)$  adsorption energy of fcc and hcp bound O (-190 kJ/mol), divided by one. Interactions between different kinds of adsorbates were also calculated, the ordered structures used in our calculations are shown in Figure 3.3, the summed adsorption energies are listed in Table 3.4.

The general trend in the interactions for threefold site bound adsorbates is that



the next-nearest neighbour interaction is strongly repulsive (anywhere between 25 and 100 kJ/mol) due to the bonding of both adsorbates to the same rhodium surface atoms. The next-next-nearest interaction is much smaller (0 to 25 kJ/mol). The interaction between top-bound NO and other, threefold bound, adsorbates is weakly repulsive. Because of the large repulsion at close distance we have excluded the occupation of nearest-neighbour sites ( $1/\sqrt{3}$  lattice vectors separated), and applied the lateral interactions for adsorbates at next- and next-next-nearest neighbours (1 and  $2/\sqrt{3}$  lattice vectors separated) in our kinetic Monte Carlo model.

The activation energy for the NO dissociation ( $(2 \times 2)$  structure) on a perfect Rh(111) surface has been previously determined [30]. A calculation with our system gives almost the same activation energy of 157 kJ/mol which is what we expected as the models are similar and the method identical. This activation energy is much higher than the experimental results, which can be explained by a different dissociation mechanism, most likely at steps in the surface.

### 3.4 ORDERING OF THE NO ADLAYER

We have started by simulating the adsorption of NO at low temperatures (150–225 K). At these temperatures NO adsorbs molecularly; dissociation only starts above 275 K [12]. In our simulations of the adsorption of NO, the threefold sites are occupied first, since they are energetically more favourable. Above 0.40 ML adsorbates start forming patches of ordered structures. Two ordered structures (Figure 3.4) are encountered over the entire simulated temperature range (125–225 K), first the experimentally found  $c(4 \times 2)$ -2NO structure, in which each adsorbed NO has two nearest-neighbours. The other ordered structure is a  $(2 \times 2)$ -2NO structure, with one adsorbate fcc, one adsorbate hcp, arranged in a honeycomb-lattice. Every adsorbate has three nearest neighbours. The  $c(4 \times 2)$ -2NO structure can be transformed into the  $(2 \times 2)$ -2NO structure by shifting each second zig-zag row by one lattice vector. The difference in adsorption energy between the two structures equals half a next-next-nearest neighbour NO-NO interaction per adsorbate; each NO having one interaction in the  $c(4 \times 2)$ -2NO structure, and 1.5 in the  $(2 \times 2)$ -2NO structure. Both structures are therefore equal in energy when the DFT-based next-next-nearest neighbour NO-NO interaction of 0 kJ/mol is used. Since this value has a non-negligible error margin, we have investigated interactions between 0 and 4 kJ/mol repulsive. The  $(2 \times 2)$ -2NO structure dominates at 0.50 ML in the absence of a next-next-nearest neighbour lateral interaction, resulting in many small ordered islands of 50–200 adsorbates (Figure 3.5). In the case of a small repulsive next-next-nearest neighbour lateral interaction, the  $c(4 \times 2)$ -2NO structure dominates, with island sizes of 50–200 adsorbates for an interaction of 2 kJ/mol, and up to over 1000 adsorbates for an interaction of 4 kJ/mol (not shown). The basic cause for ordering at this coverage is the avoidance of occupying next-nearest-neighbour sites and/or low adsorption energy (i.e. top) sites.

If the coverage is gradually increased to values above 0.50 ML, the NO molecules are forced to either adsorb close to each other (next-nearest-neighbour position, re-

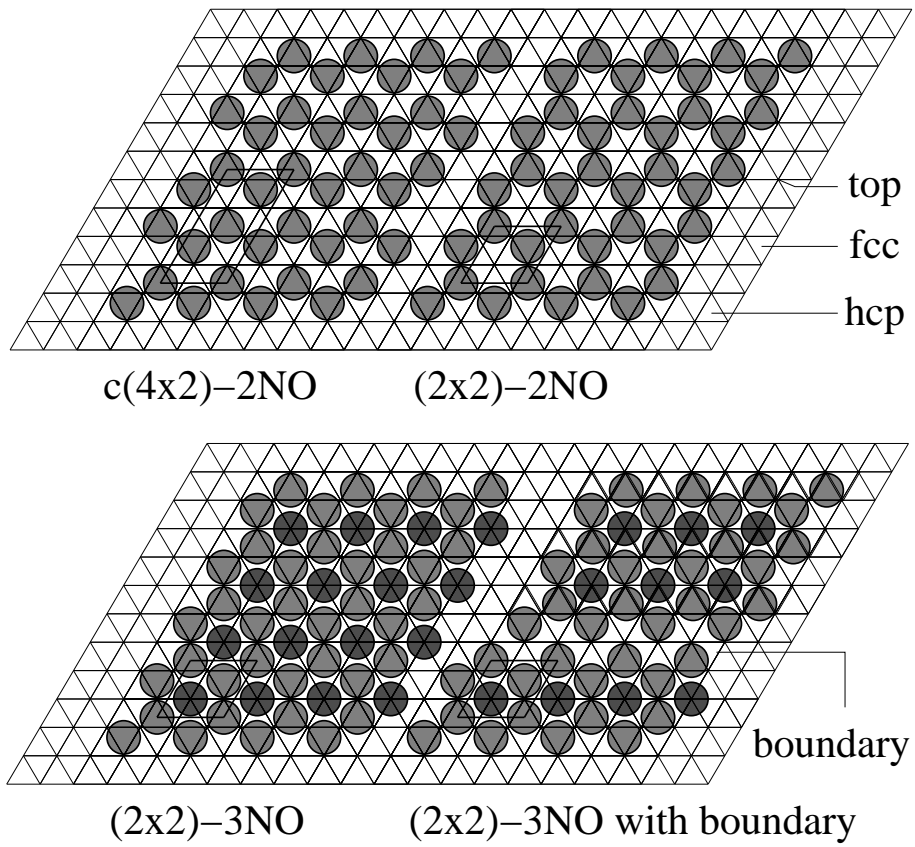


Figure 3.4: Ordered structures of NO on Rh(111). The light grey circles indicate threefold bound NO, the dark grey circles top bound NO.

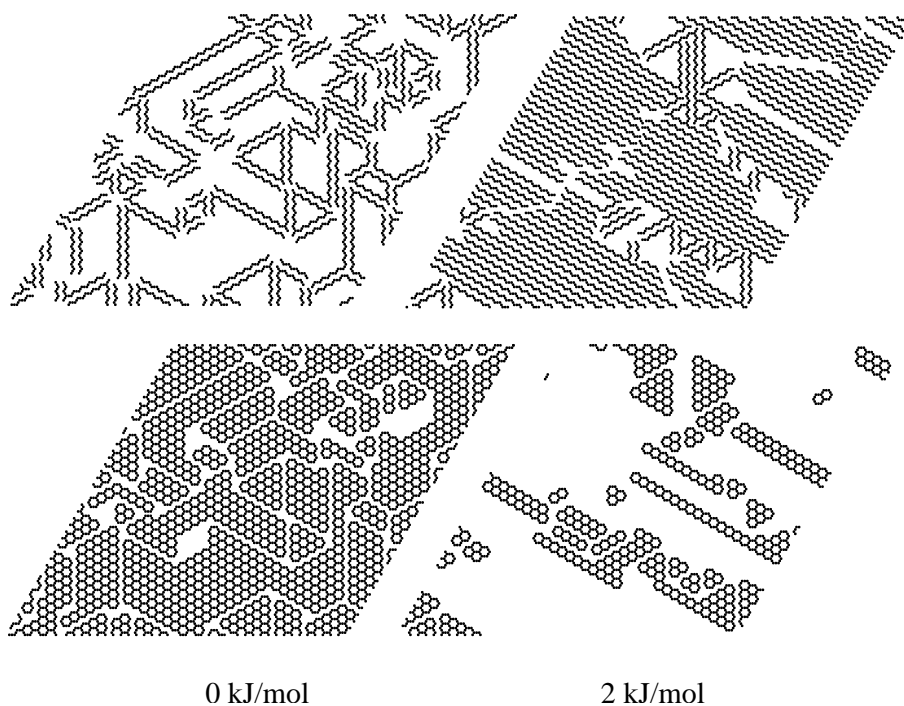


Figure 3.5: Adsorbate distribution after adsorption at 225 K and 0.50 ML for a next-nearest neighbour NO-NO repulsion of 0 (left) and 2 kJ/mol (right). Since the ordering is hard to recognise from the original output, two separate images are displayed for each result, with the characteristic zig-zag lines of the  $c(4 \times 2)$ -2NO structure (upper panels) or the hexagons of the  $(2 \times 2)$ -2NO structure (lower panels) emphasised. Snapshot of  $76 \times 76 d_{\text{Rh-Rh}}$ .

sulting in a 26 kJ/mol repulsion per interaction) or to adsorb on an other kind of sites, the top sites (47 kJ/mol less stable). Experimentally the top sites are found to become occupied. The top sites have a lower adsorption energy, but a structure can be formed with lower repulsive interactions and a high coverage of 0.75 ML. The adsorbates in this structure form a hexagonal packing, which is as dense as can be without next-nearest neighbour interactions. In our model, this  $(2 \times 2)$ -3NO structure is also found. The islands are separated by  $c(4 \times 2)$ -2NO-like domains (2 zig-zag lines, then another  $(2 \times 2)$ -3NO domain, Figure 3.4). For a zero next-next-nearest neighbour lateral interaction, the  $(2 \times 2)$ -3NO structure is easily formed at high diffusion and at 225 K. For lower temperatures, the structure is formed less readily, and the saturation coverage diminishes from 0.75 ML at 225 K to 0.65 at 150 K, in agreement with experimental results [7]. Because of the lateral interactions the threefold and top sites get approximately equal effective adsorption energies during the formation of the  $(2 \times 2)$ -3NO structure. This results in a very fast hopping of NO from top sites to neighbouring threefold sites and back, until another NO molecule moves in to block diffusion to the threefold site. This forced us to reduce the prefactor for top-to-threefold and threefold-to-top diffusion with respect to the prefactor for threefold-to-threefold diffusion, but tests with equal prefactors showed no noticeable influence on the results.

For a non-zero next-next-nearest neighbour lateral interaction during adsorption at 0.50 ML large  $c(4 \times 2)$ -2NO islands are formed, which hardly reconstruct. This slow conversion of the  $c(4 \times 2)$ -2NO islands into the  $(2 \times 2)$ -3NO structure is due to several factors. First, the strong next-nearest neighbour lateral interaction of 26 kJ/mol prevents restructuring from within the islands, so reconstruction has to take place at the edges of the islands. Another factor may be that reconstruction occurs through bridge sites, which were not explicitly incorporated in our model. Last, the effective adsorption rate is in reality higher than in our model because of precursor adsorption behaviour. Tests with increased adsorption rates and/or defects in the  $c(4 \times 2)$ -2NO adlayer give, as expected, a faster conversion into the  $(2 \times 2)$ -3NO structure.

Increasing the coverage above 0.75 ML causes adsorbates to occupy next-nearest-neighbour positions. Since the repulsion between two next-nearest-neighbour NO molecules is relatively strong (26 kJ/mol), 0.75 ML is the saturation coverage at low temperatures and under UHV conditions. Under high pressures and higher temperatures, however, another ordered structure for NO on Rh(111) was recently discovered with a slightly higher coverage (0.778 ML). This structure does involve next-nearest neighbour lateral interactions between the adsorbates, but these are compensated by having less adsorbates in the high-energy top sites, resulting in comparable energies for both structures [31]. It is interesting to note that with only minor changes in lateral interactions we could also reproduce this structure. In this paper we restrict ourselves to coverages up to 0.75 ML, however.

We conclude this section with a series of snapshots during NO adsorption. The underlying lattice is not displayed. These snapshots show some typical configurations for the intermediate stages between the ordered structures. Figure 3.6 shows the onset of  $c(4 \times 2)$ -2NO domain formation, with also some small  $(2 \times 2)$ -2NO domains present. The same area at higher coverage (Figure 3.7) shows the same  $c(4 \times 2)$ -2NO domains,

Table 3.6: Lateral interactions for NO on Rh(111) (kJ/mol) at  $1 d_{\text{Rh-Rh}}$  (nearest neighbour) in the single-site model. Since the interactions are pairwise, the lower left part of the table is identical to the upper right part. We have therefore only reported the lower left part.

	NO threefold	$(\varphi_{\text{NN}}; \text{kJ/mol})$	
NO threefold	0	N threefold	
N threefold	12.5	8	O threefold
O threefold	12.5	0	2

and around them  $(2 \times 2)$ -3NO domains. The  $c(4 \times 2)$ -2NO domains rearrange from the outer boundaries, not from the inside out. Finally, at coverages close to saturation, the  $(2 \times 2)$ -3NO domains are separated by  $c(4 \times 2)$ -2NO-like domain boundaries (Figure 3.8).

### 3.5 TEMPERATURE PROGRAMMED DESORPTION

#### 3.5.1 SINGLE-SITE MODEL

We first performed simulations with the single-site model [14, 19], which was very well able to reproduce the TPD-spectra, but, since it was only a single-site model, could not reproduce the correct spatial ordering of adsorbates on the surface. Adsorbates in this model occupy neighbouring sites at higher coverages, i.e., sites one lattice vector apart. We show here examples at two different coverages, 0.50 and 0.75 ML (Figure 3.9). At 0.50 ML, each NO has two neighbours at one lattice vector distance, while in the three-site model and in the experiment it is found that each NO has two neighbours at a larger distance,  $2/\sqrt{3}$  lattice vectors apart. At a coverage of 0.75 ML, the number of neighbours at one lattice vector distance even increases to four. In the three-site model and the experiment on the other hand, the number of neighbouring NO molecules increases to six, but they are still separated  $2/\sqrt{3}$  lattice vectors separated from each other.

Since large lateral interactions at nearest-neighbour distance in the single-site model caused blocked adsorption and premature desorption (i.e., at lower temperatures), the interactions had to be decreased to much lower values in order to reproduce the TPD spectra. The lateral interactions in that model (Table 3.6) were therefore at odds with the DFT calculations of Loffreda *et al.* [28] and our results in Table 3.5.

#### 3.5.2 THREE-SITE MODEL

This discrepancy between the actual lateral interactions and adsorbate distribution and the ones in our single-site model led us to do simulations on the more elaborate three-site model. In this model the experimentally found ordered structures are reproduced,

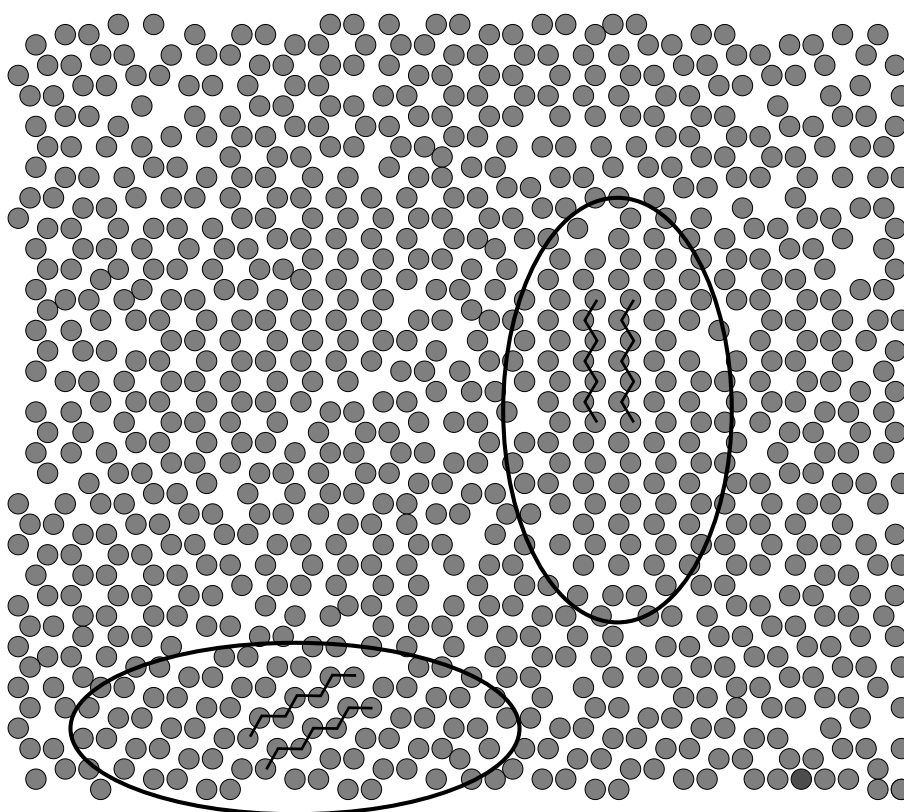


Figure 3.6: Typical configuration of the adlayer after adsorption of 0.47 ML NO, showing the onset of  $c(4 \times 2)$ -2NO domain formation (indicated by the ovals and the zig-zag lines). Snapshot of  $40 \times 40$   $d_{\text{Rh-Rh}}$ . The light grey circles indicate threefold bound NO, the dark grey circles top bound NO.

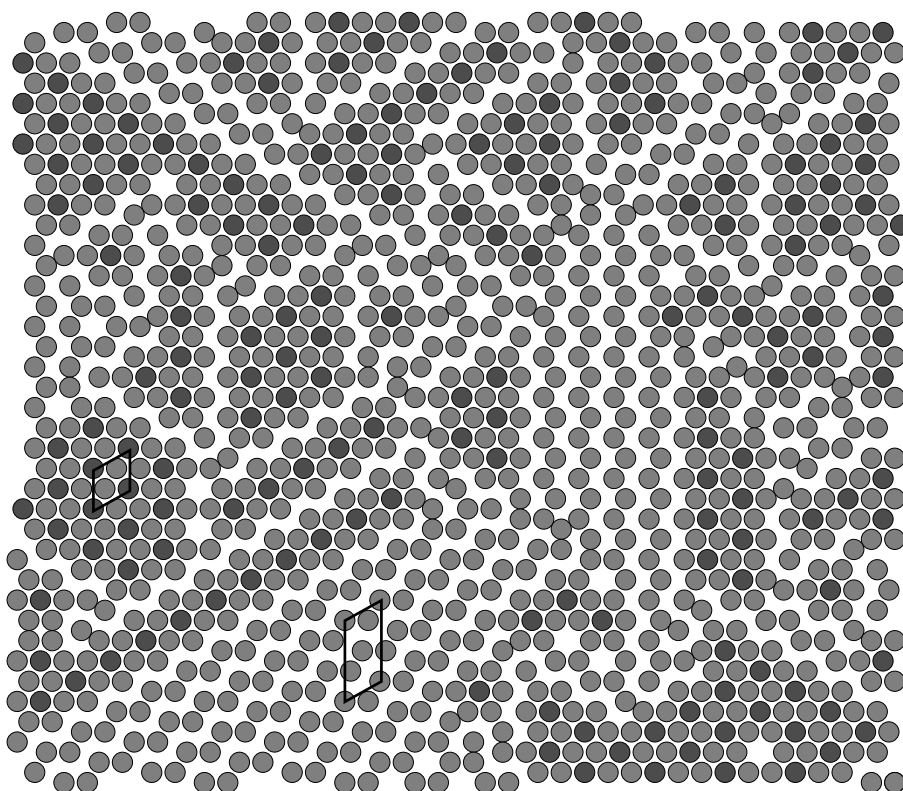


Figure 3.7: Typical configuration of the adlayer after adsorption of 0.60 ML NO, showing the transformation of the  $c(4 \times 2)$ -2NO domains into  $(2 \times 2)$ -3NO domains. Since the unit cells are similar in shape,  $c(4 \times 2)$ -2NO domains coexist with  $(2 \times 2)$ -3NO domains. The light grey circles indicate threefold bound NO, the dark grey circles top bound NO.

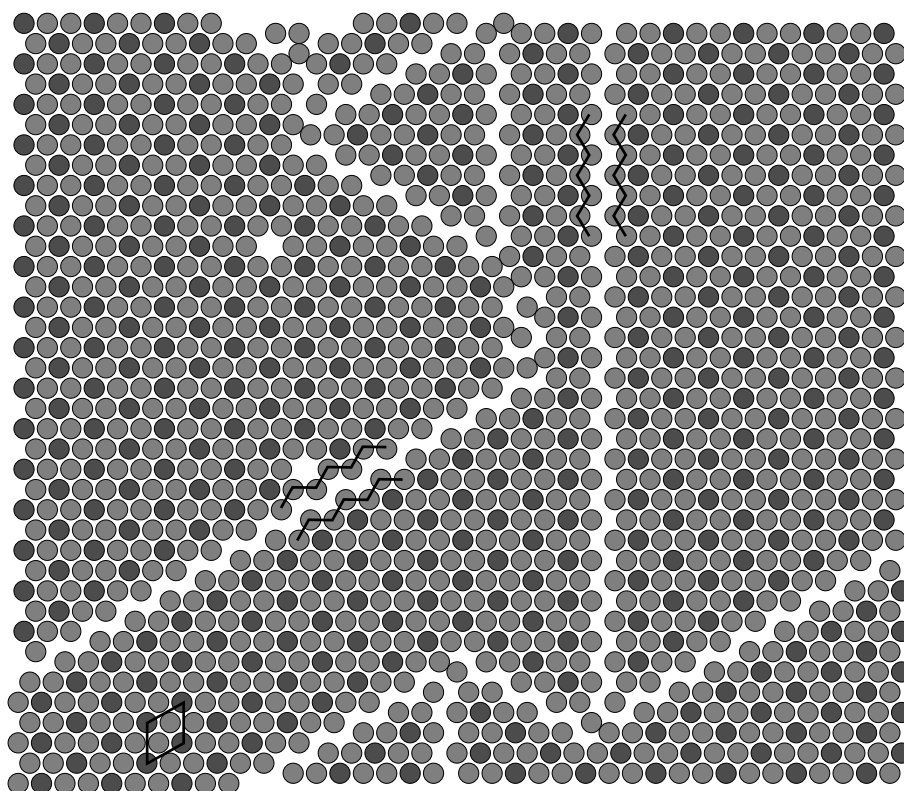


Figure 3.8: Typical configuration of the adlayer after adsorption of 0.71 ML NO. The surface is covered in large  $(2 \times 2)$ -3NO domains, separated by  $c(4 \times 2)$ -2NO-like domain walls (indicated by the zig-zag lines). The  $(2 \times 2)$ -3NO unit cell is indicated. The light grey circles indicate threefold bound NO, the dark grey circles top bound NO.



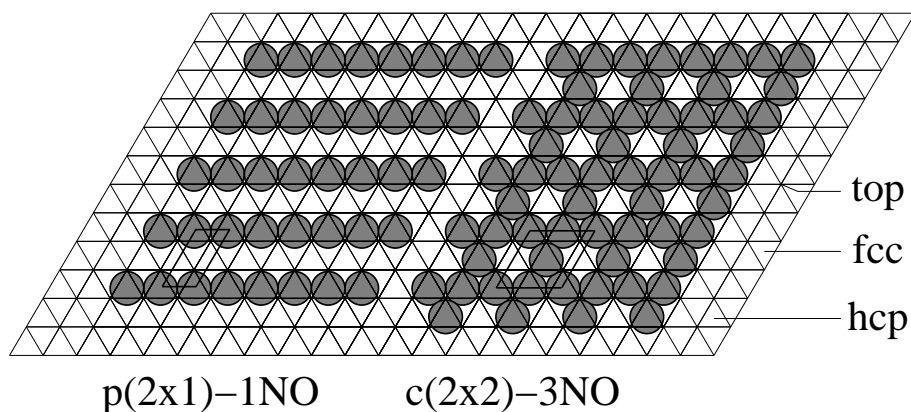


Figure 3.9: Minimum energy adsorption structures at 0.50 ML (left) and 0.75 ML (right) in the single-site model. All NO molecules are bound to threefold sites.

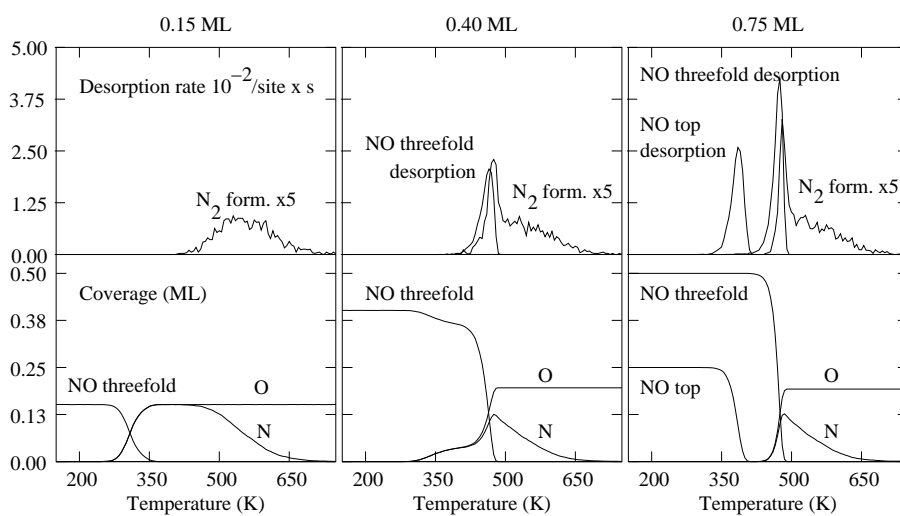


Figure 3.10: NO and N<sub>2</sub> desorption rates (top), and NO, nitrogen and oxygen coverages (bottom), during temperature programmed reaction and desorption. Starting coverages are (from left panel to right) 0.15, 0.40 and 0.75 ML. N<sub>2</sub> desorption rates have been multiplied by 5; the heating rate was 10 K/s.

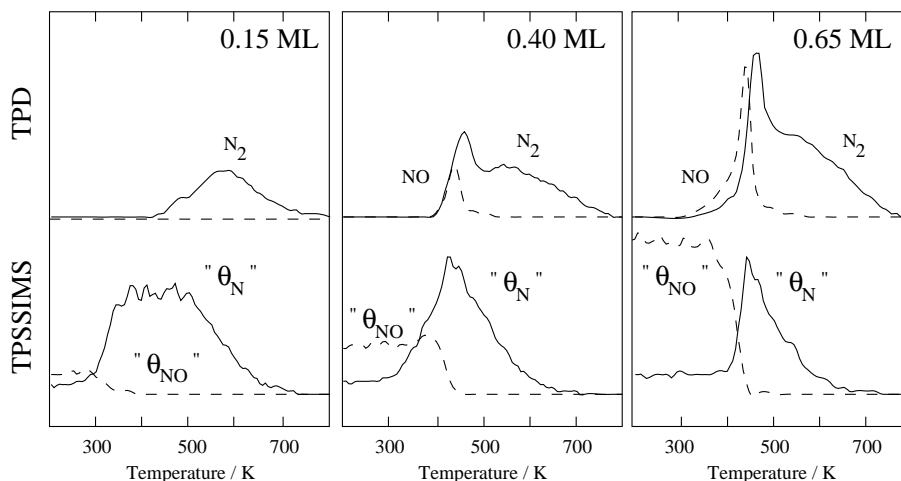


Figure 3.11: The NO (---) and  $N_2$  (—) TPD rates (top), and  $\Sigma_{n=1,2}Rh_nNO^+/Rh_n^+$  (---) and  $Rh_2N^+/Rh_2^+$  (—) TPSSIMS ion intensity ratios (bottom), during the temperature programmed reaction of NO on Rh(111) for low (left panel), medium (central panel) and high (right panel) initial NO coverages. The NO TPD spectra have been divided by a factor 4 with respect to the  $N_2$  TPD spectra. The adsorption temperature was 100 K; the heating rate was 10 K/s. Adapted from Ref. 12.

and the lateral interactions are consistent with the values derived from the DFT calculations. Figure 3.10 shows a set of simulated TPD spectra, which closely resemble the experimental spectra previously published in Ref. 12 and here reproduced in Figure 3.11. The low coverage region (left), with a coverage below 0.20 ML, is characterised by dissociation of all NO. NO occupies threefold sites. Dissociation starts at 275 K, and is complete just above 350 K. Nitrogen formation occurs in a wide second order peak between 450 and 650 K. The dissociation is not hampered by a lack of accessible sites at these coverages, since even after dissociation of all NO the total coverage is only 0.40 ML. No desorption of NO takes place, since dissociation is faster than desorption. We distinguish between free and accessible sites, since even for saturated overlayers there are many non-occupied or free sites, but these are not accessible for molecules to bind to since this would cause a large repulsion with the neighbouring adsorbates.

The medium coverage region (between 0.20 and 0.50 ML, centre) is characterised by partial decomposition of threefold NO. N and O form islands (local coverage 0.30-0.35 ML, unordered) separated from the NO islands; dissociation stops when the NO islands are compressed into an ordered structure of 0.50 ML coverage. The formation of separate N+O and NO islands can be explained by a closer look at the lateral interactions (Table 3.5). NO adsorbates can be packed together at next-next-nearest

neighbour distance without a penalty, while this is not possible for nitrogen or oxygen adatoms. If the adlayer is therefore allowed to relax, then the adlayer will try to remove most of the interactions, or at least the stronger ones. This is most easily done by compressing the NO-islands to a local coverage of 0.50 ML, while leaving the N+O islands untouched. Nitrogen and oxygen both have considerable interactions at next-next-nearest neighbour distance; they therefore do not approach each other to such close proximity. More NO can only dissociate when part of the NO desorbs, above 400 K.

This clearly demonstrates the influence of the lateral interactions: NO dissociation causes an increase in coverage. Because of the increase in coverage, the amount of repulsion increases, and the dissociation becomes more difficult. The dissociation process therefore becomes more and more difficult until it just stops. There are still empty sites present, but the activation energy for dissociation is too high due to all the repulsions. A similar segregation into islands was seen in co-adsorption experiments of NO+N and NO+O by Xu *et al.* [32]. Only after the onset of desorption of NO at around 425 K are some more accessible sites (i.e., sites with less neighbouring adsorbates) generated, and can dissociation proceed. The result is that (for this coverage of 0.40 ML) 50% of the NO desorbs, and the other 50% dissociates, causing the formation of 0.20 ML N atoms (which readily desorbs as N<sub>2</sub>) and 0.20 ML of O atoms which stay on the surface. The desorption of nitrogen gas occurs in two peaks, one almost coinciding with the NO desorption peak, the other one much wider and at higher temperatures. This coincidence of the first peak is caused by the fast formation of N atoms on one hand and the repulsive interactions still present at 450 K. After the NO has disappeared there are few interactions, the activation energy for nitrogen formation is higher and the remaining N atoms on the surface desorb in a broad peak.

At coverages close to saturation (above 0.50 ML), dissociation is completely inhibited up to 400 K (right). Top bound NO desorbs around 380 K, but does not create the vacancies needed for dissociation. After the desorption of threefold NO above 400 K, dissociation proceeds, and nitrogen formation occurs in a first and a second order peak. This total blockage of dissociation is due to the absence of accessible sites. When the top-bound NO desorbs, top sites are freed, but these are not capable of binding N or O adatoms. Dissociation is therefore suppressed until the desorption of threefold-bound NO. Then dissociation and desorption compete again, with 0.20 ML NO dissociating and the rest desorbing. The amount of NO that dissociates therefore does not increase with NO starting coverage increasing from 0.40 to 0.75 ML. This maximum amount of dissociated NO is directly related to the competition between desorption and dissociation, since it is known that upon re-adsorption of NO higher N+O coverages can be generated. The amount of dissociated and desorbed NO versus initial NO coverage thus shows the following trend: below 0.20 ML initial coverage all NO dissociates, above 0.20 ML initial coverage 0.20 ML NO dissociates and the rest desorbs. Experimentally this was also measured. Borg *et al.* [12] found that for initial coverages up to 0.25 ML all NO dissociates, and that for higher coverages NO both dissociates and desorbs. The amount of dissociated NO increases with the initial NO coverage, even for coverages larger than 0.25 ML. Hardeveld [33] on the other

hand found that for initial coverages up to 0.20 ML all NO dissociates. Between 0.20 and 0.45 ML initial coverage 0.20 ML NO dissociates while the rest desorbs. For coverages above 0.45 ML a further increase in the amount of dissociated NO was found while the amount of desorbed NO remained constant. Aryafar *et al.* [18] have also shown that for coverages up to 0.20 ML all NO dissociates with little NO desorption. They found that at higher coverages 0.20 ML NO dissociates, the rest desorbs molecularly.

### 3.6 DISCUSSION

It should be noted that in order to keep the model more simple, we modelled the dissociation reaction and the recombination of nitrogen on the terrace, although there is considerable experimental evidence that these in fact occur at steps in the surface [15, 34–37]. In the case that diffusion to the steps is fast, the reaction at the steps can be modelled as a reaction on the terrace with a correction in the prefactor to account for the fraction of active sites. The prefactor for the terrace reaction rate constant then becomes the fraction of steps times the prefactor of the reaction rate constant at the steps. Since diffusion of NO, N and O is fast with respect to the reactions, the condition holds and the macroscopic rates are the same. As for the spatial distribution of adsorbates, it is expected that a similar segregation into separate N+O and NO islands will be seen for the step-reaction, since also in this case the empty sites on the surface will be filled causing compression of the adlayer. A similar suppression of dissociation will be caused by the lack of empty terrace sites, and the fractions of desorbed and dissociated NO will therefore also be comparable. Thus we conclude that despite the omission of steps in our model, the simulations presented here are able to describe the most important experimental features.

Comparing our results for Rh(111) with the results for Rh(100), we see that both surfaces show lateral-interactions-induced blocking of dissociation, which can be well reproduced by assuming pairwise interactions [13]. Similar coverage regions were found and reproduced, for respectively unhampered dissociation, partial dissociation, and absence of dissociation up to desorption of NO. The lateral-interactions-induced occupation of a second type of site at higher coverages was also seen on Rh(100), but not modelled. No ordered structures were observed upon adsorption of NO on Rh(100), contrary to Rh(111). The role of steps in the reactions is thought to be less dominant on the (100) surface since this surface is more open and reactive.

### 3.7 CONCLUSIONS

We have successfully reproduced the ordering behaviour of NO on Rh(111) during adsorption and the temperature programmed desorption (TPD) of NO from Rh(111) under UHV conditions using a kinetic Monte Carlo model involving lateral interactions derived from DFT calculations and different adsorption sites (top, fcc and hcp). The formation of  $c(4 \times 2)$ -2NO domains at 0.50 ML coverage strongly depends on the

next-next-nearest-neighbour repulsion between the NO adsorbates used in the model. The formation of the  $(2 \times 2)$ -3NO structure at higher coverage follows from the avoidance of the strong next-nearest-neighbour repulsion in favour of the occupation of the top sites.

A single-site model was able to reproduce the experimental TPD, but the lateral interactions were at odds with the values of the DFT calculations. A three-site model resolved this problem. All NO dissociates during TPD for initial coverages of NO below 0.20 ML. For NO coverages larger than 0.20 ML, 0.20 ML NO dissociates while the rest desorbs. This is due to a lack of accessible sites on the surface, i.e., sites where a molecule can bind without experiencing large repulsions with neighbouring adsorbates. For NO coverages above 0.20 ML, the dissociation of NO causes a segregation into separate NO and N+O islands. The dissociation causes the surface to be filled with adsorbates, and the adsorbates are therefore pushed closer together. NO on one hand can easily be compressed into islands of 0.50 ML coverage, because there is no large next-next-nearest-neighbour repulsion. N+O on the other hand form islands with a lower coverage (0.30-0.35 ML) due to the considerable next-next-nearest-neighbour repulsion. Top bound NO (above 0.50 ML initial coverage) does not contribute to the amount of NO dissociated during TPD, it desorbs in a separate peak at 380 K. Instead, dissociation is blocked until the desorption of threefold bound NO.

This chapter has been published as: C. G. M. Hermse, F. Frechard, A. P. van Bavel, J. J. Lukkien, J. W. Niemantsverdriet, R. A. van Santen and A. P. J. Jansen; Combining density-functional calculations with kinetic models: NO/Rh(111); *J. Chem. Phys.*, 118 (15): 7081–7089, 2003.

- [1] C.-T. Kao, G. S. Blackman, M. A. van Hove and G. A. Somorjai; The surface structure and chemical reactivity of Rh(111)-(2x2)-3NO by HREELS and dynamical LEED analysis; *Surf. Sci.*, 224: 77–96, 1989.
- [2] I. Zasada, M. A. van Hove and G. A. Somorjai; Reanalysis of the Rh(111)+(2x2)-3NO structure using automated tensor LEED; *Surf. Sci.*, 418: L89–L93, 1998.
- [3] N. Materer, A. Barbieri, D. Gardin, U. Starke, J. D. Batteas and M. A. van Hove; Dynamical leed analyses of the Pt(111)-p(2x2)-NO and the Ni(111)-c(4x2)-2NO structures: substrate relaxation and unexpected hollow-site adsorption; *Surf. Sci.*, 303: 319–332, 1994.
- [4] K. H. Hansen, Z. Slijivancanin, B. Hammer, E. Laegsgaard, F. Besenbacher and I. Stensgaard; An STM and DFT study of the ordered structures of NO on Pd(111); *Surf. Sci.*, 496: 1–9, 2002.
- [5] S. Surnev, M. Sock, M. G. Ramsey, F. P. Netzer, M. Wiklund, M. Borg and J. N. Andersen; CO adsorption on Pd(111): a high-resolution core level photoemission and electron energy loss spectroscopy study; *Surf. Sci.*, 470: 171–185, 2000.
- [6] M. K. Rose, T. Mitsui, J. Dunphy, A. Borg, D. F. Ogletree, M. Salmeron and P. Sautet; Ordered structures of CO on Pd(111) studied by STM; *Surf. Sci.*, 512: 48–60, 2002.
- [7] T. W. Root, L. D. Schmidt and G. B. Fisher; Adsorption and reaction of nitric oxide and oxygen on Rh(111); *Surf. Sci.*, 134: 30–45, 1983.
- [8] J. F. Zhu, M. Kinne, T. Fuhrmann, R. Denedcke and H.-P. Steinruck; In situ high-resolution XPS studies on adsorption of NO on Pt(111); *Surf. Sci.*, 529: 384–396, 2003.
- [9] M. Stichler and D. Menzel; The geometry of the saturated (2x2)-NO adlayer on Ru(001): a structure with three different sites; *Surf. Sci.*, 391: 47–58, 1997.
- [10] P. Cernota, K. Rider, H. A. Yoon, M. Salmeron and G. Somorjai; Dense structures formed by CO on Rh(111) studied by scanning tunneling microscopy; *Surf. Sci.*, 445: 249–255, 2000.
- [11] R. Linke, D. Curulla, M. J. P. Hopstaken and J. W. Niemantsverdriet; CO/Rh(111): vibrational frequency shifts and lateral interactions in adsorbate layers; *J. Chem. Phys.*, 115(17): 8209–8216, 2001.
- [12] H. J. Borg, J. F. C.-J. Reijerse, R. A. van Santen and J. W. Niemantsverdriet; The dissociation kinetics of NO on Rh(111) as studied by temperature programmed static secondary ion mass spectrometry and desorption; *J. Chem. Phys.*, 101(11): 10052–10063, 1994.
- [13] A. P. van Bavel, C. G. M. Hermse, M. J. P. Hopstaken, A. P. J. Jansen, J. J. Lukkien, P. A. J. Hilbers and J. W. Niemantsverdriet; Quantifying lateral adsorbate interactions by kinetic Monte-Carlo simulations and density-functional theory: NO dissociation on Rh(100); *Phys. Chem. Chem. Phys.*, 6: 1830–1836, 2004.
- [14] R. M. van Hardeveld, M. J. P. Hopstaken, J. J. Lukkien, P. A. J. Hilbers, A. P. J. Jansen, R. A. van Santen and J. W. Niemantsverdriet; Role of surface diffusion in the ordering of adsorbed molecules: dynamic Monte Carlo simulations of NO on Rh(111); *Chem. Phys. Lett.*, 302: 98–102, 1999.
- [15] L. A. DeLouise and N. Winograd; Adsorption and desorption of NO from Rh(111) and Rh(331) surfaces; *Surf. Sci.*, 159: 199–213, 1985.
- [16] T. W. Root, G. B. Fisher and L. D. Schmidt; Electron energy loss characterization of NO on Rh(111). I. NO coordination and dissociation; *J. Chem. Phys.*, 85(8): 4679–4686, 1986.
- [17] Y. J. Kim, S. Thevuthasan, G. S. Herman, C. H. F. Peden, S. A. Chambers, D. N. Belton and H. Permana; Chemisorption geometry of NO on Rh(111) by x-ray photoelectron

- diffraction; *Surf. Sci.*, 359: 269–279, 1996.
- [18] M. Aryafar and F. Zaera; Isothermal kinetic study of the decomposition of nitric oxide over Rh(111) surfaces; *J. Catal.*, 175: 316–327, 1998.
- [19] R. M. Nieminen and A. P. J. Jansen; Monte Carlo simulations of surface reactions; *Appl. Catal. A*, 160: 99–123, 1997.
- [20] E. W. Hansen and M. Neurock; First-principles-based Monte-Carlo methodology applied to O/Rh(100); *Surf. Sci.*, 464: 91–107, 2000.
- [21] K. Honkala, P. Pirilä and K. Laasonen; Coadsorption of CO and NO on the Pd(111) surface: combined ab initio and Monte Carlo study; *Phys. Rev. Lett.*, 86(26): 5942–5945, 2001.
- [22] C. Stampfl, H. J. Kreuzer, S. H. Payne, H. Pfnür and M. Scheffler; First-principles theory of surface thermodynamics and kinetics; *Phys. Rev. Lett.*, 83(15): 2993–2996, 1999.
- [23] G. Kresse and J. Furthmüller; Efficiency of ab-initio total energy calculations for metals and semiconductors using a plane-wave basis set; *Comput. Mater. Sci.*, 6(1): 15–50, 1996.
- [24] G. Kresse and J. Furthmüller; Efficient iterative schemes for ab initio total-energy calculations using a plane-wave basis set; *Phys. Rev. B*, 54(16): 11169–11186, 1996.
- [25] J. P. Perdew; *Electronic Structure of Solids '91*, chapter Unified Theory of Exchange and Correlation Beyond the Local Density Approximation, page 11; Akademie Verlag, Berlin, 1991.
- [26] D. Vanderbilt; Soft self-consistent pseudopotentials in a generalized eigenvalue formalism; *Phys. Rev. B*, 41(11): 7892–7895, 1990.
- [27] G. Kresse and J. Hafner; Norm-conserving and ultrasoft pseudopotentials for first-row and transition elements; *J. Phys.: Condens. Matter*, 6(40): 8245–8257, 1994.
- [28] D. Loffreda, D. Simon and P. Sautet; Molecular and dissociative chemisorption of NO on palladium and rhodium (100) and (111) surfaces: A density-functional periodic study; *J. Chem. Phys.*, 108(15): 6447–6457, 1998.
- [29] Q. Ge, R. Kose and D. A. King; Adsorption energetics and bonding from femtomole calorimetry and from first principles theory; *Adv. Catal.*, 45: 207–259, 2000.
- [30] David Loffreda; *Modélisation théorique de l'adsorption et de la réactivité de la molécule NO sur les surfaces de catalyseurs à base de palladium, de rhodium et d'alliages palladium-manganèse*; PhD thesis, Université Claude Bernard-Lyon 1, 1999.
- [31] K. B. Rider, K. S. Hwang, M. Salmeron and G. A. Somorjai; Structure and dynamics of dense monolayers of NO adsorbed on Rh(111) in equilibrium with the gas phase in the Torr pressure range; *Phys. Rev. Lett.*, 86(19): 4330–4333, 2001.
- [32] H. Xu and K. Y. S. Ng; Molecular NO islands versus O and N islands on Rh(111) surface studied by scanning tunneling microscopy; *Surf. Sci.*, 365: 779–788, 1996.
- [33] Martijn van Hardeveld; *Elementary reactions in the catalytic reduction of NO on rhodium surfaces*; PhD thesis, Eindhoven University of Technology, 1997.
- [34] N. M. H. Janssen, A. R. Cholach, M. Ikai, K. Tanaka and B. E. Nieuwenhuys; The interaction of NO with stepped Rh surfaces; *Surf. Sci.*, 382: 201–213, 1997.
- [35] F. Esch, A. Baraldi, C. Comelli, S. Lizzit, M. Kiskinova, P. D. Cobden and B. E. Nieuwenhuys; Atomic nitrogen on steps: A fast x-ray photoelectron spectroscopy study of the NO uptake on Rh(533), Rh(311) and Rh(111); *J. Chem. Phys.*, 110(8): 4013–4019, 1999.
- [36] S. Dahl, A. Logadottir, R. C. Egeberg, J. H. Larsen and I. Chorkendorf; Role of steps in N<sub>2</sub> activation on Ru(0001); *Phys. Rev. Lett.*, 83(9): 1814–1817, 1999.
- [37] M. Ikai, N. M. H. Janssen, B. E. Nieuwenhuys and K. Tanaka; Spatial distribution of N<sub>2</sub> and NO desorbing from a Rh(533) surface; *J. Chem. Phys.*, 106(1): 311–320, 1997.

## CHAPTER 4

# CHIRAL DOMAINS: TARTARIC ACID ON Cu(110)

To explain the formation of the asymmetric  $(9\ 0, 1\ 2)$  structure for  $(R,R)$ -bitartrate on the unreconstructed Cu(110) surface we propose a model that takes into account the relevant interactions with the first and second shell of neighbours and the influence of an adsorbate-induced surface stress. We suggest that the surface stress occurs in the  $[1\bar{1}0]$  direction, when more than three carboxylate groups bind next to each other to the same copper row. This stress is released if two or more copper atoms are left vacant between them. Employing kinetic Monte Carlo simulations this model was tested using electronic structure calculations based parameters, reproducing the experimental  $(9\ 0, 1\ 2)$   $(R,R)$ -bitartrate structure. This confirms the proposal that the empty trough is formed to release the surface stress caused by adsorption of  $(R,R)$ -bitartrate. This also leads us to suggest that a similar mechanism is responsible for the formation of empty troughs in other ordered structures, created by adsorption of similar molecules, such as acetate and succinate, on the Cu(110) surface.

### 4.1 INTRODUCTION

The development of enantioselective heterogeneous catalysts has received a lot of attention in the past decades [1–5]. Such heterogeneous catalysts, which are able to synthesise one optical isomer with an enantiomeric excess from a pro-chiral reagent, have an extreme importance for pharmaceutical and chemical industries. This is because the effect of each enantiomer of a drug is often different in living beings. One enantiomer may be much more active than the other one, or, which is worse, one enantiomer may be harmful while the other enantiomer is wholesome. In synthesising drugs one therefore always strives to produce only the desired enantiomer. The benefit



of having an enantioselective heterogeneous catalyst is not only due to the production of the chiral molecule itself (with high selectivity), but also due to the catalyst, which is easier to handle and to separate than most of the currently used homogeneous ones.

Among different strategies for the preparation of these chiral heterogeneous catalysts, an interesting approach is to modify the surface of an “ordinary” catalyst by adsorbing chiral modifiers. One example of such application is the enantioselective hydrogenation reaction of  $\beta$ -ketoesters on Ni catalysts, modified by an initial adsorption of tartaric acid [6–12]. Tartaric acid is a bi-acid with the formula  $\text{HOOC-C}^*\text{HOH-C}^*\text{HOH-COOH}$ , where the \* denotes a chiral carbon atom.

Scanning tunnelling microscopy (STM) studies of the adsorption of tartaric acid chiral modifiers on a model catalyst surface, Cu(110), have revealed that each isomer forms different chemisorption domains, where the domain of the (*R,R*)-isomer is the mirror image of the domain formed by the (*S,S*)-isomer [13–15].

These chiral domains of tartaric acid are found to be formed by its bitartrate form. They follow a 2-dimensional ordered structure. For example, in the case of the (*R,R*)-isomer the supramolecular assembly can be described by the following matrix notation, which defines the unit cell unambiguously [16]:

$$M_{R,R} = \begin{pmatrix} 9 & 0 \\ 1 & 2 \end{pmatrix}$$

This matrix notation will be referred to as (9 0,1 2) in the text.

The molecules form extended molecular rows along the  $\langle 1\bar{1}4 \rangle$  direction. These parallel rows are assembled in groups of three, each group being separated from the next by an empty space (trough), see Figure 4.1. These troughs can provide a chiral adsorption site on the otherwise achiral Cu(110) surface. These self-assemblies were originally attributed to the close proximity of the  $\alpha$ -hydroxy groups on the neighbouring bitartrate [13, 14, 17], leading to *intermolecular* hydrogen-bond interactions.

In an earlier study, we have demonstrated by first-principles calculations that  $\alpha$ -hydroxy groups prefer to interact with oxygen atoms of the  $\text{COO}^-$  group of the bitartrate species, forming an *intramolecular* hydrogen bond [18]. The formation of these H-bonds stabilises the adsorbed species compared to its gas-phase configuration, in which it has several intramolecular H-bonds. This has been confirmed by studying the adsorption of a similar molecule: succinic acid ( $\text{HOOC-CH}_2\text{-CH}_2\text{-COOH}$ ) [18]. The adsorption of this molecule is less strong than for tartaric acid due to the lack of H-bond formation in its adsorbed form.

On the Ni(110) catalyst, a similar *intramolecular* hydrogen bond has been observed from theoretical calculations of bitartrate adsorption [19], however there is no long range ordering of the tartaric acid molecules [19]. This implies that there is no correlation between *intramolecular* hydrogen bonds and the long range ordering of bitartrate on the (110) surface. Contrary to Ni(110), several ordered structures were observed for tartrate adsorption on Ni(111) [20].

It was possible to demonstrate that lateral interactions are responsible for the formation of the different chiral domains by distinct optical isomers of tartaric acid on

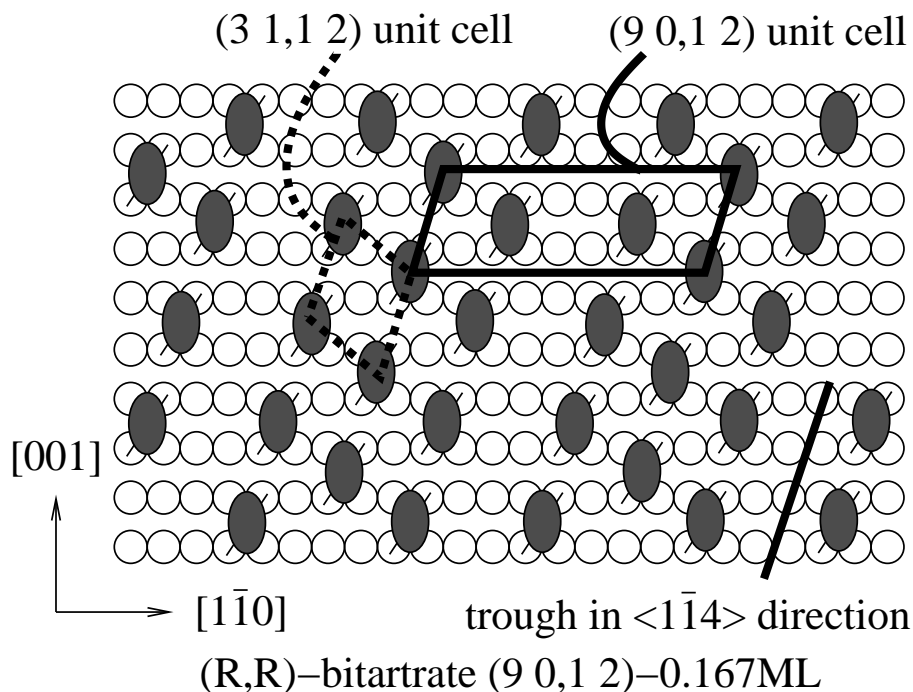


Figure 4.1: The (9 0, 1 2) structure for (*R,R*)-bitartrate on Cu(110). The overall (9 0, 1 2) unit cell is indicated with a solid line, the dashed unit cell indicates the local (3 1, 1 2) ordering within the rows. The trough in the  $\langle 1\bar{1}4 \rangle$  direction can provide chiral adsorption sites on the otherwise achiral Cu(110) surface.

the Cu(110) surface [18]. These interactions also play an important role upon increasing the coverage; the bitartrate form transforms to the monotartrate form, leading to a re-organisation of the molecular domain to a (4 0, 2 3) arrangement [13, 14, 17].

To attain more insights into the creation of the empty troughs and understand why such specific chiral domain, *viz.* (9 0, 1 2), is formed upon adsorption of (*R,R*)-tartaric acid on Cu(110), the present work combines two important and well-known theoretical tools: periodic Density Functional Theory and kinetic Monte Carlo simulations. From the results obtained for bitartrate we will finally discuss similar empty trough structures, formed through adsorption of acetate [21] and succinate [22] on Cu(110), for which the formation mechanism until now was unclear.

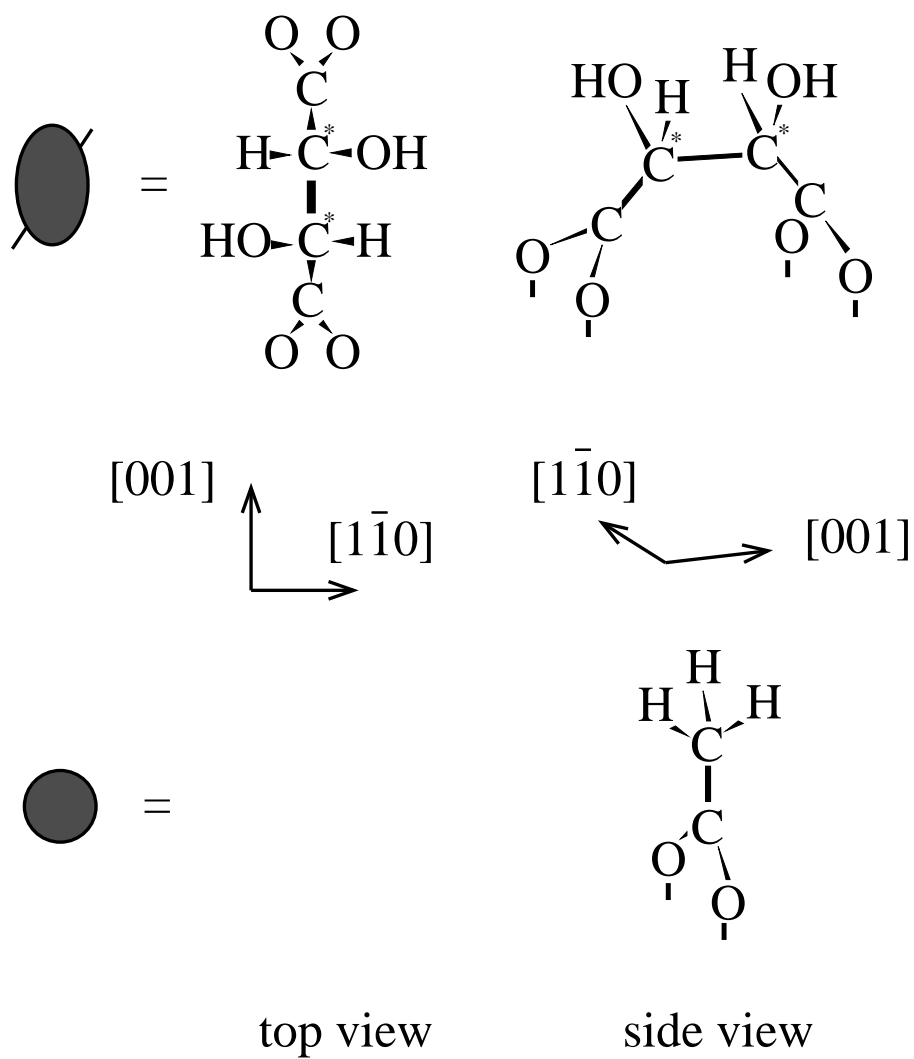


Figure 4.2: The adsorption geometry of  $(R,R)$ -bitartrate and acetate on Cu(110). The dashes protruding from the tartrate ovals represent the tartrate hydroxyl groups sticking out.

## 4.2 MODEL AND METHODS

### 4.2.1 THE REACTION MODEL

The model is formed by a rectangular (110) surface, with adsorbed (*R,R*)-bitartrate molecules. The (*R,R*)-bitartrate is assumed to be adsorbed with one carboxylate group attached to two copper atoms in one row, and the other carboxylate group attached to two copper atoms in the next row (see Figure 4.2) [13, 15].

Adsorption took place on an empty grid, during a simulated time of 100 s (100 times  $\tau_{\text{ads}} = 1/k_{\text{ads}}$ ). The grid size was a multiple of the (9 0,1 2) unit cell, i.e., 90x36, with each grid point representing a tartrate binding site between four surface copper atoms. The simulated temperature was equal to 365 K, well within the experimental region of 350–405 K where the bitartrate adlayer was equilibrated [15].

Adsorption of (*R,R*)-bitartrate required a rectangle of four empty copper sites; each copper atom binds one of the four carboxylate oxygen atoms of the bitartrate. The adsorption rate constant was set to unity ( $1 \text{ s}^{-1}$ ). The Brønsted-Evans-Polanyi coefficient  $\alpha$  for adsorption was zero, implying barrierless adsorption.

In the experiment, no new (*R,R*)-bitartrate can adsorb in the empty troughs of the (9 0,1 2) structure (though at higher pressures adsorption of monotartrate is possible) [13]. This gives, apart from the requirement that a rectangle of four protruding copper atoms is free, the additional condition that the neighbouring atoms in the  $[1\bar{1}0]$  direction also have to be empty to allow adsorption. This extra requirement that the neighbouring sites (at the 1\_hor position) need to be empty to allow adsorption of (*R,R*)-bitartrate is justified by the large repulsive value of the 1\_hor interaction, see Table 4.2.

The surface adlayer was equilibrated by allowing diffusion. Diffusion was allowed in the  $[1\bar{1}0]$  and in the  $[001]$  direction, so along the copper rows and perpendicular to the copper rows, where the diffusion rate was modified by the interactions. The hopping rate constant was set to 20,000 hops per second ( $k_{\text{diff}}/k_{\text{ads}} = 20,000$ ) in each direction, with tests performed with rate constants up to  $200,000 \text{ s}^{-1}$ . The Brønsted-Evans-Polanyi coefficient  $\alpha$  for diffusion was set to 0.5, implying a middle transition state.

We included interactions between neighbouring adsorbed (*R,R*)-bitartrate molecules. The first neighbour shell consists of eight different possibilities, which are displayed in Figure 4.3. Because of the presence of the OH groups, all of these interactions are in principle different.

Due to the extent of the interactions along the copper rows, some additional interactions were also included in our model. These additional interactions are the ones where a copper row is being shared by two carboxylate groups of different tartrate molecules (see Figure 4.4). These interactions are part of the second neighbour shell. The other second neighbour shell interactions are expected to be close to zero, since the first neighbour shell interactions closer by for those positions are already small.

It is well known that the fcc(110) surface has an anisotropic surface stress, i.e., the surface stress in the  $[1\bar{1}0]$  direction is different from the surface stress in the  $[001]$  di-

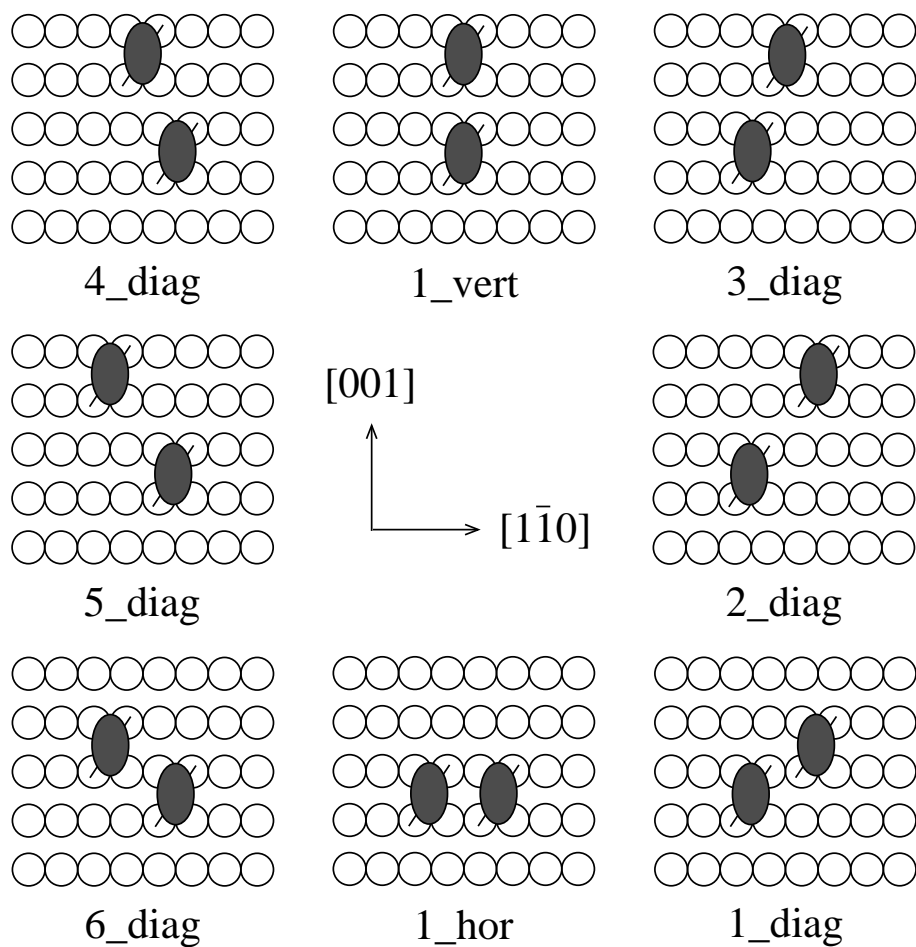


Figure 4.3: The first neighbour shell interactions  $\varphi(i)$  for  $(R,R)$ -bitartrate on Cu(110) in our model.

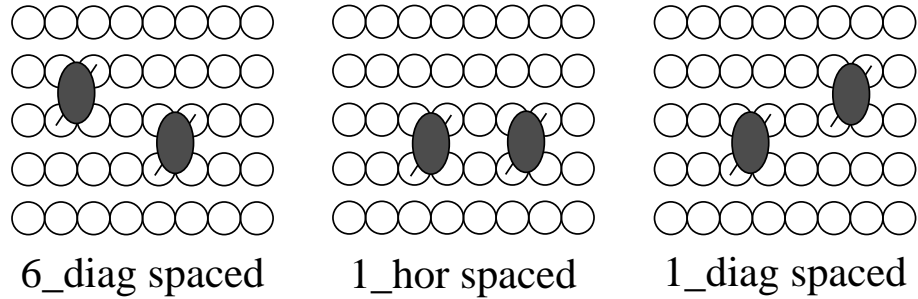


Figure 4.4: The second neighbour shell interactions  $\varphi(i)$  for  $(R,R)$ -bitartrate on Cu(110) in our model.

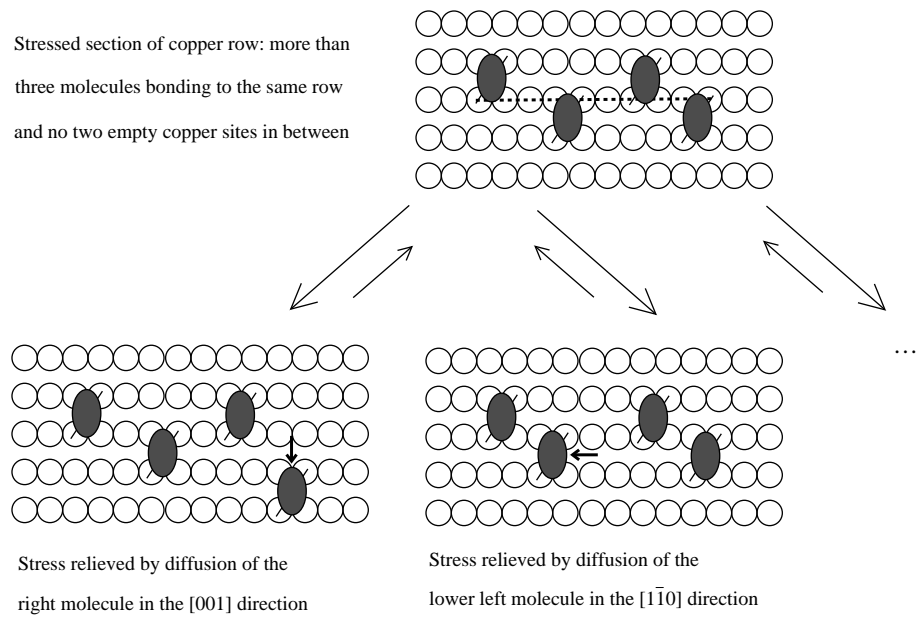


Figure 4.5: The additional through-surface interaction for  $(R,R)$ -bitartrate on Cu(110) in our model. If more than three  $(R,R)$ -bitartrate molecules bind next to each other to the same section of copper row (i.e., in the  $[1\bar{1}0]$  direction) with one or no empty copper atoms in between, the adsorption energy is lowered (top). This causes an increase in the diffusion rate for jumps releasing this surface stress, like the lower two examples show for a jump in the [001] (bottom left) and a jump in the  $[1\bar{1}0]$  (bottom centre) direction. The two jumps shown are examples; six other jumps also release the adsorbate-induced surface stress in this case.

rection [23, 24]. The surface stress in the  $[1\bar{1}0]$  direction increases upon adsorption of different molecules. In some cases, the stress is released by reconstruction of the (110) surface, for example the Cu(110) surface shows an added/missing row reconstruction upon adsorption of oxygen [25].

Previously, we have observed that the Cu-Cu surface bond increases from 2.58 to 2.62 Å in the  $[1\bar{1}0]$  direction upon adsorption of bitartrate [18], thus causing an increase in the surface stress along the copper rows in the  $[1\bar{1}0]$  direction. We therefore proposed that the empty trough of the (9 0,1 2) pattern forms to reduce the surface stress along the copper rows (i.e., the  $[1\bar{1}0]$  direction), similar to the added/missing row reconstruction of the Cu(110) surface upon oxygen adsorption [18]. So, summarising, the proposal of an adsorbate-induced surface stress in the  $[1\bar{1}0]$  direction is motivated by (1) an increase in the Cu-Cu spacing (in the  $[1\bar{1}0]$  direction) due to bitartrate adsorption, (2) the observation of (2x1) reconstructions for many fcc(110) surfaces which are related to surface stresses and (3) the fact that the nearest neighbour copper atom in the [001] direction is farther away than for the  $[1\bar{1}0]$  direction. The induction of a surface stress in the [001] direction is in principle possible for bitartrate because the bitartrate backbone is deformed to bond to two neighbouring copper rows. No such surface stress in the [001] direction is possible for the similar ordered structure of acetate on Cu(110); this molecule binds to only one copper row (see Section 4.5.2). The fourth argument in favour of an adsorbate-induced surface stress in the  $[1\bar{1}0]$  direction is therefore provided by the existence of a similar ordered structure for a molecule which cannot induce a stress in the [001] direction.

This adsorbate-induced surface stress can be seen as an elastic interaction [26]: the adsorbates induce a change in the substrate geometry, and this influences the bonding of adsorbates farther away. Elastic interactions are known to be long-range in nature. In our case the adsorbed tartrate molecules stretch the copper-copper distance in the  $[1\bar{1}0]$  direction, thus resulting in an elastic interaction (or stress) in this direction. The interaction (a special form of  $\varphi$ ) is modelled in the following way (Figure 4.5): copper atoms along a copper row are postulated to experience a surface stress due to adsorption of (*R,R*)-bitartrate on copper atoms nearby in the same row. This stress builds up when more than three (*R,R*)-bitartrate molecules bind next to each other to the same section of the copper row and is removed if two or more copper atoms are left empty between the (*R,R*)-bitartrate molecules.

In other words, starting from a section of copper row with two (or more) empty copper sites, one counts the number of tartrate molecules binding to it until again two (or more) empty copper sites are encountered. If the number of tartrate molecules counted is more than three, than that section of copper row is stressed. If no two empty copper sites are found at all for a copper row, the entire row is stressed. The binding energy of bitartrate to a stressed section of a copper row is less than the binding energy to a non-stressed section of a copper row. This causes an increased rate for jumps that remove the lining-up of stressed adsorbates; and a decrease in the number of jumps that form this kind of stressed line-ups.

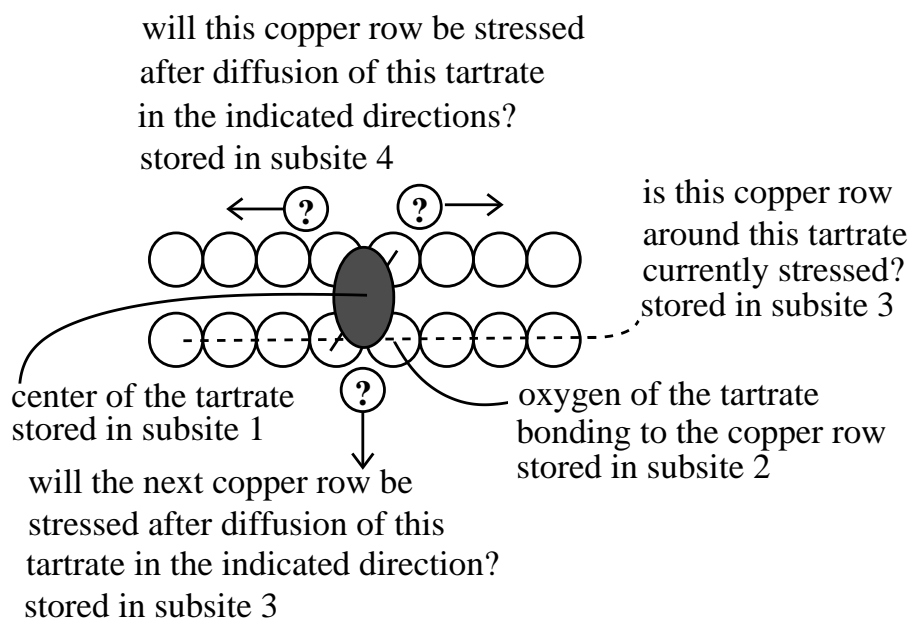


Figure 4.6: The usage of subsites for information storage in our model.

#### 4.2.2 IMPLEMENTATION OF THE ADSORBATE-INDUCED SURFACE STRESS

The question whether a bitartrate binds to one or more stressed copper rows can only be answered by looking at the occupancy of several neighbouring sites. The standard implementation of lateral interactions in the program we use checks each neighbouring site, and modifies the activation energy by a certain amount if a site is occupied. Three-particle interactions and interactions like the stress used here require some additional bookkeeping. Below we will indicate for the interested reader how the stress was implemented.

The model uses of a grid with four different subsites to do the bookkeeping associated with the implementation of the stress. The first subsite stores the centre of the bitartrate molecule in between the copper rows (Figure 4.6). A second subsite is located on top of each copper atom of the copper rows. This site can either be empty, or bonded to by a carboxylate oxygen of the bitartrate. An adsorbed bitartrate is therefore defined by its centre (stored in the first subsite) and the the four copper atoms it is binding to (stored in the second subsite).

If we want to look whether a stretch of copper row is stressed, and we only store the centres of the bitartrates, than we need to look both above and below the copper row, as well as along it. With the occupation of the copper atoms known, we only need to search along one direction, along the copper row. By using this additional



subsite which describes the occupancy of the copper atoms we can therefore more easily answer the question whether a copper row is stressed: the problem is now one-dimensional instead of two-dimensional.

The other subsites number three and four are then used to store whether the bitartrate is currently bonding to stressed copper rows, and to store whether the bitartrate will be bonding to stressed copper rows if it hops up, down, left or right. By storing this in a subsite, we can use the standard implementation of the program, check only at one subsite whether the bitartrate binds to a stressed row, and based on the information in that single subsite modify the activation energy. The information in these subsites needs to be updated after diffusion. This is done by a set of immediate reactions. The simulation procedure then becomes:

1. Adsorb or move an (*R,R*)-bitartrate molecule; the new positions of the centre of mass (subsite 1) and the four oxygens binding to the copper rows (subsite 2) are stored.
2. Check along the copper rows (i.e., subsite 2) the tartrate binds to, whether the carboxylate groups of the (*R,R*)-bitartrate are currently bound to stressed or non-stressed copper rows; store the answer for both copper rows each (*R,R*)-bitartrate binds to in the third type of subsite.
3. Check along the copper rows (i.e., subsite 2) the tartrate binds to, whether diffusion to the left or to the right (along the copper rows) of the bitartrate will cause one or both of the carboxylate groups to bind to a stressed copper row; store the answer for each carboxylate group and each direction (left or right) in subsite 4.
4. Check along the neighbouring copper rows (up or down, in the [001] direction), whether a jump up or down of the bitartrate will cause a carboxylate group to bind to a stressed copper row; store the answer for each jump direction (up or down) in subsite 3.
5. Move an (*R,R*)-bitartrate molecule, using the labels in subsite 3 and 4 to modify the reaction rate constant for the stress if present; the neighbouring subsites 1 (storing the bitartrate centres of mass) are checked to modify the reaction rate constant for the ‘normal’ nearest- and next-nearest-neighbour interactions.

### 4.2.3 DFT METHODOLOGY

In the work reported here all electronic structure calculations were performed using the Vienna Ab-initio Simulation Package (VASP) [27, 28]. This code allows for periodic Density Functional Calculations (DFT) using pseudopotentials and a plane wave basis set. The DFT was parameterised in the local-density approximation (LDA), with the exchange-correlation functional proposed by Perdew and Zunger [29] and corrected for nonlocality in the generalised gradient approximations (GGA) using the

Perdew-Wang 91 functional [30]. The interaction between the core and valence electrons is described using the ultrasoft pseudopotentials introduced by Vanderbilt [31] and provided by Kresse and Hafner [32].

In the calculations performed here the Cu(110) surface is modelled by a periodic five-layer slab with a bitartrate adlayer adsorbed on one side of the slab. One slab is separated from its periodic image in the  $z$  direction by a vacuum space which is equivalent to eight metal layers. Only the two bottom layers have been kept frozen at bulk distance in all optimisations.

To minimise the effect of the stress that occurs due to the constraints in the slab model, the optimal bulk Cu-Cu distance was calculated to be 2.58 Å [18], which is in good agreement with the experimental value of 2.56 Å [33].

The aim of the electronic structure calculations is to gather information on the lateral interactions between the bitartrate species on the Cu(110) surface. Beyond 1/6 ML bitartrate species undergo a chemical transformation to monotartrate species [15], therefore, all systems studied here have a coverage equal to or below 1/6 ML. Several different relative positions of two neighbouring bitartrate species have been investigated here as listed in Table 4.1 and Figure 4.7. To achieve low coverage limit on the surface, the unit cells were rather large: 18 atoms per metal layer for the  $6 \times 3$  arrangement and 24 atoms per metal layer for the  $6 \times 4$  arrangement. In addition, the experimental (9 0, 1 2) unit cell, which has 18 atoms per metal layer and three bitartrate molecules (1/6 ML), has been studied.

The Brillouin-zone integrations have been performed on a  $1 \times 2 \times 1$  Monkhorst-Pack grid of  $k$ -points, allowing to reach the desired convergence for the system energy.

The hydrogen atoms, which were released during the formation of the bitartrate phase, were considered to recombine and desorb as molecular hydrogen, which is well-known experimentally for Cu-surfaces at room temperature [34, 35].

### 4.3 DETERMINATION OF THE IMPORTANT INTERACTIONS

The model has 8 first neighbour shell interactions (see Figure 4.3). Each of these interactions can be thought of as having a direct and a through-surface part. The symmetry breaking in the (*R,R*)-bitartrate case is caused by a direct hydroxyl-hydroxyl interaction, separated by less than 2 Å [18]. This close proximity is only realised when the adsorbates are arranged according to the 1\_diag position in Figure 4.3. All other arrangements result in a larger distance between the hydroxyl groups. Since the direct repulsive interaction between two hydroxyl groups decreases with distance, it can be argued that the hydroxyl groups do not contribute to other interactions besides 1\_diag.

All other interactions are due to carboxylate groups bonding to neighbouring copper atoms, and they are therefore surface-mediated and more long-range. As a consequence of this, it can be argued that 2\_diag and 5\_diag (short: 2,5\_diag) are similar, and 3\_diag and 4\_diag (3,4\_diag) as well. Interestingly, the through-surface part of 1\_diag should be similar to the through-surface part of 6\_diag, even though the total value of the first neighbour shell interaction for each position should be distinct. We

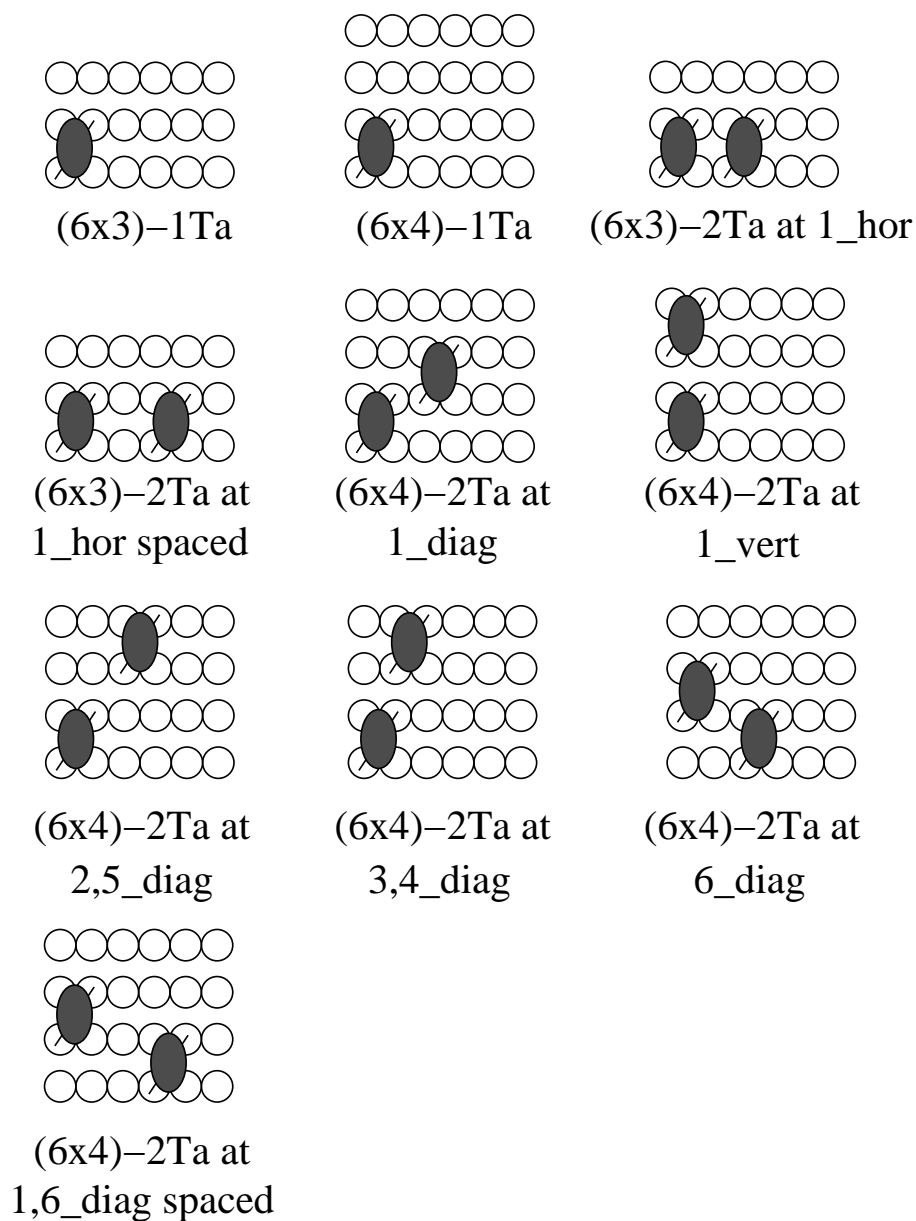


Figure 4.7: Ordered structures for  $(R,R)$ -bitartrate on Cu(110) calculated by DFT.

Table 4.1: Adsorption energies per adsorbate molecule for ordered structures of (*R,R*)-bitartrate on Cu(110) calculated by DFT.

designation	coverage (ML)	$E_{\text{ads}}$ (kJ/mol)
(6 × 3)-1Ta	0.056	-158
(6 × 4)-1Ta	0.042	-158
(6 × 3)-2Ta at 1_hor	0.111	-145
(6 × 3)-2Ta at 1_hor spaced	0.111	-147
(6 × 4)-2Ta at 1_diag	0.083	-147
(6 × 4)-2Ta at 1_vert	0.083	-153
(6 × 4)-2Ta at 2,5_diag	0.083	-153
(6 × 4)-2Ta at 3,4_diag	0.083	-153
(6 × 4)-2Ta at 6_diag	0.083	-150
(6 × 4)-2Ta at 1,6_diag spaced	0.083	-151
(9 0,1 2)	0.167	-128
(3 1,1 2)	0.200	-113 <sup>a</sup>
(-3 1,-1 2)	0.200	-103 <sup>a</sup>

<sup>a</sup> Adapted from Ref. 18.

can thus effectively reduce the number of first neighbour shell interactions from 8 to 6: 1\_hor, 1\_diag, 2\_diag (=5\_diag), 3\_diag (=4\_diag), 1\_vert and 6\_diag.

All the interactions mentioned above may play a role in the formation of the (9 0,1 2) structure, so we have applied DFT calculations to determine their values (Figure 4.7 and Table 4.1). The similarity in the adsorption energy for the (6 × 3)-1Ta and the (6 × 4)-1Ta structure shows that there is no further interaction in the [001] direction. The (6 × 3)-1Ta structure can therefore be taken as a reliable estimate of the zero-coverage limit. By coadsorbing other (*R,R*)-bitartrate molecules, we were able to extract the pairwise interactions  $\varphi(i)$ , listed in Table 4.2:

$$\varphi(i) = (E_{\text{ads,coadsorbed}} - E_{\text{ads,alone}})/n \quad (4.1)$$

where  $n$  is the number of pairwise interactions per adsorbate in the coadsorbed structure. As an example, the value for 1\_vert was deduced by taking the difference between the '(6 × 4)-2Ta at 1\_vert' and the '(6 × 4)-1Ta' adsorption energy:  $5 = -153 + 158$  kJ/mol, with  $n$  equal to one. From Figure 4.7 one can see that in the '(6 × 4)-2Ta at 1\_vert' unit cell there are two tartrate molecules, and two 1\_vert interactions (one in the middle of the unit cell, one across the unit cell boundary in the [001] direction; this interaction spans from the top of the unit cell into the bottom of the next unit cell).  $n$  therefore equals two interactions per unit cell divided by two tartrate molecules per unit cell, so one interaction per adsorbate.

As a second example, 1\_hor was determined by taking the difference between the '(6 × 3)-2Ta at 1\_hor' and the '(6 × 3)-1Ta' adsorption energy and dividing by one half:  $26 = [(-145 + 158)/0.5]$  kJ/mol, with  $n$  equal to one half. From Figure 4.7 one

can see that in the  $(6 \times 3)$ -2Ta at 1<sub>hor</sub> unit cell there are two tartrate molecules, and only one 1<sub>hor</sub> interaction (in the middle of the unit cell, and none across the unit cell boundaries).  $n$  therefore equals one interaction per unit cell divided by two tartrate molecules per unit cell, so one half interaction per adsorbate.

As shown in Table 4.2, 1<sub>hor</sub>, 1<sub>diag</sub> and 6<sub>diag</sub> turn out to be considerable, with all other first neighbour shell interactions being much smaller. The large value of the three mentioned interactions is due to carboxylate groups bonding to neighbouring Cu atoms. In the case of 1<sub>hor</sub>, there are two times two carboxylate groups bonding next to each other to the same copper row. This results in a strongly repulsive interaction of 26 kJ/mol. For 6<sub>diag</sub>, there is only one couple of two carboxylate groups binding next to each other to the same copper row, and the value of this interaction is therefore roughly half the value for 1<sub>hor</sub>. The 1<sub>diag</sub> interaction is larger than the 6<sub>diag</sub> interaction due to the additional hydroxyl-hydroxyl repulsion. A rough value for the additional hydroxyl-hydroxyl interaction can be derived from the difference in energy between the (3 1,1 2) structure and the (-3 1,-1 2) structure, about 10 kJ/mol [18]. If one adds the hydroxyl-hydroxyl repulsion to the 6<sub>diag</sub> through-surface interaction, the total 1<sub>diag</sub> interaction would be about 26 kJ/mol, which is quite close to calculated value of 22 kJ/mol. The interactions 1<sub>vert</sub>, 2<sub>diag</sub>, 5<sub>diag</sub>, 3<sub>diag</sub> and 4<sub>diag</sub> do not involve tartrate molecules bonding to the same copper rows, they bind to neighbouring copper rows. This results in a much smaller interaction of 5 kJ/mol repulsive.

It is striking to see that one of the interactions present in the (9 0,1 2) structure, the 6<sub>diag</sub> interaction, is actually strongly repulsive. This immediately leads to the conclusion that the (9 0,1 2) structure is only formed at coverages close to 0.167 ML, in avoidance of other, even stronger interactions (1<sub>hor</sub>, for instance). Because of the strong interactions along the copper rows (1<sub>diag</sub>, 6<sub>diag</sub> and 1<sub>hor</sub>), we have also looked at the second neighbour shell along the copper rows.

The calculations of the second neighbour shell structures ( $(6 \times 3)$ -2Ta at 1<sub>hor</sub> spaced' and  $(6 \times 4)$ -2Ta at 1,6<sub>diag</sub> spaced') also show a decrease in binding energy with respect to the zero-coverage limit. The decrease in binding energy is here due to both surface stress (which will be defined in the next section) and the second neighbour shell interaction. Nevertheless the results clearly show that these interactions are less repulsive than 1<sub>hor</sub> and 6<sub>diag</sub> respectively. 1<sub>diag</sub> spaced and 6<sub>diag</sub> spaced are taken to be equal since at this larger distance the hydroxyl-hydroxyl repulsion observed for 1<sub>diag</sub> is likely to be negligible.

The surface stress was determined from the difference in binding energy between tartrate adsorbed in the (3 1,1 2) and (9 0,1 2) arrangement; both structures have similar interactions, but one is stressed, the other one not. In the (3 1,1 2) structure, the first neighbour shell interactions experienced by each tartrate are:

$$3_{\text{diag}} + 6_{\text{diag}} + 2 \times \text{Stress}. \quad (4.2)$$

The stress is included twice, since both carboxylate groups of the tartrate bind to a stressed copper row. For the (9 0,1 2) structure, the interactions are (averaged over the

Table 4.2: Values for the lateral interactions (kJ/mol) derived from the adsorption energies listed in Table 4.1 and for the kMC model.

interaction	DFT	kMC model
first neighbour shell:		
1_hor	26	26
1_diag	22	22
1_vert	5	5
2_diag, 5_diag	5	5
3_diag, 4_diag	5	1
6_diag	16	10
second neighbour shell:		
1_hor spaced	11	11
1_diag spaced, 6_diag spaced	7	7
Stress	5	6

2 different tartrate molecules in the unit cell):

$$3\_diag + \frac{2}{3} \times 6\_diag. \quad (4.3)$$

From the difference in adsorption energy of tartrate in the (3 1,1 2) and (9 0,1 2) structure, having previously derived the value for 6\_diag, we can therefore derive the value of the stress. The value of the stress then amounts to 5 kJ/mol per stressed row (with each tartrate binding to two copper rows, this can add up to 10 kJ/mol per adsorbate).

The additional stability of the (9 0,1 2) structure with respect to the (3 1,1 2) structure amounts to 10 kJ/mol, if corrected for the absence of the 6\_diag interaction in the (9 0,1 2) structure. This clearly indicates the effect of the empty troughs in the (9 0,1 2) structure: by locally leaving sites empty, the bonding of tartrate molecules nearby is stronger.

#### 4.4 ORDERING OF THE ADLAYER

As mentioned before the DFT-based parameter set includes some very repulsive interactions. In computational terms this means that a great amount of diffusion is needed, such that rare events (rare because they are energetically unfavourable) are also well represented during our simulations. This led us to use large diffusion rates and relatively small grids (as seen in the Section 4.2.1). Still, with these diffusion rates and

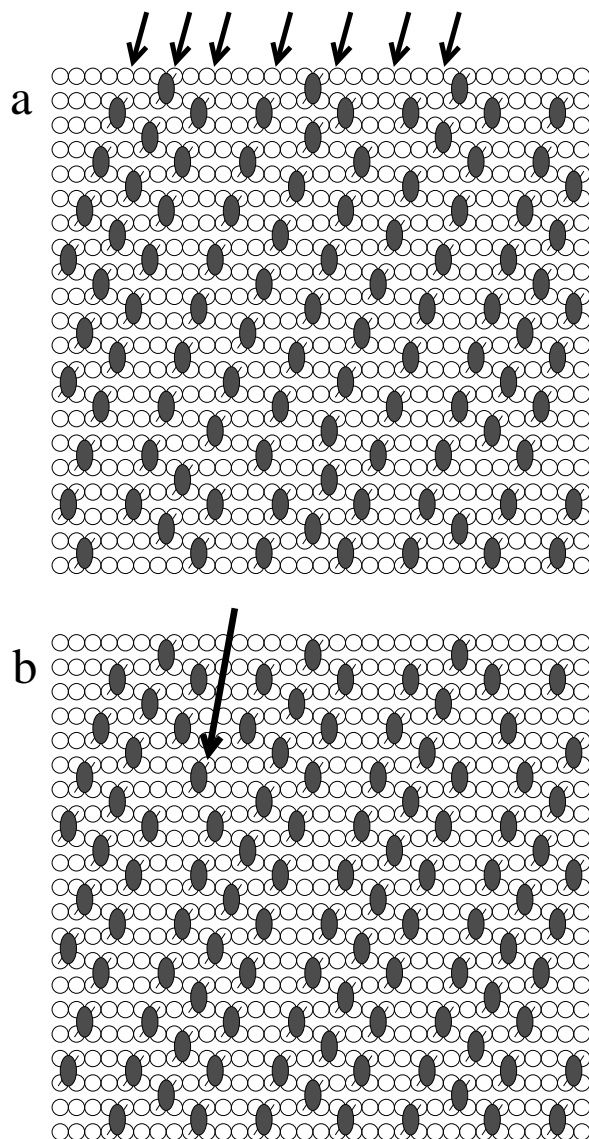


Figure 4.8: Snapshots of simulated adsorption of  $(R,R)$ -bitartrate on Cu(110). (a) the  $(3 \ 1,1 \ 2)$  rows of the  $(9 \ 0,1 \ 2)$  structure (upper left of the picture) form through compression of the wider spaced rows in a  $(4 \ 1,1 \ 2)$  structure (middle of the picture). The difference in row spacing is indicated by the arrows above the picture. Common defects in the  $(9 \ 0,1 \ 2)$  structure are indicated by the arrows in (b) and (c). (b) missing tartrate defect between the  $(3 \ 1,1 \ 2)$  rows.

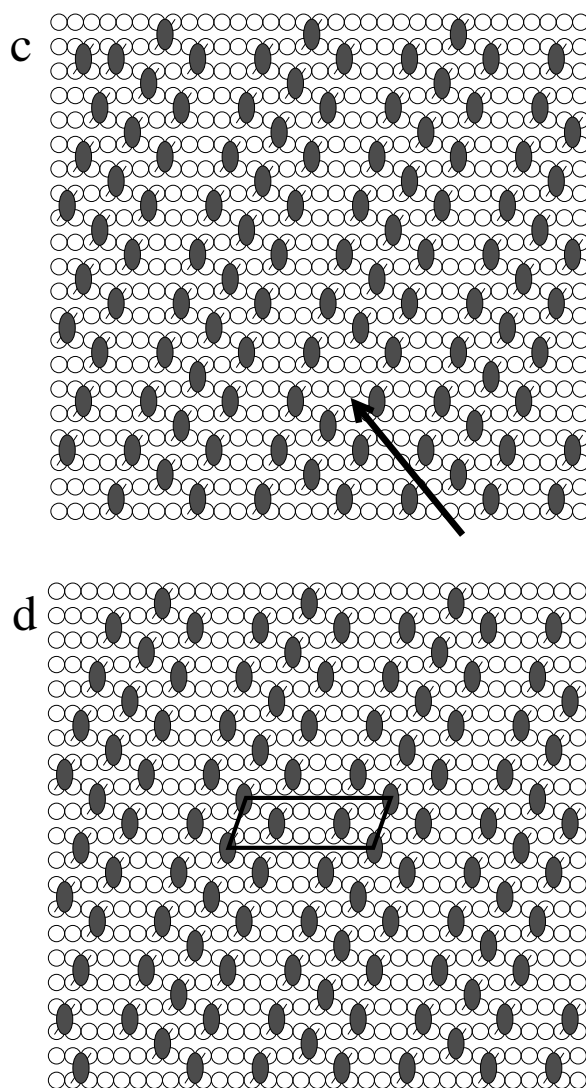


Figure 4.8: (continued) (c) missing tartrate within the (3 1,1 2) rows. (d) under continued adsorption, a perfect (9 0,1 2) structure is obtained; the unit cell is indicated. Snapshots of 30x20 sites, taken from a full simulated grid of 90x36 sites.



grid sizes we needed to reduce the value of some interactions to improve the simulation time, but keeping the overall order of the DFT parameter set, see the column ‘kMC model’ in Table 2.

The rationale for reducing 3\_diag, 4\_diag and 6\_diag with respect to the DFT-value is that since they are repulsive, diffusion to these positions is a rare event. Of course a given amount of these diffusion steps is necessary for the formation of the (9 0,1 2) structure; this means that the less probable these diffusion events are (i.e., the more repulsive the interactions are), the larger the total number of diffusion trials must be. These diffusion trials determine the overall computational cost. With the diffusion rate constant of  $20,000 \text{ s}^{-1}$ , the 3\_diag, 4\_diag and 6\_diag interaction can not be chosen more repulsive, since otherwise the attempt frequencies become too low, and the adlayer does not order within the simulated time. Adsorption at higher temperatures and thermal annealing of the adlayer have been considered to make the rare events more likely, but this results in a collapse of the (9 0,1 2) structure into a (3 1,1 2) structure because of the small value of the stress. Choosing a much smaller simulation grid than the one we used reduces the computational cost, but it will contain only a couple of (9 0,1 2) unit cells. This is undesirable, since for small grid sizes diffusion is severely hampered by interaction with the periodic boundary images of the bitartrates present, mitigating the advantage of reduced computational cost.

In conclusion, the reduction of 3\_diag, 4\_diag and 6\_diag is needed to limit the cpu time used. If we then compare the parameters used with the DFT-based parameters, we still have a very good match: for most of the interactions we were able to use the DFT-based values, and the overall order of repulsiveness of the first neighbour shell interactions is maintained. For both parameter sets the overall order is  $1_{\text{hor}} > 1_{\text{diag}} > 6_{\text{diag}} >$  all other first neighbour shell interactions. Both parameter sets yield the same energetical order of the possible ordered structures. This modified parameter set is therefore in good agreement with the DFT calculations and suitable to simulate the ordering behaviour of tartrate.

The first interesting result appears when the second neighbour shell interactions are not used, the (9 0,1 2) structure does not form in our simulations. Instead the adsorbates collapse into a (stressed) (3x2)-0.167 ML structure, even when the influence of the surface stress is added to this simulation. In addition, the (9 0,1 2) arrangement is also not formed if the second neighbour shell interactions are added but not the stress. This suggests that both the second neighbour shell interactions and the surface stress are important for the formation of the (9 0,1 2) configuration.

The formation of the (9 0,1 2) structure is displayed in Figure 4.8. Since all interactions are repulsive, the (9 0,1 2) structure only forms at coverages close to 0.167 ML. It forms as a consequence of the avoidance of strongly repulsive interactions (like  $1_{\text{hor}}$ ,  $1_{\text{diag}}$  and the stress). At around 0.15 ML, the tartrate orders in rows in the  $\langle 1\bar{1}4 \rangle$  direction, forming a (4 1,1 2) structure (centre of panel a). The (4 1,1 2) structure is similar to the (3 1,1 2) rows in the (9 0,1 2) structure, except for the larger spacing in the  $[1\bar{1}0]$  direction (indicated by the arrows above the panel). Upon increasing the coverage, the rows of the (4 1,1 2) structure collapse to form the (3 1,1 2) rows of the (9 0,1 2) structure (left and right of panel a). Common defects during formation

of the (9 0,1 2) structure are displayed in panels b and c. If one of the tartrates at the edge of one of the (3 1,1 2) rows is missing, the one opposite to it can jump out of its (3 1,1 2) row and sit in the middle of the trough. This reduces the number of interactions experienced by this tartrate molecule, without the copper rows getting stressed (panel b). Sometimes also a tartrate in the middle of the (3 1,1 2) rows is missing, but in our model this does not cause other tartrate molecules to move, as shown in panel c. This is due to the hard-rectangular shape of the bitartrate in our model. None of the bitartrates in Figure 4.8c can hop to the empty site without other bitartrates having to move aside. Finally, when also these defects are filled, a perfect (9 0,1 2) structure is formed, as shown in panel d.

## 4.5 DISCUSSION

### 4.5.1 RECONSTRUCTION OF THE SURFACE

We have done our DFT calculations under the assumption that the bitartrate binds to a non-reconstructed Cu(110) surface; i.e., all the slabs in our calculations have a clean (110) termination. The interactions derived from these calculations reproduce the (9 0,1 2) structure. A reconstructed surface with bitartrate binding to it would have given a different set of interactions, which would not necessarily cause the formation of a (9 0,1 2) structure. In hindsight we can therefore conclude that the assumption that the Cu(110) surface is not reconstructed is justified. This conclusion may be extended to the low-coverage ordered structures for succinate and acetate on Cu(110). Reconstruction of the surface is known for higher coverages of acetate on Cu(110) [36], though, and also for formic and (p-amino-)benzoic acid [37, 38]. Mobile copper atoms are known to be included in ordered structures of for example benzoic acid on Cu(110) [39]. As shown here, no such mobile copper atoms are needed to explain the stability of the (9 0,1 2) structure. This does not, however, totally exclude the possibility that additional copper atoms are present.

For (*R,R*)-bitartrate on Ni, the surface is also reconstructed [19, 20]. Lateral interactions different from the ones on copper (110) system are therefore present, and no (9 0,1 2) ordered structure is formed.

In addition, calculations of the surface stress along and perpendicular to the metal rows (i.e., in the  $[1\bar{1}0]$  and  $[001]$  direction) for different metals have shown that there is a correlation between these stresses and the (non-)occurrence of the (1x2) missing row reconstruction [23, 24]. This difference in stress may also explain why bitartrate on Cu does not cause reconstruction of the surface, while on Ni it does.

### 4.5.2 SIMILAR PATTERNS FORMED BY OTHER ADSORBATES

We have also looked at other adsorbates, and it turns out that the adsorption of (*R,R*)-bitartrate on Cu(110) shows many similarities to other acids adsorbed on this surface.

In the case of acetate, the bonding is between two copper atoms and the carboxylate group (as seen by IR spectroscopy [21, 36] and theoretical calculations [40, 41])

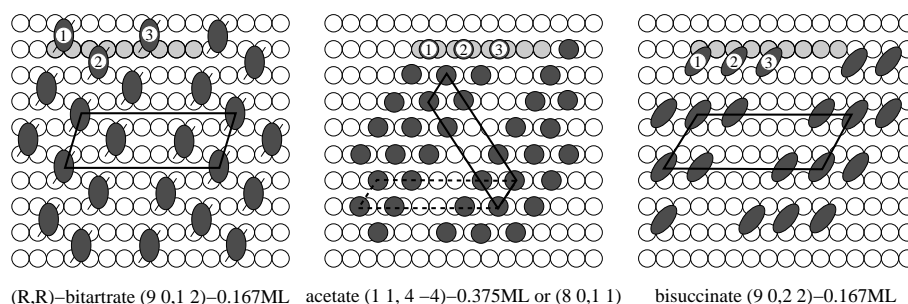


Figure 4.9: Comparison of the  $(R,R)$ -bitartrate (9 0,1 2) ordered structure (left panel) with the acetate (1 1,4 -4) ordered structure (middle panel) and one of the proposed arrangements for the bisuccinate (9 0,2 2) ordered structure [22] (right panel). Due to the similar bonding through the carboxylate groups  $(R,R)$ -bitartrate and acetate form rows of each three molecules, separated by empty troughs of each two unoccupied copper atoms (see shaded atoms). The bisuccinate also forms rows of each three molecules, but the empty trough is three instead of two copper atoms wide. An alternative unit cell to the acetate (1 1,4 -4) structure is indicated by the dashed line, its designation is (8 0,1 1).

with the hydrocarbon backbone more or less perpendicular to the surface (i.e., sticking outwards, Figure 4.2). The only difference in the bitartrate case is the possibility of binding the second carboxylate group to a neighbouring bridging copper-copper site.

The (9 0,1 2)  $(R,R)$ -bitartrate structure has an acetate equivalent: the (1 1,4 -4)-0.375 ML acetate structure (Figure 4.9, left and middle panel) [21, 36, 42, 43]. Two unit cells are indicated, first the common (1 1,4 -4) with a solid line, and added to that one more resembling the geometry of the (9 0,1 2) unit cell of the  $(R,R)$ -bitartrate structure, with a dashed line and the designation (8 0,1 1).

There are a number of striking similarities between these structures. First, in both structures the stacking of molecules in the [001] direction is avoided. This is easily explained by the steric hindrance of the methyl groups of neighbour acetate species at the 1<sub>vert</sub> position. This avoidance of the neighbouring sites in the [001] direction is also seen for the higher coverage ordered structure of acetate on Cu(110), the  $c(2 \times 2)$ -0.50 ML structure [21].

Second, both ordered structures have a binding of three carboxylate groups in the  $[1\bar{1}0]$  direction (shaded copper atoms in Figure 4.9), then an empty trough of two unoccupied copper atoms, and again binding of three carboxylate groups. In the acetate structure these groups are all adsorbed next to each other, while in the  $(R,R)$ -bitartrate case, two of them are adsorbed next to each other, while the third one is displaced in the  $[1\bar{1}0]$  direction.

Both are “empty trough” structures, and due to their binding similarities, the cause of the empty trough formation is likely to be similar. In principle, for the  $(R,R)$ -

bitartrate structure a stress could appear in the [001] direction because of the deformation of the bitartrate backbone. The acetate, on the other hand, has no second contact in the [001] direction; no direct stress can, therefore, build up in this direction. The stress causing the empty trough formation must therefore lie in the  $[1\bar{1}0]$  direction, along the copper atom rows in the acetate case, as was also suggested for the bitartrate case.

Third, considering the amount of carboxylate groups bound to the surface, they are almost identical:  $1/3$  ML for the (*R,R*)-bitartrate versus  $3/8$  ML for the acetate structure.

In a recent experimental study of the adsorption of succinic acid on Cu(110) an empty trough structure was also found, again with three bisuccinate molecules binding to one copper row, then a trough of three empty copper atoms, and again bisuccinate molecules [22]. Its unit cell is (9 0,2 -2), slightly different from the (*R,R*)-bitartrate unit cell (Figure 4.9, right panel). This is probably due to the absence of the internal H-bonds between the OH and the carboxylate groups in the bisuccinate case but present in the bitartrate [18], which leads to a different local bonding geometry (succinic acid is a bi-acid like tartaric acid, but with the hydroxyl groups replaced by hydrogen).

The similarity in the ordered structures of these three molecules (bitartrate, bisuccinate and acetate) suggests a common way of binding to the surface in order to release the surface stress, as demonstrated here for the bitartrate case. For bitartrate only the (9 0,1 2) domain is experimentally observed, since the repulsive hydroxyl-hydroxyl interaction prevents the formation of the (9 0,-1 2) structure. For acetate and succinate however, apart from the structures depicted in Figure 4.9, also domains of the mirror structures (-1 1,4 4) and (9 0,-2 2) are observed since they are energetically identical.

## 4.6 CONCLUSIONS

We have analysed the (9 0,1 2) (*R,R*)-bitartrate structure on the unreconstructed Cu(110) surface in terms of pairwise first and second neighbour shell interactions and an adsorbate-induced surface stress along the copper rows. We suggest that the surface stress is caused when more than three bitartrate molecules bind next to each other to the same section of copper row.

We have quantified these interactions and the stress using DFT calculations. As for the stress, a decrease in binding energy of about 5 kJ/mol is caused by adsorbing more than three carboxylate groups next to each other to the same section of copper row. This stress causes the empty troughs in the (9 0,1 2) structure. The interactions causing the (3 1,1 2) arrangement within the (9 0,1 2) structure are the direct (chiral) hydroxyl-hydroxyl repulsion, and the repulsion between carboxylate groups adsorbed right next to each other to the same copper rows. Aside from the first neighbour shell interactions along the copper rows, the second neighbour shell interactions along the copper rows are shown to be important for the formation of the (9 0,1 2) pattern: without them the bitartrate orders into an achiral (3x2) pattern.

Using a kinetic Monte Carlo model that incorporates the pairwise interactions and

the surface stress, we were able to explain the formation of the  $(9\ 0, 1\ 2)$   $(R,R)$ -bitartrate structure during the simulated adsorption of  $(R,R)$ -bitartrate on Cu(110).

Due to the similarity of bonding of acids to Cu(110), we expect an adsorbate-induced surface stress similar to the one observed for bitartrate will also cause the empty troughs in the ordered structures observed for acetate and succinate on Cu(110).

This chapter has been published as: C. G. M. Hermse, A. P. van Bavel, A. P. J. Jansen, L. A. M. M. Barbosa, P. Sautet and R. A. van Santen; Formation of chiral domains for tartaric acid on Cu(110): a combined DFT and kinetic Monte Carlo study; *J. Phys. Chem. B*, 108 (30): 11035–11043, 2004.

- [1] S. Akabori, S. Sakurai, Y. Izumi and Y. Fujii; An asymmetric catalyst; *Nature*, 178: 323–324, 1956.
- [2] Y. Orito, S. Imai and S. Niwa; Asymmetric hydrogenation of methyl pyruvate using Pt-C catalyst modified with cinchonidine; *J. Chem. Soc. Jpn.*, 8: 1118–1120, 1979.
- [3] O. Schwalm, B. Minder, J. Weber and A. Baiker; Enantioselective hydrogenation of  $\alpha$ -ketoesters over Pt/alumina modified with cinchonidine - theoretical investigation of the substrate-modifier interaction; *Catal. Lett.*, 23(3-4): 271–279, 1994.
- [4] U. K. Singh, R. N. Landau, Y. Sun, C. LeBlond, D. G. Blackmond, S. K. Tanielyan and R. L. Augustine; Enantioselective catalysis: influence of conversion and bulk diffusion limitations on selectivity in the hydrogenation of ethyl pyruvate; *J. Catal.*, 154(1): 91–97, 1995.
- [5] M. Studer, S. Burkhardt and H.-U. Blaser; Enantioselective hydrogenation of  $\alpha$ -keto acetals with cinchona modified Pt catalyst; *Chem. Commun.*, 17: 1727–1728, 1999.
- [6] J. A. Groenewegen and W. M. H. Sachtler; Mechanism of asymmetric hydrogenation on modified nickel catalysts; *J. Catal.*, 38(1-3): 501–504, 1975.
- [7] A. Hoek and W. M. H. Sachtler; Enantioselectivity of nickel catalysts modified with tartaric acid or nickel tartrate complexes; *J. Catal.*, 58(2): 276–286, 1979.
- [8] Y. Izumi; Modified Raney nickel (MRNi) catalyst: heterogeneous enantio-differentiating (asymmetric) catalyst; *Adv. Catal.*, 32: 215–271, 1983.
- [9] G. Wittmann, G. B. Bartók, M. Bartók and G. V. Smith; Homogeneous and heterogeneous catalytic asymmetric reactions. Part III. New investigations concerning the preparation of reproducible MRNi catalyst; *J. Mol. Catal.*, 60(1): 1–10, 1990.
- [10] M. A. Keane and G. Webb; The enantioselective hydrogenation of methyl acetoacetate over supported nickel-catalysts. I. The modification procedure; *J. Catal.*, 136(1): 1–15, 1992.
- [11] M. A. Keane; Interaction of optically active tartaric acid with a nickel-silica catalyst: Role of both the modification and reaction media in determining enantioselectivity; *Langmuir*, 13(1): 41–50, 1997.
- [12] A. L. Martínez and M. A. Keane; The gas phase hydrogenation of 2-butanone over supported nickel catalysts: introduction of enantioselectivity; *J. Mol. Catal. A*, 153(1-2): 257–266, 2000.
- [13] M. O. Lorenzo, S. Haq, T. Bertrams, P. Murray, R. Raval and C. J. Baddeley; Creating chiral surfaces for enantioselective heterogeneous catalysis: R,R-tartaric acid on Cu(110); *J. Phys. Chem. B*, 103: 10661–10669, 1999.
- [14] M. O. Lorenzo, C. J. Baddeley, C. Muryn and R. Raval; Extended surface chirality from supramolecular assemblies of adsorbed chiral molecules; *Nature*, 404: 376–378, 2000.
- [15] M. O. Lorenzo, V. Humblot, P. Murray, C. J. Baddeley, S. Haq and R. Raval; Chemical transformations, molecular transport, and kinetic barriers in creating the chiral phase of (R,R)-tartaric acid on Cu(110); *J. Catal.*, 205: 123–134, 2002.
- [16] R. I. Masel, editor; *Principles of Adsorption and Reaction on Solid Surfaces*; Wiley series in chemical engineering. Wiley, New York, 1996.
- [17] R. Raval; Creating chiral architectures at metal surfaces; *J. Phys.: Condens. Matter*, 14: 4119–4132, 2002.
- [18] L. A. M. M. Barbosa and P. Sautet; Stability of chiral domains produced by adsorption of tartaric acid isomers on the Cu(110) surface: periodic density functional theory study; *J. Am. Chem. Soc.*, 123(27): 6639–6648, 2001.
- [19] V. Humblot, S. Haq, C. Muryn, W. A. Hofer and R. Raval; From local adsorption stress

- to chiral surfaces: R,R-tartaric acid on Ni(110); *J. Am. Chem. Soc.*, 124(3): 503–510, 2002.
- [20] T. E. Jones and C. J. Baddeley; A RAIRS, STM and TPD study of the Ni{111}/R,R-tartaric acid system: Modelling of the chiral modification of Ni particles; *Surf. Sci.*, 513: 453–467, 2002.
- [21] S. M. York, S. Haq, K. V. Kilway, J. M. Phillips and F. M. Leibsle; STM, FTIR and quantum chemical calculation studies of acetate structures on Cu(110) surfaces; *Surf. Sci.*, 522: 34–46, 2003.
- [22] V. Humblot, M. O. Lorenzo, C. J. Baddeley, S. Haq and R. Raval; Local and global chirality at surfaces: Succinic acid versus tartaric acid on Cu(110); *J. Am. Chem. Soc.*, 126(20): 6460–6469, 2004.
- [23] P. J. Feibelman; Anisotropy of the stress on fcc(110) surfaces; *Phys. Rev. B*, 51(24): 17867–17875, 1995.
- [24] S. Olivier, A. Saul and G. Treglia; Relation between surface stress and (1x2) reconstruction for (110) fcc transition metal surfaces; *Appl. Surf. Sci.*, 212–213: 866–871, 2003.
- [25] K. Kern, H. Niehus, A. Schatz, P. Zeppenfeld, J. Goerge and G. Comsa; Long-range spatial self-organization in the adsorbate-induced restructuring of surfaces: Cu{110}-(2x1)O; *Phys. Rev. Lett.*, 67(7): 855–858, 1991.
- [26] J. K. Nørskov; *Coadsorption, promoters and poisons*, volume 6 of *The chemical physics of solid surfaces*, chapter 1 Adsorbate-adsorbate interactions on metal surfaces, pages 1–27; Elsevier, 1993.
- [27] G. Kresse and J. Furthmüller; Efficiency of ab-initio total energy calculations for metals and semiconductors using a plane-wave basis set; *Comput. Mater. Sci.*, 6(1): 15–50, 1996.
- [28] G. Kresse and J. Furthmüller; Efficient iterative schemes for ab initio total-energy calculations using a plane-wave basis set; *Phys. Rev. B*, 54(16): 11169–11186, 1996.
- [29] J. Perdew and A. Zunger; Self-interaction correction to density-functional approximations for many-electron systems; *Phys. Rev. B*, 23: 5048–5079, 1981.
- [30] J. Perdew and Y. Wang; Accurate and simple density functional for the electronic exchange energy: Generalized gradient approximation; *Phys. Rev. B*, 33: 8800–8802, 1986.
- [31] D. Vanderbilt; Soft self-consistent pseudopotentials in a generalized eigenvalue formalism; *Phys. Rev. B*, 41(11): 7892–7895, 1990.
- [32] G. Kresse and J. Hafner; Norm-conserving and ultrasoft pseudopotentials for first-row and transition elements; *J. Phys.: Condens. Matter*, 6(40): 8245–8257, 1994.
- [33] C. Kittel; *Introduction to Solid State Physics*; John Wiley eds., Chichester, 1996.
- [34] J. Tabatabaei, B. H. Sakakini, M. J. Watson and K. C. Waugh; The detailed kinetics of the desorption of hydrogen from polycrystalline copper catalysts; *Catal. Lett.*, 59: 143–149, 1999.
- [35] T. Genger, O. Hinrichsen and M. Muhler; The temperature-programmed desorption of hydrogen from copper surfaces; *Catal. Lett.*, 59(2-4): 137–141, 1999.
- [36] S. Haq and F. M. Leibsle; Acetate on Cu(110): evidence for long-range intermolecular interactions and molecular-induced restructuring of a metal surface; *Surf. Sci.*, 355: L345–L349, 1996.
- [37] F. M. Leibsle, S. Haq, B. G. Frederick, M. Bowker and N. V. Richardson; Molecularly induced step faceting on Cu(110) surfaces; *Surf. Sci. Lett.*, 343: L1175–L1181, 1995.
- [38] Q. Chen, D. J. Frankel and N. V. Richardson; Organic adsorbate induced surface reconstruction: p-aminobenzoic acid on Cu(110); *Langmuir*, 17: 8276–8280, 2001.
- [39] Q. Chen, C. C. Perry, B. G. Frederick, P. W. Murray, S. Haq and N. V. Richardson; Struc-

- tural aspects of the low-temperature deprotonation of benzoic acid on Cu(110) surfaces; *Surf. Sci.*, 446: 63–75, 2000.
- [40] O. Karis, J. Hasselström, N. Wassdahl, M. Weinelt, A. Nilsson, M. Nyberg, L. G. M. Pettersson, J. Stöhr and M. G. Samant; The bonding of simple carboxylic acids to Cu(110); *J. Chem. Phys.*, 112(18): 8146–8155, 2000.
- [41] J. M. Philips, F. M. Leibsle, A. J. Holder and T. Keith; A comparative study of chemisorption by density functional theory, ab initio, and semi-empirical methods: carbon monoxide, formate and acetate on Cu(110); *Surf. Sci.*, 545: 1–7, 2003.
- [42] S. Haq and F. M. Leibsle; Erratum to “Acetate on Cu(110): evidence for long-range intermolecular interactions and molecular-induced restructuring of a metal surface” [*Surface Science* 355 (1996) L345]; *Surf. Sci.*, 367: L66–L66, 1996.
- [43] P. Baumann, H. P. Bonzel, G. Pirug and J. Werner; Long-range ordered acetate structure on Cu(110); *Chem. Phys. Lett.*, 260: 215–222, 1996.





## CHAPTER 5

# MODELLING THE BUTTERFLY: BRIDGE-BOUND ANIONS

The adsorption of a bridge-bonded anion onto an fcc(111) surface is studied using kinetic Monte Carlo simulations. Different models with first neighbour shell exclusion and finite second neighbour shell lateral interactions are considered. All simulated voltammograms show one peak associated with anion adsorption in a disordered phase, and one peak related to a disorder-order transition in the adlayer. The disorder-order transition transforms the adlayer with a coverage of 0.18 ML into a  $(\sqrt{3} \times \sqrt{7})$  ordered structure with a coverage of 0.20 ML. The shape of the adsorption isotherm and the simulated voltammogram is strongly influenced by attractive or repulsive lateral interactions, as well as by the sweep rate and the presence of steps in the surface.

### 5.1 INTRODUCTION

In a typical electrochemical experiment one brings a solution of ions into contact with an electrode. If we focus on the anions (i.e., the negatively charged ions) only, then part of these anions will adsorb on the electrode surface, while the rest remains in solution. The anions are (partially) discharged during adsorption by transfer of electrons to the electrode. This adsorption current can be measured. The potential of the electrode determines how many anions will adsorb. By varying the potential of the electrode one can perform adsorption/desorption experiments of the ions. This is used in linear sweep voltammetry. In linear sweep voltammetry one starts with the electrode at a negative potential, such that no anions are adsorbed on the electrode surface. Next, the electrode potential is linearly increased with time (or “swept”) up to a certain value. This causes adsorption of the anions present. During the sweep the current is measured as a function of time, and this momentary current is a measure

for the adsorption rate of the anion. One can easily extend this type of experiment; if the potential is subsequently gradually decreased to the starting potential, electrons will be transferred from the electrode to the adsorbed anions, which will then leave the surface. The current measured while decreasing the electrode potential is similar to the current measured while increasing the electrode potential, but opposite in sign. The experiment where the potential is first increased to some value and then reduced to the original value is referred to as cyclic voltammetry [1].

The adsorption of anions on single-crystal electrode surfaces usually gives rise to the appearance of ordered adsorbate adlayers. The formation of these ordered adlayers is often accompanied by a characteristic sharply peaked current response in the cyclic voltammetry, commonly referred to as “butterfly” in the electrochemical community (see for an example Fig. 5.1) [2–4]. These adsorbed anions are, apart from their characteristic voltammetric response, also known to influence profoundly the electrochemical and structural properties of electrode surfaces. Adsorbed anions influence the reactivity, they may cause reorientation of the steps at the surface and suppress oxidation of the surface [5–7]. They may cause, but also lift reconstructions of the surface [8–11]. Finally they can greatly enhance metal dissolution, or be used in under-potential deposition (UPD) [5, 12–14]. Understanding these processes requires a thorough insight into the interactions between the anion and the surface and among the anions themselves, thus meriting theoretical study. Previous studies trying to model specific anion adsorption have treated atop and fourfold hollow adsorption of ions on fcc(100) and atop and threefold hollow adsorption on fcc(111) surfaces [15–23]. From these studies it has become clear that the combination of the adsorption site and the lateral interactions defines the voltammogram shape and the ordered structure formed.

In extension to these studies we treat here bridge-bonded adsorption on fcc(111) surfaces in the presence of lateral interactions. The distinguishing factor of the model considered here from those studied previously is that the interaction model does not have the same symmetry as the underlying substrate. We show that the behaviour of this model anion has many similarities to the adsorption behaviour of (bi)sulfate on fcc(111) surfaces. The simulated voltammogram shows a broad peak associated with adsorption in a disordered phase, and a sharp one associated with a disorder-order transition in the adlayer. The disorder-order transition converts the adlayer with a coverage of 0.18 ML into a  $(\sqrt{3} \times \sqrt{7})$  ordered structure with a coverage of 0.20 ML. The  $(\sqrt{3} \times \sqrt{7})$  structure with 0.20 ML saturation coverage is experimentally known for the adsorption of anions from sulfuric acid solution on many fcc(111) surfaces. The anion involved is either bisulfate ( $\text{HSO}_4^-$ ) or sulfate ( $\text{SO}_4^{2-}$ ).

Previous models of this system assumed threefold-bound (bi)sulfate, and were only able to explain the  $(\sqrt{3} \times \sqrt{7})$  structure by using a complicated set of two- and three-particle interactions. The model presented here does not require such interactions, and is therefore more promising.

Many different effects are likely to influence the adsorption of (bi)sulfate on these fcc(111) surfaces. In this article we will systematically study these effects for our model anion. We start with the influence of the voltammetric sweep rate and the

presence of steps on the surface. Next we treat the influence of both attractive and repulsive interactions between the adsorbates on the voltammogram. We also discuss the consequences for the voltammogram shape of having both sulfate and bisulfate on the surface. We conclude by linking the effects found for our model anion to experimental data.

## 5.2 MODEL

We model the adsorption of the adsorbate (an anion A) by Monte Carlo simulations employing a lattice-gas model for the substrate:



where \*\* denotes an empty bridge site (formed by two empty surface atoms); each \* corresponds to a surface atom. Fig. 5.2 shows the (111) substrate and the neighbouring sites around a central bridge-bonded adsorbate (in black). We model the interactions between the adsorbates in two different ways. First, we consider a shell of purely hard interactions, in which the simultaneous bonding of two anions to neighbouring sites is simply excluded. These excluded neighbouring sites are displayed in white in Fig. 5.2. This model is equivalent to the elongated hard hexagon model considered by Orts *et al.* [24]. Next, we consider a second shell of neighbouring sites with either finite attractive or finite repulsive interactions  $\varepsilon_{ij}$ . These are displayed in grey in Fig. 5.2. A negative value of  $\varepsilon_{ij}$  here indicates that the interaction is attractive. The exclusion of the first shell of neighbouring sites is a very common approximation related to the fact that the metal-metal distance is usually smaller than the Van der Waals diameter of the adsorbate [16, 17]. Significant repulsion is therefore expected if two adsorbates bind this close together.

The isotherms were calculated by determining the coverage  $\theta$  on the lattice as a function of the electrode potential  $E$ . The isotherms were calculated by including adsorption, desorption and surface diffusion steps and scanning  $E$ . The algorithm used was the First Reaction Method. In this algorithm, a tentative time is calculated for every possible reaction. All reactions together with their tentative times are stored in an event list. The algorithm proceeds by repeatedly performing the following steps: select the reaction with minimal time from the event list, advance the system time to the time of this reaction, adjust the lattice according to the reaction, and update the event list. For the case of time-dependent rate constants (such as in voltammetry, where rate constants are time dependent because of the time dependent potential), one can determine the tentative times exactly or approximate them by taking the rate constants constant for a small time step. In this work the times were determined exactly. We have used kinetic Monte Carlo simulations rather than equilibrium Monte Carlo simulations to allow us to study also the non-equilibrium adsorption of anions, which is important for high sweep rates. The rate constants for adsorption and desorption

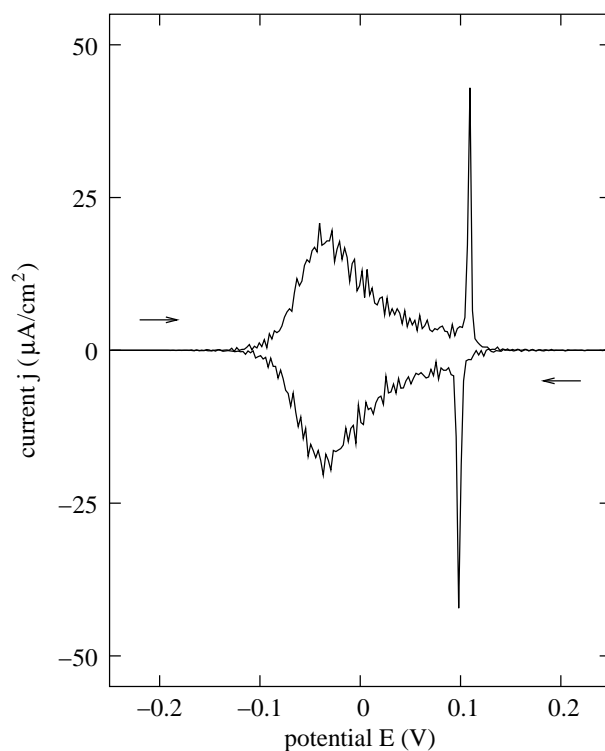


Figure 5.1: Simulated cyclic voltammogram (or “butterfly”) for the model described in Fig. 5.2 with first neighbour shell exclusion. The potential was increased from  $-0.25$  to  $+0.25$  V with a sweep rate of  $+20$  mV/s, and then decreased to  $-0.25$  V with a sweep rate of  $-20$  mV/s. At  $-0.25$  V the surface is empty, while at  $+0.25$  V the surface is fully covered with anions. The positive-going sweep is displayed in the top half of the figure. This current corresponds to adsorption of the anion. The negative-going sweep, which is shown in the bottom half of the figure, corresponds to desorption of the anion. The sharp spike in the current at  $0.1$  V in the positive-going sweep is due to the formation of an ordered phase in the adlayer. The sharp spike in the current at  $0.1$  V in the negative-going sweep is due to the break-up of the ordered phase.

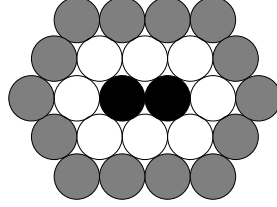


Figure 5.2: Lateral interaction model on a fcc(111) lattice. The adsorbed anion binds to two surface atoms in a bridged fashion (black atoms), making bonding to the first shell of neighbouring sites (white) impossible. There is a finite attractive or repulsive interaction with anions binding to the second neighbour shell (grey).

are:

$$k_{\text{ads}} = k^0 \exp\left(\frac{-\alpha_{\text{ads}}\gamma eE}{k_{\text{B}}T}\right) \exp\left(\frac{-\zeta_{\text{ads}}N\varepsilon_{ij}}{k_{\text{B}}T}\right) \quad (5.2)$$

$$k_{\text{des}} = k^0 \exp\left(\frac{\alpha_{\text{des}}\gamma eE}{k_{\text{B}}T}\right) \exp\left(\frac{\zeta_{\text{des}}N\varepsilon_{ij}}{k_{\text{B}}T}\right) \quad (5.3)$$

where  $\alpha_{\text{ads}} = 1/2$  is the transfer coefficient for adsorption,  $\gamma$  is the electrosorption valency (taken as -2 unless otherwise stated),  $e$  is the elementary charge,  $E$  is the electrode potential,  $\zeta_{\text{ads}} = 1/2$  is the Brønsted-Evans-Polanyi coefficient for adsorption, and  $N$  is the number of occupied second neighbour shell sites in the adsorbed state. The first exponent describes the potential-dependent adsorption of the anion, the second exponent describes the potential-independent change in binding energy due to the interaction  $\varepsilon_{ij}$  between the adsorbed anions. The definitions in equations 5.2 and 5.3 imply that in our model at zero potential the adsorption rate constant is equal to the desorption rate constant:  $k_{\text{ads}} = k_{\text{des}} = k^0$ , if  $\varepsilon_{ij} = 0$ . The transfer coefficient and Brønsted-Evans-Polanyi coefficient for desorption are given by

$$\alpha_{\text{des}} = 1 - \alpha_{\text{ads}} \quad (5.4)$$

and

$$\zeta_{\text{des}} = 1 - \zeta_{\text{ads}}. \quad (5.5)$$

The diffusion steps were defined as hopping between neighbouring bridge sites. The diffusion rate constants were chosen such that detailed balance was satisfied:

$$k_{\text{diff}} = k_{\text{diff}}^0 \exp\left(\frac{-\zeta_{\text{diff}}\Delta N\varepsilon_{ij}}{k_{\text{B}}T}\right), \quad (5.6)$$

where  $\zeta_{\text{diff}} = 1/2$  is the Brønsted-Evans-Polanyi coefficient for diffusion and  $\Delta N$  is the difference in the number of occupied second neighbour shell sites before and after the hop. If after the hop the anion has more second neighbour shell neighbours, then

a negative value of  $\varepsilon_{ij}$  (an attractive interaction) will make the exponent positive, thus making the hop more probable.

Apart from the coverage-voltage ( $\theta-E$ ) isotherm itself, we are particularly interested in the compressibility  $d\theta/dE$  of the adlayer, as this quantity is proportional to the Faradaic current measured in an electrochemical voltammetry experiment:

$$j = -e\gamma\Gamma_m\nu\frac{d\theta}{dE}, \quad (5.7)$$

where  $j$  is the Faradaic current in  $\text{A}/\text{cm}^2$ ,  $\Gamma_m$  is the number of surface sites per unit surface area (taken to be  $1.5 \times 10^{15}$  sites/ $\text{cm}^2$ ), and  $\nu$  is the sweep rate (typically 50 mV/s).

The voltammograms shown here are averages over four individual simulations on a  $256 \times 256$  lattice with periodic boundary conditions, to increase the signal-to-noise ratio. The temperature was fixed at 300 K. The compressibility  $d\theta/dE$  of the adlayer was determined by taking the difference of the adsorption and the desorption rate for each time interval of 0.05 s and dividing it by the sweep rate. The disorder-order transition at 0.11 V in Fig. 5.3 is particularly sensitive to the level of equilibration; an insensitivity of this peak to reducing the sweep rate indicates that the surface is well equilibrated. The isotherms were therefore calculated by choosing the rates of adsorption, desorption and diffusion such that upon reducing the sweep rate from 50 to 5 mV/s the disorder-order transition peak is shifted by less than 5 mV. This is also what is expected experimentally. The values fulfilling this requirement are  $k^0 = 10^3 \text{ s}^{-1}$  and  $k_{\text{diff}}^0 = 10^5 \text{ s}^{-1}$ . The sweep rate used was 50 mV/s unless stated otherwise. All snapshots are  $30 \times 30$  sites, taken from the full simulated grid of  $256 \times 256$  sites.

### 5.3 LINEAR SWEEP VOLTAMMETRY AND ORDERING

Figure 5.3 shows the adsorption isotherm and simulated voltammogram for the model described in Fig. 5.2 with first neighbour shell exclusion and no interaction with the second neighbour shell ( $\varepsilon_{ij} = 0$ ). Going from more negative to more positive potential, the anion adsorbs between -0.1 and 0.1 V in a disordered phase (see snapshots in Fig. 5.4a,b). This results in a broad adsorption peak in the voltammogram. There is a disorder-order transition at 0.11 V, indicated by the sharp peak in the voltammogram. At this voltage the anion coverage rapidly increases from 0.18 ML to 0.20 ML, which is the saturation coverage. This result was previously obtained by Orts *et al.* using an elongated hard hexagon type model [24]. The onset of the disorder-order transition is shown in Fig. 5.4c.  $(\sqrt{3} \times \sqrt{7})$  Islands are forming, and, as indicated in the figure, these can have three different orientations. After the disorder-order transition (at potentials of 0.12 V and above) only large  $(\sqrt{3} \times \sqrt{7})$  domains are present on the surface. These typically consist of more than thousand adsorbates. The  $(\sqrt{3} \times \sqrt{7})$  ordered structure shown in Fig. 5.4d can also be referred to as  $\begin{pmatrix} 2 & 1 \\ 1 & 2 \end{pmatrix}$ , using the matrix notation, which relates the unit cell vectors of the adsorbate overlayer to the

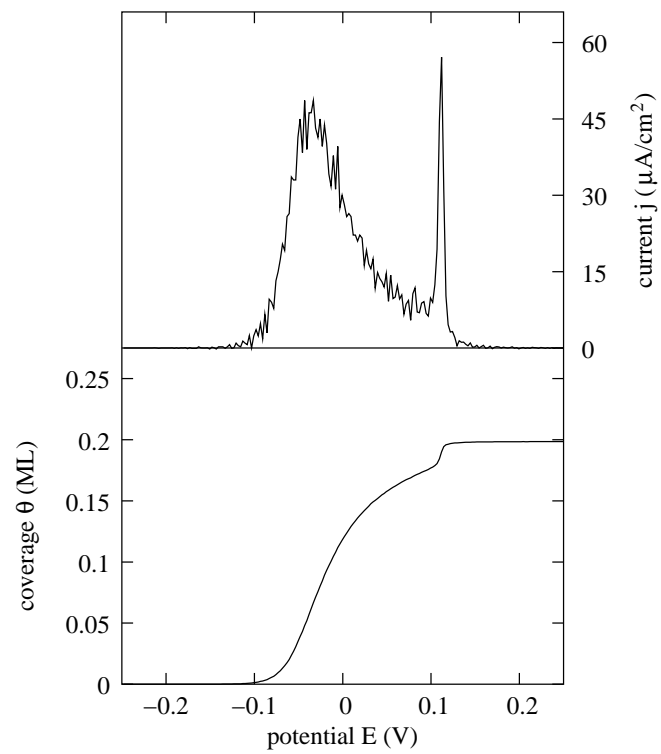
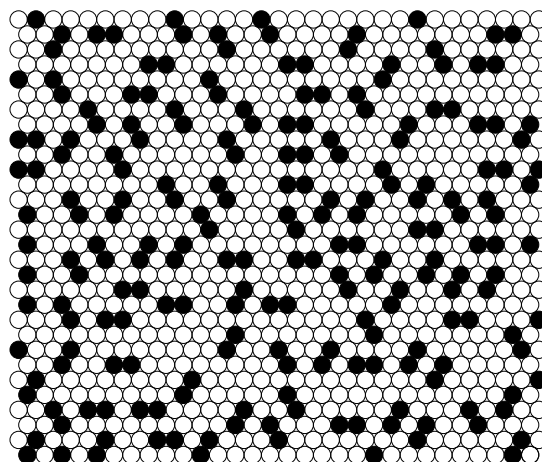
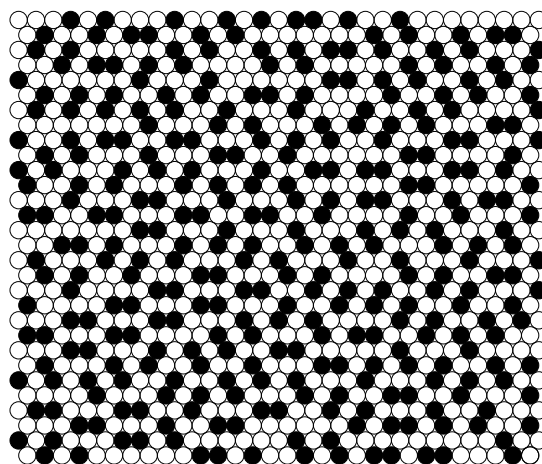


Figure 5.3: Simulated voltammogram (top) and adsorption isotherm (bottom) for the model with first neighbour shell exclusion.



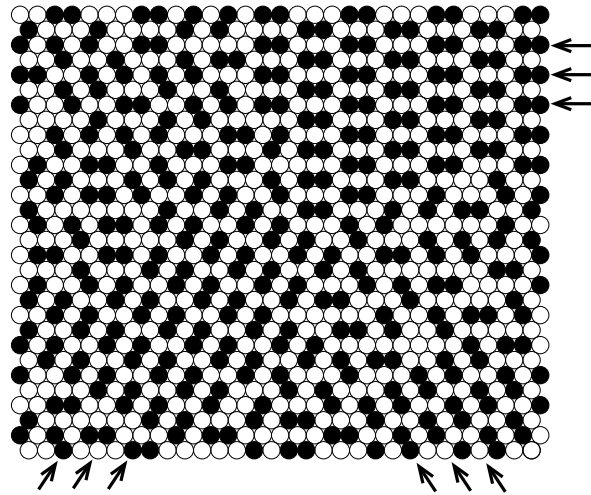


a: 0.00 V, 0.12 ML

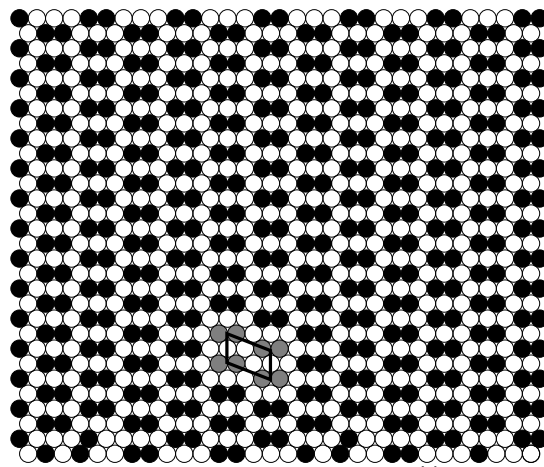


b: 0.10 V, 0.18 ML

Figure 5.4: Snapshots of the surface during anion adsorption for the model with first neighbour shell exclusion. Before the disorder-order transition (panel (a) and (b)) there is no ordering.



c: 0.11 V, 0.19 ML



d: 0.12 V, 0.20 ML

$$\begin{pmatrix} 0 \\ 1 \end{pmatrix} \rightarrow \begin{pmatrix} 1 \\ 0 \end{pmatrix}$$

Figure 5.4: (continued) During the disorder-order transition  $(\sqrt{3} \times \sqrt{7})$  islands grow (c); the three different domain orientations are indicated by the small arrows); after the disorder-order transition large islands dominate (d). The  $(\sqrt{3} \times \sqrt{7})$  unit cell is indicated in (d).

unit cell vectors of the surface. The other two (rotationally equivalent) domains indicated at the lower left and the lower right part of Fig. 5.4c are then described by

$$\begin{pmatrix} 3 & \bar{1} \\ 2 & 1 \end{pmatrix} \text{ and } \begin{pmatrix} 2 & \bar{1} \\ 1 & 2 \end{pmatrix}.$$

At 0.10 V, the surface is occupied by anions which have three different orientations. Packing of equal amounts of these anions of different orientations is only possible up to about 0.18 ML. This causes a decrease in the adsorption current close to 0.10 V. It is only with the alignment of the adsorbates in the same direction that more anions can adsorb, since the ordered ( $\sqrt{3} \times \sqrt{7}$ ) structure allows for a tighter packing of anions.

### 5.3.1 THE INFLUENCE OF THE SWEEP RATE

Upon increasing the sweep rate from 50 to 500 mV/s the voltammogram remains largely the same, only the peak corresponding to the disorder-order transition becomes broader and shifts to higher potential (Figure 5.5). This is because the equilibration of the adlayer by means of desorption and diffusion does not keep up with the adsorption. The desorption rate decreases rapidly with increasing potential, thus preventing long-range ordering. The ordered islands formed on the surface are smaller and the total coverage is lower, since ordered packing allows for the largest amount of anions binding to the surface. For a sweep rate of 5000 mV/s, the peak of the disorder-order transition completely disappears from the voltammogram, leaving only small ordered islands typically consisting of 50–100 adsorbates. Sweep rates smaller than 50 mV/s give a sharper disorder-order transition peak. The full width at half maximum (FWHM) of the disorder-order transition peak for a sweep rate of 50 mV/s as shown in Fig. 5.5 equals 7 mV. When a lower sweep rate of 5 mV/s is used, the peak sharpens even further and the full width at half maximum becomes smaller than the voltage interval over which the current was determined, which was 2.5 mV (not shown). Since the disorder-order transition is very sharp, it is difficult to determine the order of the transition. By similarity to the hard hexagon model we expect it to be second order [25].

### 5.3.2 THE INFLUENCE OF THE TERRACE SIZE

The presence of defects in the surface prevents long-range ordering of adsorbates. The voltammogram is therefore expected to change when steps are introduced. We have investigated this effect by introducing step sites at regular intervals in our model. Bonding to these step sites is excluded, and the adsorbates are also not allowed to diffuse across the steps. Our results indicate that for different terrace sizes only the disorder-order transition peak changes (as expected); the broad peak associated with adsorption in a disordered phase hardly changes. This is similar to the case of fast adsorption presented in the previous section. The disorder-order transition peak decreases in intensity with decreasing terrace size (Figure 5.6). The saturation coverage decreases as well. For terrace sizes of 64 and larger, the orientation of the ( $\sqrt{3} \times \sqrt{7}$ )

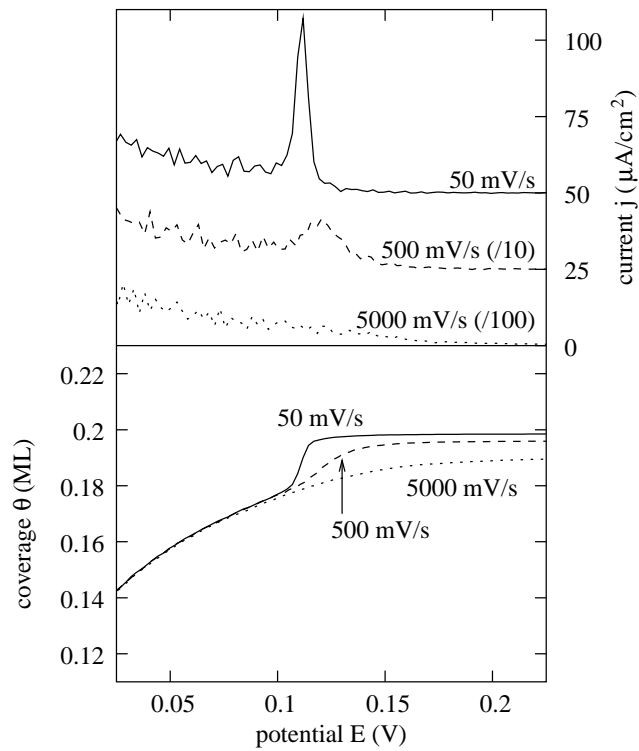


Figure 5.5: Simulated voltammogram (top) and adsorption isotherm (bottom) for the model with first neighbour shell exclusion. Fast adsorption with a sweep rate of 5000 mV/s (dotted line) and 500 mV/s (dashed line) compared to slow adsorption, 50 mV/s (solid line).

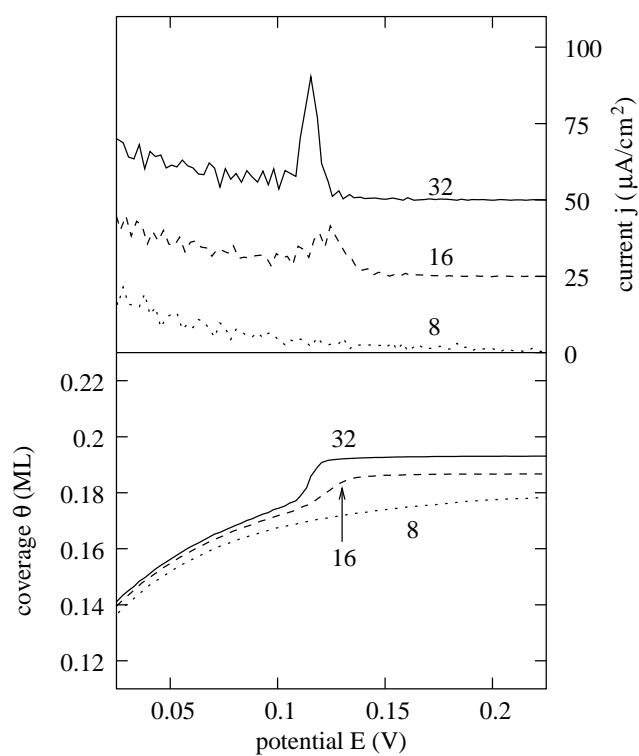


Figure 5.6: Simulated voltammogram (top) and adsorption isotherm (bottom) for the model with first neighbour shell exclusion. Adsorption with a terrace width of 8 (dotted line), 16 (dashed line) and 32 (solid line) sites.

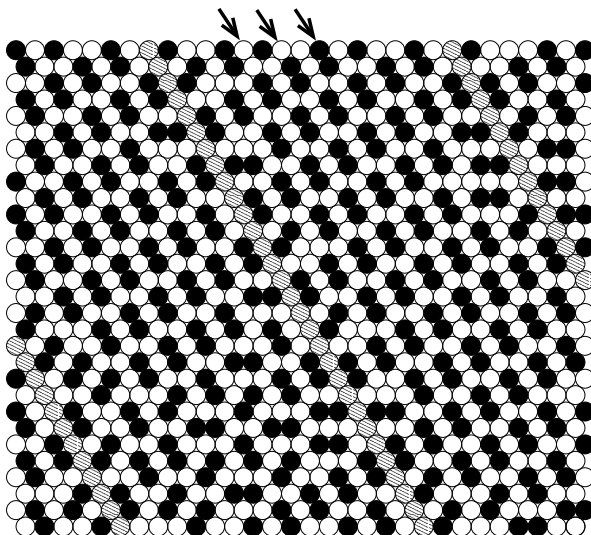


Figure 5.7: Snapshot of the surface at 0.25 V after anion adsorption for the model with first neighbour shell exclusion and a terrace width of 16. Bonding to the steps (shaded circles) is forbidden. The arrows show the alignment of the adsorbate islands (in black) to the steps (shaded), the coverage equals 0.19 ML.

domains is independent of the step orientation; i.e., islands of all the three different orientations of the  $(\sqrt{3} \times \sqrt{7})$  structure are found. The intensity of the disorder-order transition peak is comparable to the one for the case without steps. For terrace sizes of 16 and 32, the  $(\sqrt{3} \times \sqrt{7})$  domains align to the steps, as shown in Figure 5.7. For an even smaller terrace size of 8, no ordering is observed, even if the sweep rate is reduced to 5 mV/s.

### 5.3.3 ATTRACTIVE INTERACTIONS

Interactions between the adsorbed anions strongly influence the adsorption isotherms. An attraction ( $\varepsilon_{ij} < 0$ ) causes the broad peak associated with adsorption in a disordered phase to sharpen and shift to lower potential (Figure 5.8). At the same time the disorder-order transition peak loses intensity and also shifts to lower potential. The adsorbates on the surface group together in islands even at low coverages, but within the islands there is initially no ordering. Only at a coverage of 0.18 ML does the disorder-order transition take place and are  $(\sqrt{3} \times \sqrt{7})$  ordered domains formed. The islands are slightly smaller in size (100–500 adsorbates) than the ones obtained for the simulations without interactions. This is due to the attractions between the adsorbates, which effectively reduce the diffusion rate. Small  $(\sqrt{3} \times \sqrt{7})$  islands of different orientations are therefore less easily joined into larger islands, and packing

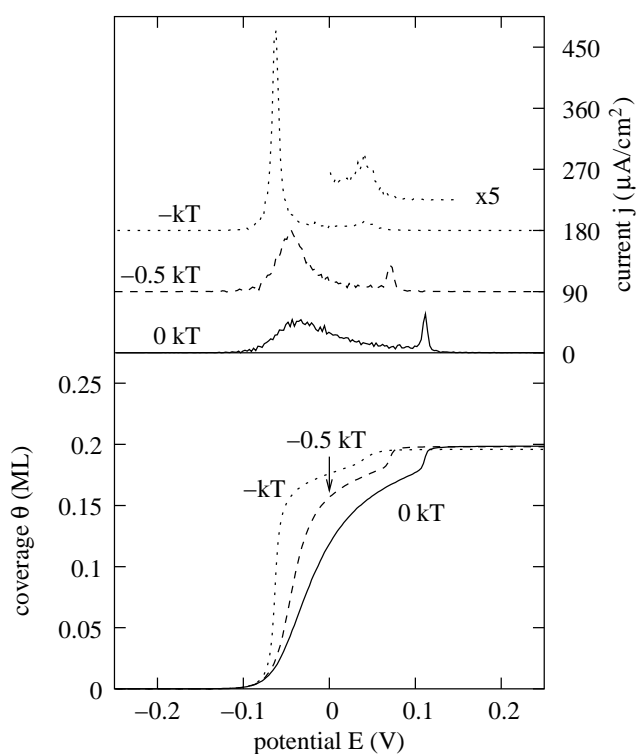


Figure 5.8: Simulated voltammogram (top) and adsorption isotherm (bottom) for the model with first neighbour shell exclusion and second neighbour shell attraction. Adsorption with an attraction of  $-k_B T$  (dotted line) and  $-0.5 k_B T$  (dashed line) compared to the case without interaction (solid line).

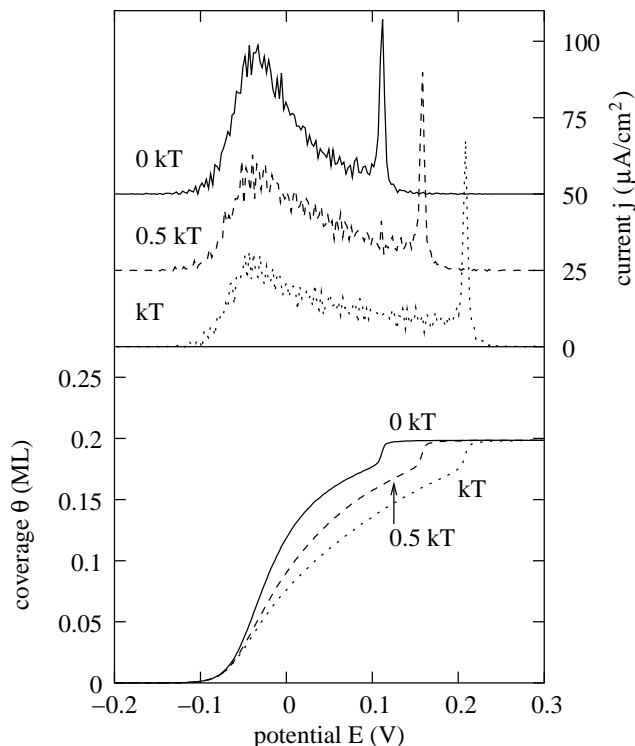


Figure 5.9: Simulated voltammogram (top) and adsorption isotherm (bottom) for the model with first neighbour shell exclusion and second neighbour shell repulsion. Adsorption with a repulsion of  $k_B T$  (dotted line) and  $0.5 k_B T$  (dashed line) compared to the case without interaction (solid line).

faults are less readily removed. The sharpening up of the adsorption peak because of attractive interactions is due to (1) a shift in the adsorption/desorption equilibrium, since the adsorption and desorption rate constants are influenced by the presence of neighbouring adsorbates, and (2) the presence of more sites accessible for adsorption, since the empty sites are joined into adsorbate-free areas.

#### 5.3.4 REPULSIVE INTERACTIONS

A repulsion ( $\epsilon_{ij} > 0$ ) causes the broad peak associated with adsorption in a disordered phase to broaden even further (Figure 5.9). The onset of adsorption is not influenced, since repulsive interactions only become apparent at higher coverages. Only at higher voltages does adsorption become more troublesome, and the broad peak associated with adsorption in a disordered phase thus extends to higher potential. The disorder-

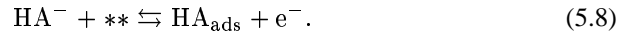


order transition in this case retains its intensity, it only shifts to higher potential. After the adsorption sweep, large ordered islands of the  $(\sqrt{3} \times \sqrt{7})$  structure are formed, despite the repulsive interactions. These islands are comparable in size to the ones obtained for the simulations without interactions.

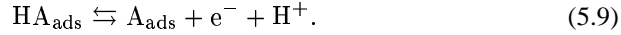
### 5.3.5 SEQUENTIAL TRANSFER OF THE ELECTRONS

As mentioned in the introduction, anion adsorption from sulfuric acid solutions can be as bisulfate ( $\text{HSO}_4^-$ ) or sulfate ( $\text{SO}_4^{2-}$ ). In the previous sections we have assumed the anion to be sulfate-like, and two electrons were transferred per model anion. In this section we extend our model to include also adsorption of bisulfate. Bisulfate, upon adsorption on the surface, transfers initially only one electron. If it is deprotonated to sulfate at a higher potential, then it may transfer a second electron to the surface.

The adsorption in our model then becomes:



The species adsorbed on the surface can then be deprotonated to yield the second electron:



This second reaction is an acid/base equilibrium where the charge of the base is neutralised by the surface. For simplicity we have taken  $\text{HA}_{\text{ads}}$  and  $\text{A}_{\text{ads}}$  both to be bonded in a bridging fashion as displayed in Figure 5.2. We assume  $\text{HA}_{\text{ads}}$  and  $\text{A}_{\text{ads}}$  to be completely discharged. However, the key quantity here is the electrosorption valency, which has been taken -1 for both reactions. This electrosorption valency could also correspond to a transfer of the anion through the double layer. Both  $\text{HA}_{\text{ads}}$  and  $\text{A}_{\text{ads}}$  are allowed to diffuse across the surface, only  $\text{HA}_{\text{ads}}$  is allowed to desorb. No attractive or repulsive interactions were used.

The rate constants for the adsorption equilibrium in Eqn. 5.8 is still described by Eqns. 5.2 and 5.3. We can write the following expressions for the rate constants in our simulation that describe Eqn. 5.9:

$$k_{\text{HA} \rightarrow \text{A}} = k_f^0 \exp\left(\frac{-\alpha_f \gamma e E}{k_B T}\right) \quad (5.10)$$

$$k_{\text{A} \rightarrow \text{HA}} = k_b^0 \exp\left(\frac{(1 - \alpha_f) \gamma e E}{k_B T}\right) \quad (5.11)$$

where  $\alpha_f$  is the transfer coefficient for the forward (acid) reaction, taken to be 1/2, and  $\gamma$  equals -1. We assume that these reactions are in equilibrium during the entire simulation by taking  $k_f^0$  and  $k_b^0$  sufficiently large. The microscopic rate constants  $k_f^0$  and  $k_b^0$  can be related to their macroscopic counterparts:

$$k_f^0 = k_{\text{acid}} \quad (5.12)$$

$$k_b^0 = k_{\text{base}}[\text{H}^+] \quad (5.13)$$

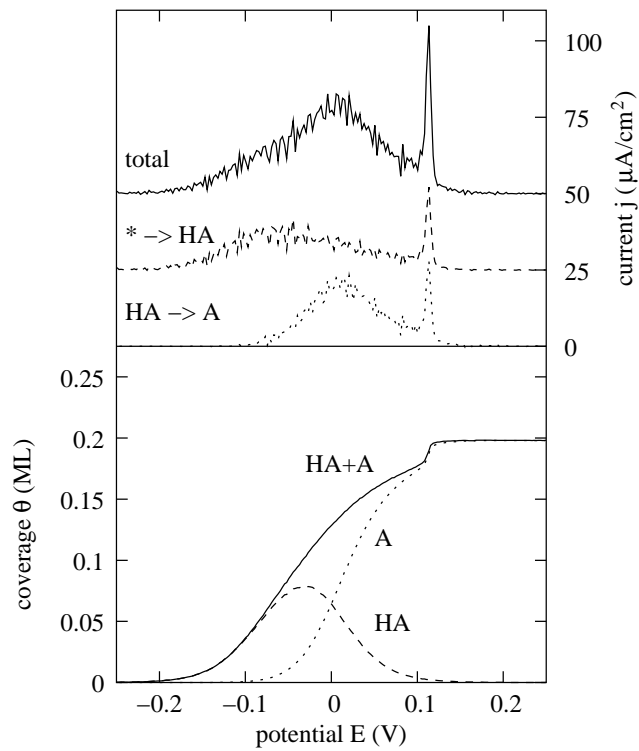


Figure 5.10: Simulated voltammogram (top) and adsorption isotherm (bottom) for the model with first neighbour shell exclusion and sequential electron transfer. The ratio of the acid constant to the hydronium ion concentration,  $K_a/[\text{H}^+]$ , equals 1. Partial coverages of  $\text{HA}_{\text{ads}}$  (dashed line),  $\text{A}_{\text{ads}}$  (dotted line) and the total coverage (solid line) are indicated in the lower panel. The current due to adsorption of  $\text{HA}_{\text{ads}}$  (dashed line), the current due to conversion of  $\text{HA}_{\text{ads}}$  into  $\text{A}_{\text{ads}}$  (dotted line) and the total current (solid line) are indicated in the top panel.

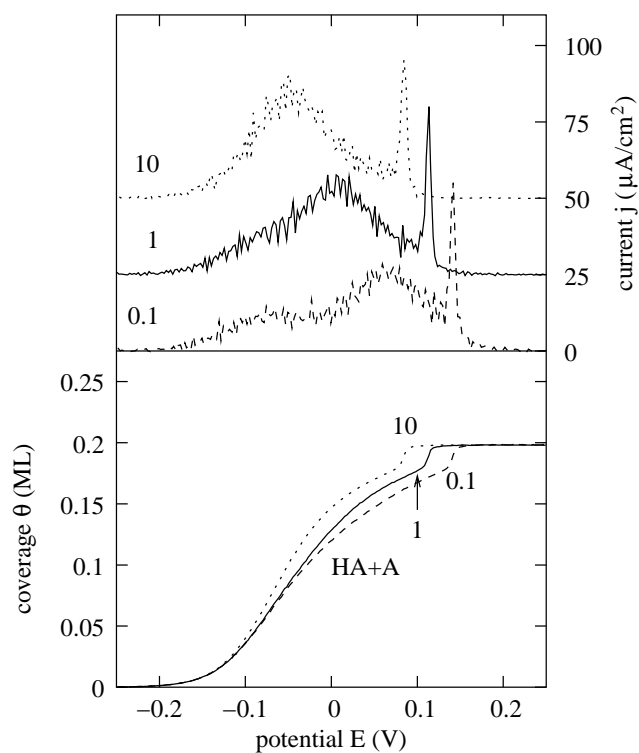


Figure 5.11: Simulated voltammogram (top) and adsorption isotherm (bottom) for the model with first neighbour shell exclusion and sequential electron transfer. The ratio of the acid constant to the hydronium ion concentration,  $K_a/[H^+]$ , equals 0.1 (dashed line), 1 (solid line), and 10 (dotted line) respectively. Indicated coverage is the total coverage of  $HA_{ads}$  and  $A_{ads}$  together.

where  $k_{\text{acid}}$  and  $k_{\text{base}}$  are the macroscopic acid and base constants respectively, and  $[\text{H}^+]$  is the hydronium ion concentration. The ratio  $k_f^0/k_b^0$  can then be written as

$$\frac{k_f^0}{k_b^0} = \frac{k_{\text{acid}}}{k_{\text{base}}[\text{H}^+]} = \frac{K_a}{[\text{H}^+]}, \quad (5.14)$$

where  $K_a$  is the equilibrium acid constant.

We first discuss the case where the ratio  $K_a/[\text{H}^+]$  has some intermediate value. Next we will discuss the limits of  $K_a/[\text{H}^+]$  going to infinity or zero. The voltammogram for  $K_a/[\text{H}^+] = 1$  is displayed in Fig. 5.10. For voltages more negative than -0.05 V, the surface is mainly occupied by  $\text{HA}_{\text{ads}}$ , and the current measured is only due to adsorption (dashed line). Between -0.05 V and +0.05 V adsorption continues, and the majority species on the surface changes from  $\text{HA}_{\text{ads}}$  into  $\text{A}_{\text{ads}}$ . This causes, aside from the adsorption current, a broad current peak due to conversion of  $\text{HA}_{\text{ads}}$  into  $\text{A}_{\text{ads}}$  (dotted line in the upper panel). The conversion yields the second electron per adsorbate. At potentials more positive than +0.05 V,  $\text{HA}_{\text{ads}}$  is immediately converted into  $\text{A}_{\text{ads}}$  upon adsorption, and the adsorption and conversion current (dashed and dotted line) are therefore identical. The total measured current consists of two components, one due to adsorption to form  $\text{HA}_{\text{ads}}$ , and one due to the conversion of  $\text{HA}_{\text{ads}}$  into  $\text{A}_{\text{ads}}$ .

The value of the ratio  $K_a/[\text{H}^+]$  determines at which potential the majority species changes from  $\text{HA}_{\text{ads}}$  to  $\text{A}_{\text{ads}}$ . A high value of this ratio (indicating a strong acid and/or a low hydronium ion concentration) causes the surface to be occupied by  $\text{A}_{\text{ads}}$  even at low potentials. The current peak due to conversion of  $\text{HA}_{\text{ads}}$  into  $\text{A}_{\text{ads}}$  then essentially coincides with the current peak due to adsorption of  $\text{HA}_{\text{ads}}$ . This is shown by the dotted line for a ratio  $K_a/[\text{H}^+] = 10$  in Figure 5.11. The model becomes identical to our original model when the ratio  $K_a/[\text{H}^+]$  goes to infinity: in that case both electrons are transferred simultaneously, and the only adsorbed species is  $\text{A}_{\text{ads}}$ . The voltammogram for that case is similar to the one depicted in Fig. 5.3, except that it is shifted to lower potentials (because of the different way the model has been defined). The size of the shift increases with the ratio of the acid constant to the hydronium ion concentration,  $K_a/[\text{H}^+]$ . This is due to the fact that the coverage of  $\text{HA}_{\text{ads}}$  is controlled by the adsorption equilibrium in Eqn. 5.8. If at a certain potential some of the  $\text{HA}_{\text{ads}}$  is converted into  $\text{A}_{\text{ads}}$ , the adsorption equilibrium will be restored by adsorbing additional  $\text{HA}_{\text{ads}}$ . This causes an increase in the total coverage of  $\text{HA}_{\text{ads}}$  and  $\text{A}_{\text{ads}}$  together. If more  $\text{HA}_{\text{ads}}$  is converted into  $\text{A}_{\text{ads}}$ , thus, if the acid  $\text{HA}_{\text{ads}}$  is stronger, more  $\text{HA}_{\text{ads}}$  needs to be adsorbed to restore the adsorption equilibrium, and the total coverage will be higher. This causes the down-shift of the adsorption isotherm.

Figure 5.11 also shows the case where  $K_a/[\text{H}^+] = 0.1$ . In this case the current peak due to conversion of  $\text{HA}_{\text{ads}}$  into  $\text{A}_{\text{ads}}$  is shifted to higher potentials, ranging from 0.0 to +0.1 V. It needs to be mentioned that if the  $K_a/[\text{H}^+]$  ratio is further decreased, the broad peak for the conversion of  $\text{HA}_{\text{ads}}$  into  $\text{A}_{\text{ads}}$  can shift into and even to the right (positive) side of the disorder-order transition. The disorder-order transition only depends on the geometry and lateral interactions of the adsorbates present, not on

the amount of electrons these adsorbates have transferred previously. Both  $\text{HA}_{\text{ads}}$  and  $\text{A}_{\text{ads}}$  are modelled in the same way, as binding in a bridging fashion with first neighbour shell exclusion, thus the disorder-order transition also takes place in the mixed  $\text{HA}_{\text{ads}}+\text{A}_{\text{ads}}$  adlayer when the total coverage exceeds 0.18 ML. In practice the species  $\text{HA}_{\text{ads}}$  may well be adsorbed in a different fashion than  $\text{A}_{\text{ads}}$ , for example threefold bound instead of bridged. In this case the disorder-order transition will not take place in the mixed  $\text{HA}_{\text{ads}}+\text{A}_{\text{ads}}$  adlayer, but will be shifted to higher potentials where all the  $\text{HA}_{\text{ads}}$  has been converted into  $\text{A}_{\text{ads}}$ .

If the acid/base equilibrium is far to the left, i.e., if the ratio  $K_{\text{a}}/[\text{H}^+]$  equals zero, then only one electron is transferred, and only  $\text{HA}_{\text{ads}}$  is present on the surface. The peak due to conversion of  $\text{HA}_{\text{ads}}$  into  $\text{A}_{\text{ads}}$  is then absent from the voltammogram. The shape of the voltammogram in this case remains similar to the shape of the voltammogram of the anion where both electrons are transferred. This can be seen by taking a closer look at Eqn. 5.2 and 5.3. In the absence of adsorbate-adsorbate interactions, the ratio of the adsorption to the desorption constant conforms to the Nernst equation:

$$k_{\text{ads}}/k_{\text{des}} = \exp\left(\frac{-\gamma eE}{k_{\text{B}}T}\right), \quad (5.15)$$

since  $\alpha_{\text{ads}} + \alpha_{\text{des}} = 1$ . This ratio determines the equilibrium anion coverage on the surface. For a given temperature, this ratio is only dependent on the product of the electroadsorption valency with the voltage,  $\gamma E$ . For a value of  $\gamma$  of -2 (two electrons transferred) adsorption of the anion starts at -0.1 V and is complete at +0.12 V, see Fig. 5.3. If we take  $\gamma$  to be -1 (only one electron transferred), we can immediately see from Eqn. 5.15 that the adsorption process will be smeared out over double the potential range: from -0.2 V to +0.24 V. The change in intensity of the current can be derived by realising that the integral of the current over time is equal to the total charge transferred. By doubling the potential (or equivalently time) range during which adsorption takes place, a reduction of the current with a factor two would be required if the transferred charge remains the same. The total transferred charge is also divided by two, however, since only one instead of two electrons per adsorbate is transferred. This causes a total decrease in intensity of the current by a factor four. The voltammogram for the case where only one electron is transferred is therefore reduced by a factor four in intensity of the current, while at the same time being doubled in potential range with respect to the original model voltammogram depicted in Fig. 5.3.

Summarising, the main effect of the sequential conversion of  $\text{HA}_{\text{ads}}$  into  $\text{A}_{\text{ads}}$  is that the current peak associated with adsorption in a disordered phase becomes flatter and less intense than for the case where both electrons are transferred simultaneously (compare Fig. 5.3 with Fig. 5.11). The disorder-order transition peak retains its intensity.

## 5.4 COMPARISON TO EXPERIMENT

Several factors influence the adsorption behaviour of anions on a metal surface. Below, we will discuss the most important ones for (bi)sulfate. First and most important is the adsorption geometry. Second is the nature of the adsorbate, bisulfate or sulfate, and the amount of electrons that are transferred. Next, the presence of other species, like coadsorbed water, in the adlayer is discussed. Finally we discuss possible causes for effective lateral interactions between adsorbed (bi)sulfate species.

Many (111) surfaces of fcc metals show a  $(\sqrt{3} \times \sqrt{7})$  ordered structure upon adsorption of (bi)sulfate. This strongly suggests that the binding geometry of (bi)sulfate on these surfaces is similar. In the literature, mainly STM and IR have been used to assign the adsorption site of (bi)sulfate. A threefold binding geometry, with three (bi)sulfate oxygens each binding to a metal atom, has long been considered most likely [10,26]. This has also been proposed as the bonding geometry for the  $(\sqrt{3} \times \sqrt{3})$  ordering of (bi)sulfate under UHV conditions [14, 27]. Top adsorption with only one (bi)sulfate oxygen bonding to a metal atom has been proposed by Edens *et al.* [28]. A bridge-bonding geometry, where two of the (bi)sulfate oxygens bind to the metal surface, has also been suggested [11, 14, 29, 30]. Most of the modelling work of (bi)sulfate on fcc(111) surfaces so far has focused on threefold bound (bi)sulfate, with the exception of the work by Orts *et al.* [24] who considered a elongated hard hexagon model which can represent bridge-bonding (bi)sulfate. The modelling studies of threefold bound (bi)sulfate only produced the  $(\sqrt{3} \times \sqrt{7})$  ordered structure when three-particle interactions were introduced [18, 19, 31], in all other cases they produced a  $(\sqrt{3} \times \sqrt{3})$  ordered structure [20–23]. The model with bridge-bound (bi)sulfate on the other hand quite naturally produces the  $(\sqrt{3} \times \sqrt{7})$  structure, without the need of balancing two- and three-particle interactions as shown in the results section and previously by Orts *et al.* [24].

Several studies were devoted to the issue of whether the adsorbed species is bisulfate ( $\text{HSO}_4^-$ ) or sulfate ( $\text{SO}_4^{2-}$ ). Earlier studies pointed either to bisulfate [11, 26] or sulfate [28, 32–35]. More recent studies clearly show the effect of the pH and the electrode potential on the adsorbed species: with higher pH and higher electrode potential, the adsorbed species converts from bisulfate to sulfate [6, 29, 36]. This is also supported by the experimental data in Refs. 26 and 37, though not by the discussion in these references. The electrosorption valency is also known to increase from about -1 to -2 with electrode potential, in agreement with the conversion of bisulfate to sulfate [6, 38]. These more recent measurements have also provided an estimate for the acid constant of adsorbed bisulfate, which is about  $10^{-4}$  [36]. Summarising, the results suggest that at potentials where the  $(\sqrt{3} \times \sqrt{7})$  structure is present, the surface is occupied mainly by sulfate, whereas at lower potentials mainly bisulfate is present. In the rest of this discussion we shall -for matter of convenience- refer in general to the adsorbed species as sulfate, keeping in mind that this species may be either sulfate or bisulfate.

The  $(\sqrt{3} \times \sqrt{7})$  structure as viewed by STM shows additional weak spots in the unit cell. These have been assigned to a second sulfate molecule and coadsorbed

hydronium ions, but are now generally accepted as being coadsorbed water [4, 6, 10, 11, 14, 28, 39, 40]. We have taken the suggestions above, of a bridge-bound anion with an electrosorption valency of -2, into account in our model, and the results compare favourably with the experimental observations.

The voltammograms of sulfate adsorption on well-prepared Pt(111) surfaces [4, 15, 41–43] show a saw-tooth adsorption peak and a sharp disorder-order transition comparable to our voltammograms for the anion adsorption without interactions with the second neighbour shell. The experimental saw-tooth adsorption peak is about 0.2 V wide, and has a maximum intensity of about  $30 \mu\text{A}/\text{cm}^2$ . It is followed by a sharp disorder-order transition peak, typically having a maximum intensity larger than  $75 \mu\text{A}/\text{cm}^2$  (all values for a sweep rate of 50 mV/s). The experimental saw-tooth peak is more flat than the simulated peak. This may be due to a conversion of bisulfate into sulfate, as shown in the section on the sequential transfer of electrons. The simulated width is in good agreement with the experimental one. The intensity of the disorder-order transition in our simulations is smaller than the experimental one. It is determined by the diffusion rate used in our simulations and the time interval used to calculate the current. Larger diffusion rates and smaller time intervals give a sharper disorder-order transition peak. However, larger diffusion rates imply longer simulations. In addition, the voltammogram becomes more noisy with smaller time intervals, since less anions adsorb in a smaller time interval. The diffusion rate constant,  $10^5 \text{ s}^{-1}$ , and the time interval used in the simulated voltammograms, 0.05 s, are therefore a compromise between getting good statistics, limiting simulation time, and getting a sharp disorder-order transition.

Experimentally, the equilibration of the adlayer is believed to be very fast. The peak due to the disorder-order transition is therefore not expected to vary with sweep rate. Our results indicate a dependence of the disorder-order transition on the sweep rate applied. This is due to the choice of the values of the individual rate constants for adsorption, desorption and diffusion. The equilibration in the experimental adlayer may be faster or slower, depending on the values of the real rate constants for adsorption, desorption and diffusion. Bringing the time dependence of such adsorption-desorption and diffusion processes in a simulation in complete correspondence with experiment requires additional study. For a discussion of this problem in the related system of bromine electrosorption on Ag(100), see the papers by Mitchell *et al.* and Abou Hamad *et al.* [44, 45].

The intensity of the disorder-order transition peak is known to decrease with the fraction of steps on the surface. Experimentally, this peak disappears for terrace sizes between 20 and 14 atoms [15, 46]. In our model a phase transition is still seen for terrace sizes down to 16 atoms. A terrace size of 8 atoms does not show a phase transition anymore, and the  $(\sqrt{3} \times \sqrt{7})$  structure is not formed. Note that the presence of the disorder-order transition peak can also be masked by the peak associated with adsorption in a disordered phase, giving slightly different estimates for the lower limits of the terrace size. The simulated adsorption isotherms also agree well with the experimentally measured charge density–voltage ( $\sigma$ – $E$ ) and ion density–voltage ( $\Gamma$ – $E$ ) plots [38, 46]. These three types of plots are similar since a coverage can be related to

an ion density and/or a charge density and vice versa.

Attractive lateral interactions strongly influence the simulated voltammogram for our model. In experimental literature, two cases have been described where effective attractive lateral interactions between the adsorbed sulfate molecules have been deduced. For the adsorption of sulfate on copper, it was seen that the sulfate-metal interaction was so strong that the first metal layer expands, and loses registry with the bulk metal [9]. The sulfate-metal interactions are therefore more geometrically demanding than the metal-metal interactions, that is, deviations from the optimal sulfate bonding geometry drastically reduce the binding energy. Conversely stated, stretching the surface metal layer to optimise the sulfate bonding geometry causes a significant gain in binding energy. Wandelt *et al.* also showed that even at low coverages of sulfate, islands of a  $(\sqrt{3} \times \sqrt{7})$  ordered structure can be formed on Cu(111). Based on these observations they concluded that there is an effective attraction between adsorbed sulfate molecules on Cu(111) [8, 9, 47]. This can be rationalised by realising that if the copper lattice is locally expanded by one sulfate molecule (at a certain energy penalty), a second sulfate molecule binding close to the first will also bind more strongly, without having to expand the lattice by itself. Unfortunately the voltammogram of sulfate adsorption on copper is dominated by slow surface reconstruction, and is therefore not comparable to our results in Fig. 5.8.

On palladium, iridium and rhodium, hydrogen desorption and sulfate adsorption occur at similar potentials, and this also influences the voltammogram peak shapes [27, 37, 39, 40, 48, 49]. The effective sulfate-sulfate interaction in this case is due to the balance between the sulfate-hydrogen, hydrogen-hydrogen and sulfate-sulfate interactions. The voltammograms of all these metals show very sharp adsorption peaks (typically several hundreds  $\mu\text{A}/\text{cm}^2$  high and with a width of less than 0.05 V). A weak disorder-order transition peak is seen for palladium at a potential 0.05 more positive than the adsorption peak. No disorder-order transition peak is reported for iridium and rhodium. In addition, for these metals a large hysteresis (of 0.05-0.1 V) is seen between the sulfate adsorption in the positive going sweep and the sulfate desorption in the negative going sweep. These sharp adsorption peaks indicate effective attractive interactions, even though the individual two-body interactions (hydrogen-hydrogen, sulfate-sulfate, and hydrogen-sulfate) may be repulsive. Sharp and narrow adsorption peaks and a small disorder-order transition peak were also found in our simulations with attractive interactions (Fig. 5.8). A similar hysteresis between the forward and backward going sweep was also found in our simulations (not shown). Repulsive lateral interactions have a much smaller influence on the voltammogram shape (Figure 5.9) than attractive interactions. Finding solid experimental proof of repulsive interactions based on the voltammogram shape only is therefore very difficult.

Gold(111) shows a deconstruction from the  $(23 \times 1)$  structure upon adsorption of sulfate, and this effect is clearly visible in the corresponding voltammogram by the broad adsorption feature [11, 28]. The effect of the deconstruction on the voltammogram cannot be reproduced by our model. The  $(\sqrt{3} \times \sqrt{7})$  ordered structure was also observed for sulfate adsorption on ruthenium, but no peak associated with sulfate adsorption was reported in the corresponding voltammogram [50, 51]. Incommensu-



rate adsorption into a  $c(3 \times 3\sqrt{3})$  structure was observed for sulfate adsorption on silver [33, 52].

The exact nature of the adsorbed adlayer with the coadsorbed water is more complicated than the model of one anion bonding in a bridged fashion presented here. Electronic structure calculations reported so far only considered adsorption on clusters [53–55]. We think that a combined approach of periodic DFT slab calculations with surface relaxation and vibrational spectroscopy may yield more detailed information on the exact nature of the interactions between the sulfate, the water and the metal surface.

## 5.5 CONCLUSIONS

We have studied the adsorption of a bridge-bonded model anion on fcc(111) surfaces. The voltammogram for this model anion displays two peaks: the first peak is a broad one associated with adsorption in a disordered phase, the second peak is sharp and due to a disorder-order phase transition. The disorder-order transition converts the adlayer with a coverage of 0.18 ML into a  $(\sqrt{3} \times \sqrt{7})$  structure with a coverage of 0.20 ML. High sweep rates or defects in the surface do not influence the first peak, but cause a decrease in intensity for the disorder-order transition peak.

Attractive interactions cause an increase in intensity and sharpening of the first peak, and a decrease in intensity of the disorder-order transition peak. The potential range during which an adsorption current is measured becomes smaller with increasing attraction. Repulsive interactions broaden the first peak, reducing its intensity. The shape of the disorder-order transition peak is more or less unaffected by the repulsive interactions. The potential range during which an adsorption current is measured becomes larger with increasing repulsion.

The voltammogram shape is similar for the cases when one or two electrons are transferred upon adsorption. A sequential transfer of the electrons (by an acid/base reaction of the adsorbed species) causes the peak associated with adsorption in a disordered phase to be more flat and less intense, leaving the disorder-order transition unaffected.

This chapter has been accepted for publication in Surface Science as: C. G. M. Hermse, A. P. van Bavel, M. T. M. Koper, J. J. Lukkien, R. A. van Santen and A. P. J. Jansen; Modelling the butterfly:  $(\sqrt{3} \times \sqrt{7})$  ordering on fcc(111) surfaces; 2004.

- [1] D. M. Kolb; An atomistic view of electrochemistry; *Surf. Sci.*, 500: 722–740, 2002.
- [2] J. Clavilier in: A. Wieckowski (Ed.); *Interfacial Electrochemistry, Theory, Experiment and Applications*, page 231; Marcel Dekker, New York, 1999.
- [3] B. M. Ocko, J. X. Wang and T. Wandlowski; Bromide adsorption on Ag(001): a potential induced two-dimensional Ising order-disorder transition; *Phys. Rev. Lett.*, 79(8): 1511–1514, 1997.
- [4] A. M. Funtikov, U. Stimming and R. Vogel; Anion adsorption from sulfuric acid solutions on Pt(111) single crystal electrodes; *J. Electroanal. Chem.*, 428: 147–153, 1997.
- [5] O. M. Magnussen; Ordered anion adlayers on metal electrode surfaces; *Chem. Rev.*, 102: 679–725, 2002.
- [6] A. Kolics and A. Wieckowski; Adsorption of bisulfate and sulfate anions on a Pt(111) electrode; *J. Phys. Chem. B*, 105: 2588–2595, 2001.
- [7] P. Zelenay, G. Horanyi, C. K. Rhee and A. Wieckowski; Voltammetric and radioactive labeling studies of single crystal and polycrystalline rhodium electrodes in sulfate-containing electrolytes; *J. Electroanal. Chem.*, 300: 499–519, 1991.
- [8] M. Wilms, P. Broekmann, C. Stuhlmann and K. Wandelt; In-situ STM investigation of adsorbate structures on Cu(111) in sulfuric acid electrolyte; *Surf. Sci.*, 416: 121–140, 1998.
- [9] P. Broekmann, M. Wilms, A. Spaenig and K. Wandelt; Morphological aspects of sulfate-induced reconstruction of Cu(111) in sulfuric acid solution: in situ STM study; *Progr. Surf. Sci.*, 67: 59–77, 2001.
- [10] K. Ataka and M. Osawa; In situ infrared study of water-sulfate coadsorption on gold(111) in sulfuric acid solutions; *Langmuir*, 14: 951–959, 1998.
- [11] O.M. Magnussen, J. Hagebock, J. Hotlos and R.J. Behm; In situ scanning tunneling microscopy observations of a disorder-order phase transition in hydrogensulfate adlayers on Au(111); *Faraday Discussions*, 94: 329–338, 1992.
- [12] K. Sashikata, Y. Matsui, K. Itaya and M. P. Soriaga; Adsorbed iodine catalyzed dissolution of Pd single crystal electrodes: studies by electrochemical STM; *J. Phys. Chem.*, 100: 20027–20034, 1996.
- [13] I. Oda, Y. Singaya, H. Matsumoto and M. Ito; UPD mechanisms of copper and thallium on a Pt(111) electrode studied by in-situ IRAS and EC-STM; *J. Electroanal. Chem.*, 409: 95–101, 1996.
- [14] Y. Shingaya, H. Matsumoto, H. Ogasawara and M. Ito; In situ and ex situ IRAS, LEED and EC-STM studies of underpotentially deposited copper on a Pt(111) electrode in sulfuric acid solution: coadsorption of sulfate ion with copper; *Surf. Sci.*, 335: 23–31, 1995.
- [15] M. T. M. Koper, J. J. Lukkien, N. P. Lebedeva, J. M. Feliu and R. A. van Santen; Adsorbate interactions and phase transitions at the stepped platinum/electrolyte interface: experiment compared with Monte Carlo simulations; *Surf. Sci.*, 478: L339–L344, 2001.
- [16] M. T. M. Koper and J. J. Lukkien; Modeling the butterfly: influence of lateral interactions and adsorption geometry on the voltammetry at (111) and (100) electrodes; *Surf. Sci.*, 498: 105–115, 2002.
- [17] M. T. M. Koper and J. J. Lukkien; Modeling the butterfly: the voltammetry of ( $\sqrt{3} \times \sqrt{3}$ )R30° and p(2x2) overlayers on (111) electrodes; *J. Electroanal. Chem.*, 485: 161–165, 2000.
- [18] P. A. Rikvold, H. Gamboa-Aldeco, J. Zhang, M. Han, Q. Wang, H. L. Richards and A. Wieckowski; Computational lattice-gas modelling of the electroadsorption of small molecules and ions; *Surf. Sci.*, 335: 389–400, 1995.

- [19] P. A. Rikvold, J. Zhang, Y.-E. Sung and A. Wieckowski; Lattice-gas models of adsorption in the double layer; *Electrochimica Acta*, 41(14): 2175–2184, 1996.
- [20] M. Legault, L. Blum and D. A. Huckaby; An extended hexagon model for Cu underpotential deposition on Au(111); *J. Electroanal. Chem.*, 409: 79–86, 1996.
- [21] L. Blum and D. A. Huckaby; Phase transitions at liquid-solid interfaces: Pade approximant for adsorption isotherms and voltammograms; *J. Chem. Phys.*, 94(10): 6887–6894, 1991.
- [22] L. Blum, D. A. Huckaby and M. Legault; Phase transitions at electrode interfaces; *Electrochim. Acta*, 41(14): 2207–2227, 1996.
- [23] D. A. Huckaby and L. Blum; Exact results for the adsorption of a dense fluid onto a triangular lattice of sticky sites; *J. Chem. Phys.*, 92(4): 2646–2649, 1990.
- [24] J. M. Orts, L. Blum, D. Huckaby, J. M. Feliu and A. Aldaz; Modeling of 2D water-sulfate coadsorption on well-defined Me(111) electrodes; *Abstr. Pap. Am. Chem. Soc.*, 220: 91, 2000.
- [25] R. J. Baxter; *Exactly solved models in statistical mechanics*; Academic Press, 1982.
- [26] Y. Shingaya and M. Ito; Comparison of a bisulfate anion adsorbed on M(111) (M= Pt, Rh, Au, Ag and Cu); *J. Electroanal. Chem.*, 467: 299–306, 1999.
- [27] Y.-E. Sung, S. Thomas and A. Wieckowski; Characterisation of the Rh(111) electrode by CEELS, AES, LEED, and voltammetry. Adsorption of (bi)sulfate, perchlorate, and carbon monoxide; *J. Phys. Chem.*, 99: 13513–13521, 1995.
- [28] G. J. Edens, X. Gao and M. J. Weaver; The adsorption of sulfate on gold (111) in acidic aqueous media: adlayer structural inferences from infrared spectroscopy and scanning tunneling microscopy; *J. Electroanal. Chem.*, 375: 357–366, 1994.
- [29] F. C. Nart and T. Iwasita; An FTIR study of adsorbed sulfate species on polycrystalline platinum with application of group theory to the problem of band assignment for adsorbed species; *J. Electroanal. Chem.*, 322: 289–300, 1992.
- [30] M. Arenz, P. Broekmann, M. Lennartz, E. Vogler and K. Wandelt; In-situ characterisation of metal/electrolyte interfaces: sulfate adsorption on Cu(111); *Phys. Stat. Sol. (a)*, 187(1): 63–74, 2001.
- [31] J. Zhang, Y.-E. Sung, P. A. Rikvold and A. Wieckowski; Underpotential deposition of Cu on Au(111) in sulfate-containing electrolytes: a theoretical and experimental study; *J. Chem. Phys.*, 104(14): 5699–5712, 1996.
- [32] Z. Shi and J. Lipkowski; Investigations of sulfate adsorption at the Au(111) electrode by chronocoulometry and radiochemistry; *J. Electroanal. Chem.*, 366: 317–326, 1994.
- [33] N. S. Marinkovic, J. S. Marinkovic and R. R. Adzic; In situ infrared spectroscopic investigations of sulfate adsorption at the Ag(111) electrode surface; *J. Electroanal. Chem.*, 467: 291–298, 1999.
- [34] G. Lang, A. Aramata and G. Horanyi; Some remarks on a method suggested for the distinction between  $\text{SO}_4^{2-}$  and  $\text{HSO}_4^-$  ions adsorbed on an electrode; *J. Electroanal. Chem.*, 504: 225–229, 2001.
- [35] J. Lipkowski and A. Wieckowski; Using thermodynamic analysis of charge density data for a solution of  $\text{K}_2\text{SO}_4$  in  $\text{HClO}_4$ , one can determine whether the species predominantly adsorbed at an Au(111) electrode is  $\text{HSO}_4^-$  or  $\text{SO}_4^{2-}$ ; *J. Electroanal. Chem.*, 504: 230–234, 2001.
- [36] A. Lachenwitzer, N. Li and J. Lipkowski; Determination of the acid dissociation constant for bisulfate adsorbed at the Pt(111) electrode by subtractively normalized interfacial Fourier transform infrared spectroscopy; *J. Electroanal. Chem.*, 532: 85–98, 2002.

- [37] T. Senna, N. Ikemiya and M. Ito; In situ IRAS and STM of adsorbate structures on an Ir(111) electrode in sulfuric acid electrolyte; *J. Electroanal. Chem.*, 511: 115–121, 2001.
- [38] E. Herrero, J. Mostany, J. M. Feliu and J. Lipkowski; Thermodynamic studies at the Pt(111) electrode surface in sulfuric acid solutions; *J. Electroanal. Chem.*, 534: 79–89, 2002.
- [39] L.-J. Wan, S.-L. Yau and K. Itaya; Atomic structure of adsorbed sulfate on Rh(111) in sulfuric acid solution; *J. Phys. Chem.*, 99: 9507–9513, 1995.
- [40] L.-J. Wan, M. Hara, J. Inukai and K. Itaya; In situ STM of well-defined Ir(111) surface: high resolution imaging of adsorbed sulfate; *J. Phys. Chem. B*, 103: 6978–6983, 1999.
- [41] N. P. Lebedeva, M. T. M. Koper, J. M. Feliu and R.A. van Santen; The effect of the cooling atmosphere in the preparation of flame-annealed Pt(111) electrodes on CO adlayer oxidation; *Electrochem. Commun.*, 2: 487–490, 2000.
- [42] L. A. Kibler, A. Cuesta, M. Kleinert and D. M. Kolb; In-situ STM characterisation of the surface morphology of platinum single crystal electrodes as a function of their preparation; *J. Electroanal. Chem.*, 484: 73–82, 2000.
- [43] J. M. Feliu, J. M. Orts, R. Gomez, A. Aldaz and J. Clavilier; New information on the unusual adsorption states of Pt(111) in sulphuric acid solutions from potentiostatic adsorbate replacement by CO; *J. Electroanal. Chem.*, 372: 265–268, 1994.
- [44] S. J. Mitchell, G. Brown and P. A. Rikvold; Static and dynamic Monte Carlo simulations of Br electrodeposition on Ag(100); *Surf. Sci.*, 471: 125–142, 2001.
- [45] I. Abou Hamad, P. A. Rikvold and G. Brown; Determination of the basic timescale in kinetic Monte Carlo simulations by comparison with cyclic-voltammetry experiments; submitted to *Surf. Sci. Lett.*, 2004.
- [46] J. Mostany, E. Herrero, J. M. Feliu and J. Lipkowski; Thermodynamic studies of anion adsorption at stepped platinum(hkl) electrode surfaces in sulfuric acid solutions; *J. Phys. Chem. B*, 106: 12787–12796, 2002.
- [47] M. Lennartz, P. Broekmann, M. Arenz, C. Stuhlmann and K. Wandelt; Sulfate adsorption on Cu(111) studied by in-situ IRRAS and STM; revealing the adsorption site and desorption behaviour; *Surf. Sci.*, 442: 215–222, 1999.
- [48] N. Hoshi, M. Kuroda, O. Koga and Y. Hori; IRAS of the sulfuric acid anion on low and high index planes of palladium; *J. Phys. Chem. B*, 106: 9107–9113, 2002.
- [49] L.-J. Wan, T. Suzuki, K. Sashikata, J. Okada, J. Inukai and K. Itaya; In situ scanning tunneling microscopy of adsorbed sulfate on well-defined Pd(111) in sulfuric acid solution; *J. Electroanal. Chem.*, 484: 189–193, 2000.
- [50] P. C. Lu, C. H. Yang, S. L. Yau and M. S. Zei; In situ STM of (bi)sulfate, oxygen, and iodine adlayers on a well-defined Ru(001) electrode prepared in a non-ultrahigh-vacuum environment; *Langmuir*, 18: 754–762, 2002.
- [51] N. S. Marinkovic, J. X. Wang, H. Zajonz and R. R. Adzic; Adsorption of bisulfate on the Ru(0001) single crystal electrode surface; *J. Electroanal. Chem.*, 500: 388–394, 2001.
- [52] M. Schweizer and D. M. Kolb; First observation of an ordered sulfate adlayer on Ag single crystal electrodes; *Surf. Sci.*, 544: 93–102, 2003.
- [53] M. D. Legault and D. E. Babelo; Theoretical study of the adsorption of bisulfate on small gold clusters; *J. Phys. Chem. A*, 106: 9059–9064, 2002.
- [54] E. M. Patrito, P. P. Olivera and H. Sellers; On the nature of sulfate/Ag(111) and sulfate/Au(111) surface bonding; *Surf. Sci.*, 380: 264–282, 1997.
- [55] P. P. Olivera, E. M. Patrito and H. Sellers; Adsorption of sulfate, bisulfate and sulfuric acid on silver surfaces: a theoretical study; *Surf. Sci.*, 418: 376–394, 1998.

110 REFERENCES

## CHAPTER 6

# LATERAL INTERACTIONS AND MULTI-ISOTHERMS

Lateral adsorbate-adsorbate interactions cause desorption rate constants to vary with coverage. This effect can be studied in great detail from the shape of a multi-isotherm. To produce the multi-isotherm, the temperature is increased in a (semi)stepwise fashion to some temperature, followed by maintaining the temperature constant at this temperature for a prolonged time. After this time the temperature is stepped to a higher value, and held constant at this new temperature. This cycle is continued until all the adsorbates have desorbed. Using a detailed kinetic Monte Carlo model and an Evolutionary Strategy based optimisation algorithm we are able to reproduce the shape of the experimentally measured multi-isotherm of nitrogen on Rh(111) [1]. Kinetic parameters deconvoluted from lateral effects are extracted from the experiments.

### 6.1 INTRODUCTION

A common technique to study surface reactions is temperature-programmed desorption (TPD), where the temperature of a surface is linearly increased with time. As a consequence, the adsorbed species will desorb, causing a peak with a maximum at a certain typical temperature and with a certain typical width. From these results one can derive kinetic data. It is difficult to relate the resulting TPD to elementary rate constants since both the coverage of the reactant and the desorption rate constant are varied simultaneously during the TPD. It is also often not clear whether the desorption peak is associated with one or several processes. Many techniques have nevertheless been described in literature to extract pre-exponential factors and activation energies from TPD traces [2–5]. These even include estimations of coverage-dependent ac-

tivation energies. To deduce the lateral interactions present in the adlayer from the coverage-dependent activation energies requires a detailed model, however.

If the temperature is increased in a step-wise fashion, followed by a plateau of constant temperature, then on this plateau the rate constants do not change, only the coverage does. The kinetics measured on these plateaus are isothermal, and we therefore refer to the set of isothermal plateaus separated by temperature steps as “multi-isotherms” [6]. This kind of experiment would for a simple first order desorption reaction yield only one sharp desorption peak with an exponential decay at one of the plateaus. For a second order desorption also only one desorption peak is expected. Surprisingly, experiments of this type for atomic nitrogen on Rh(111) [1] and CO on Rh(100) [7] show multiple desorption peaks, indicating desorption processes with different rate constants. The fact that these rate constants are dependent on the coverage implies the presence of lateral adsorbate-adsorbate interactions (or adsorbates bound to different sites). These lateral interactions are now clearly visible within one experiment, whereas in a conventional TPD many experiments have to be done to clearly discern their effect. Since these lateral interactions are clearly visible from the multi-isotherm, they serve as an excellent starting point for trying to model the effect of adlayer interactions on the desorption rate.

In this work we discuss the experimentally reported multi-isotherm by Zaera *et al.* [1], and explain its shape in terms of lateral interactions. We compare this multi-isotherm to a simulated multi-isotherm for a simple recombinative desorption model without lateral interactions, and show that there is a significant difference between the two. We then introduce an improved model with lateral interactions. To get the correct values for the lateral interactions we use a fitting procedure based on an Evolutionary Strategy optimisation procedure. This assures efficient exploration of the parameter space, and also reduces the risk of getting stuck in a local minimum. The kinetic parameters obtained in this way yield a better description of the experimental multi-isotherm, and the kinetic parameters are physically more reasonable than for the model without interactions.

## 6.2 MODEL

### 6.2.1 MODEL IMPLEMENTATION

Our model consists of a lattice of fcc and hcp sites. These two sites form a regular honeycomb grid (Figure 6.1) with the length of each side of the hexagon equal to  $1/\sqrt{3}$  lattice vectors, and the sides of the hexagons ( $\mathbf{c}_1$ ,  $\mathbf{c}_2$  and  $\mathbf{c}_3$ ) at a 30 degree angle with the lattice vectors ( $\mathbf{a}_1$  and  $\mathbf{a}_2$ ) of the (111) surface. Every site is labelled f or h according to its type, with a prefix to indicate the type of adsorbate: N or \* (the last stands for a vacant site).

Based on the results from previous DFT-calculations [8], we have excluded the sites nearest to an adsorbate from occupation (at distance  $|\mathbf{c}|$ , see Figure 6.1). Four other kinds of lateral interactions  $\varphi(i)$  have been taken into account:  $\varphi_2$ , at the second neighbour site (one lattice vector,  $|\mathbf{a}|$  apart),  $\varphi_3$ , at the third neighbour site ( $2/\sqrt{3}$

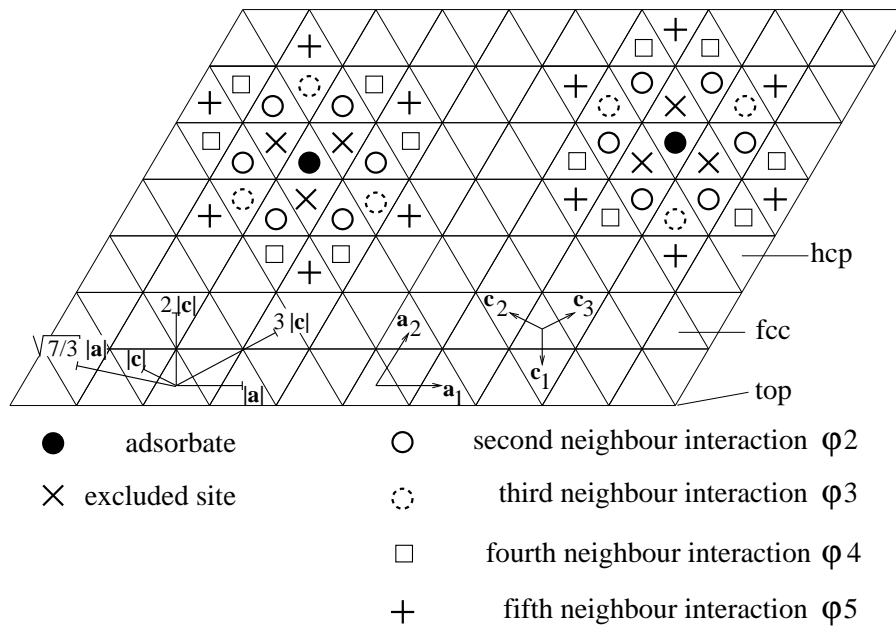


Figure 6.1: Excluded sites and lateral interactions  $\varphi(i)$  around an adsorbate in the two-site model.



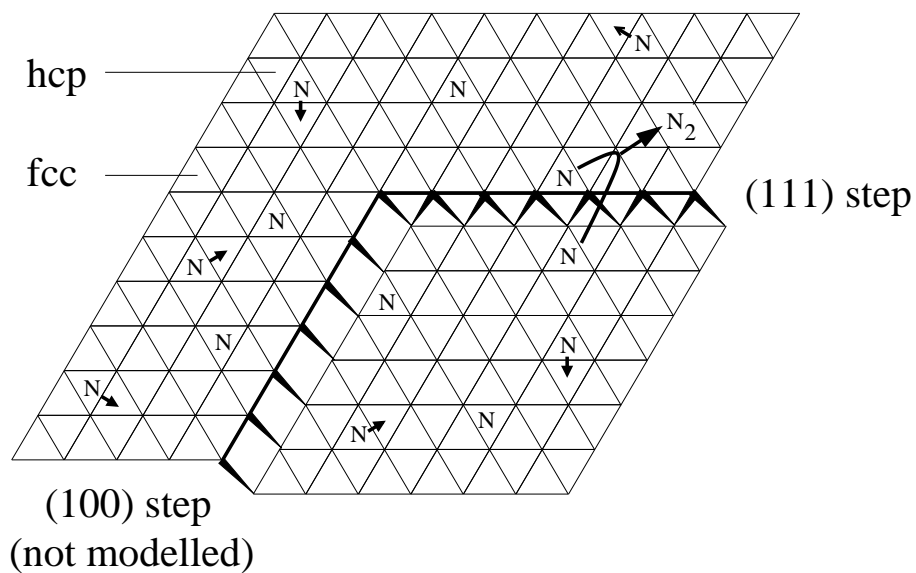
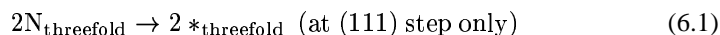


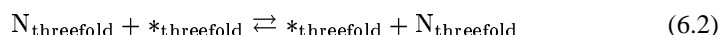
Figure 6.2: Our kinetic Monte Carlo model: nitrogen atoms occupy the threefold sites on the Rh(111) surface, and are allowed to diffuse around. They recombine at the (111) steps in the surface.

lattice vector or  $2|\mathbf{c}|$  apart),  $\varphi_4$ , at the fourth neighbour site ( $\sqrt{7/3}$  lattice vector apart), and last  $\varphi_5$  at the fifth neighbour site ( $\sqrt{3}$  lattice vector or  $3|\mathbf{c}|$  apart).

We have included recombinative desorption of  $\text{N}_2$  at the (111) steps (see also Figure 6.2):



and diffusion of N:



The rate constant for desorption is modified by the lateral interactions:

$$k_{\text{rec}} = \nu \times \exp\left(-\frac{E_{\text{act}}^0 + \alpha\delta E}{RT}\right), \quad (6.3)$$

where  $\nu$  and  $E_{\text{act}}^0$  are the Arrhenius parameters at zero coverage,  $\alpha$  is the Brønsted-Evans-Polanyi coefficient for recombinative desorption, and  $\delta E$  equals the change in reaction energy due to lateral interactions.

The kinetic parameters we have used are listed in Table 6.1. For simplicity we have treated the threefold sites as equivalent in our kMC model, though a difference in binding energy of typically 10 kJ/mol has been observed between fcc and hcp sites [8]. A similar difference in binding energy is expected between step and terrace sites, but these were also for simplicity treated as equivalent. Diffusion was not modelled with Arrhenius-type rate constants for the TPD/TPR simulations because such diffusion increases with several decades over the simulated temperature range. Instead, rate constants for diffusion were taken sufficiently large (in practice they were set to  $1000 \text{ s}^{-1}$ , modified by the lateral interactions), such that detailed balance was satisfied. Tests with various prefactors have shown that the reduction of nitrogen diffusion only slightly lowers the rate of nitrogen formation. So our modelling of the diffusion yields an adlayer at equilibrium without too much computer time spent on diffusion. Note that no diffusion of nitrogen was allowed across the steps in the surface. The grid size used was  $256 \times 128$  with two subsites per unit cell for the TPD/TPR simulations. The two subsites per unit cell represent the fcc and hcp site for each surface atom. The step density was  $1/29$ , i.e., the surface consists of 29 atom wide terraces ending in a (111) type step. The step density of  $1/29$  is the one expected for a crystal with a miss-cut of  $2^\circ$ . The surface can also be defined using the Miller index as a Rh(29 29 27) surface.

Lateral interactions across the step are not taken into account; only adsorbates on the same side of the step edge (de-)stabilise each other. This was realised by separating the 29 grid lines representing one terrace, from the next terrace by three empty grid lines representing the step. The periodicity in terms of our simulation grid was therefore  $29+3=32$ , while the simulated terrace size was, as mentioned before, 29. All coverages in this chapter are expressed as the number of adsorbates per number of terrace atoms.

In view of the difference in energy between reactant and product we have taken diffusion to be a middle transition state ( $\alpha = 0.5$ ), and we have taken the Brønsted-

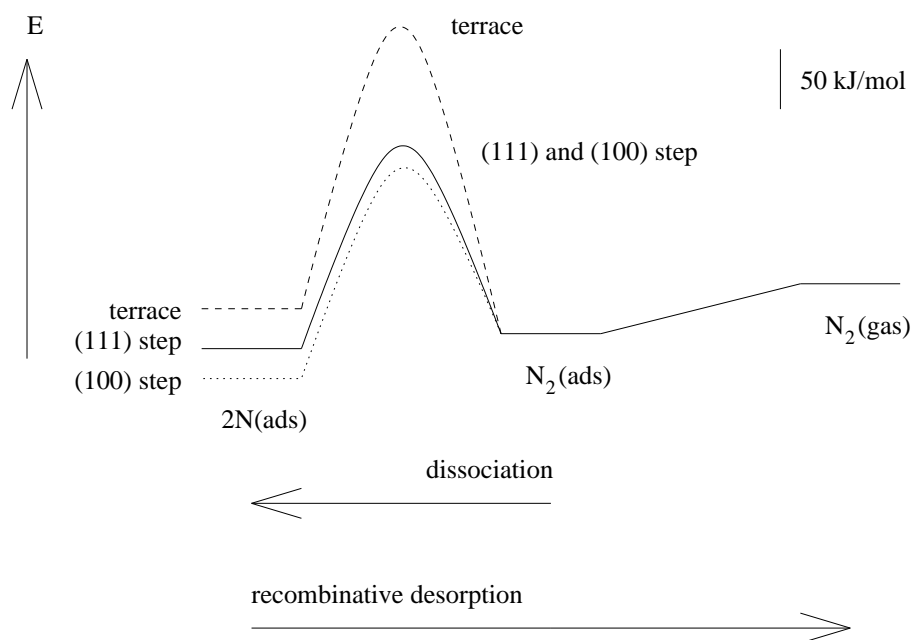


Figure 6.3: Schematic energy diagram for recombinative desorption of nitrogen from Rh(111). The activation energy for the recombination reaction is larger than for the desorption reaction, and is therefore rate determining. The activation energy of the recombination reaction at the steps is lower than the activation energy on the terrace due to a different transition state geometry. The activation energy for the (111) step is expected to be lower than for the (100) step since the (100) step binds adsorbates more strongly. The reverse of the recombination reaction is the dissociation of adsorbed dinitrogen into nitrogen atoms.

Evans-Polanyi coefficient for recombinative desorption to be 0.2, based on the extensive data set on step-mediated reactions presented in Ref. 9. For the Evolutionary Strategy simulations a reduced diffusion rate of  $100 \text{ s}^{-1}$  modified by lateral interactions was used, combined with a smaller grid of  $128 \times 64$ .

### 6.2.2 MODEL CHOICE

The recombinative desorption of nitrogen from fcc(111) surfaces has been studied using numerous techniques. Some of those are able to distinguish between terrace and step site reactivity. Below we will summarise the most important experimental results connected to our model. As shown in Fig. 6.3, the recombinative desorption of nitrogen is a two-step process. First, two nitrogen atoms on the surface recombine to form an adsorbed nitrogen molecule. The weakly adsorbed nitrogen molecule then

desorbs rapidly into the gas phase. The recombination step is rate determining in this process, since it has the highest activation energy. The activation energy of the recombination reaction is known to depend on the type of site where the reaction takes place: the reaction at step sites is different from the reaction on the terrace. The activation energy for the recombination reaction is much higher at the terrace than at the steps. This is especially striking since the binding energies of the reactants and products of the reaction (nitrogen atoms and adsorbed dinitrogen) vary less strongly. The reason why the activation energy for the terrace reaction is much higher is that the transition state geometry for the recombination reaction at the terrace is very different from the transition state geometry at the steps. Due to this difference in geometry the transition state is better stabilised at the steps than at the terrace. This is the reason for the large difference in the activation energy between terrace and steps. Finally, please note that the energy levels for adsorbed dinitrogen on both steps and terrace have been drawn at equal height. This is an approximation, since in practice it has been shown that the dinitrogen binding energy varies with the surface geometry [10].

Studies on Rh(533), or Rh 4(111)×(100), using angular resolved thermal desorption mass spectrometry [11], indicated that nitrogen desorbs from the steps in the surface. A similar study for Rh(111) at much higher temperatures reported two desorption peaks, one sharp around zero degrees, and one broad at around thirty degrees to the surface normal [12]. The temperature of 700–1000 K used in this study is considerably larger than the normal nitrogen desorption temperature of nitrogen on Rh(111), 450–650 K. This presence of two channels at higher temperatures might be compared to the case of nitrogen desorption from Ru(001) [13]. In this case poisoning of the steps resulted in an up-shift of 200 K of the nitrogen desorption peak, strongly indicating the role of the steps in the recombination. The authors were unable to assert whether the desorption peak at higher temperatures was due to reaction at the terrace, or by reaction at some unpoisoned parts of the steps. DFT calculations of the same authors on the Ru(001) surface also indicated that the (100) steps can effectively dissociate nitrogen. The dissociation reaction on the terrace had a much higher activation barrier. Since the dissociation reaction is the reverse of the recombinative desorption, one expects these steps to be active in the recombination reaction as well. The (111) step was not discussed in this study. A prerequisite for recombinative desorption at defects in the surface is that diffusion across the terrace to those defects is fast. This is also the case for ruthenium, even though the activation barrier for diffusion of nitrogen on ruthenium is relatively large. For nitrogen on rhodium, the activation barrier for diffusion is much smaller [14], and diffusion to the active site should therefore pose no problem.

When comparing the reactivity of the (111) step with the (100) step, two things will play a role. First of all, the activity, and second, the rate of deactivation (poisoning) during the reaction. Calculations of the dissociation of the NO molecule on stepped ruthenium surfaces indicate that both the (111) and the (100) step are well able to dissociate NO [15, 16]. Since NO and nitrogen are similar diatomics with strong internal bonds, one would also expect nitrogen to dissociate (or recombine) well on both types of steps. Studies of NO dissociation on stepped rhodium surfaces also support

the idea that both (111) and (100) steps are able to dissociate NO [17–19]. From the intrinsic reactivity point of view, it is therefore likely that nitrogen recombination can take place at both (100) and (111) steps in the surface. A principle feature of (100) steps is that they bind adsorbates more strongly than (111) steps. This is because (100) steps are more open than (111) steps. A stronger bond with the adsorbate is favourable for the dissociation reaction, but *unfavourable* for the recombinative desorption.

The preparation of nitrogen adlayers usually involves adsorption of NO, after which the oxygen is removed by reaction with carbon monoxide or hydrogen [20–22]. Alternatively, a beam of activated nitrogen can be directed at the surface. One can also allow ammonia to decompose on the surface under evolution of hydrogen. The main method, however, involves dissociation of NO on the surface, after which the oxygen is removed. This oxygen is known to poison the (100) steps, but not the (111) steps, on Ru(001) [23]. A similar poisoning of the (100) steps was seen on Rh(533) [11]. The presence of trace amounts of oxygen in a nitrogen adlayer is very difficult to avoid because of the preparation procedure. These traces of oxygen will preferentially bind to defects and steps, because of the stronger binding strength.

Based on these observations we think that at low temperatures (450–650 K) the nitrogen recombination reaction on Rh(111) mainly proceeds through a reaction at the steps. At higher temperatures (>700 K) a second direct reaction on the terrace may also be possible. The (111) step appears to be intrinsically more active in the recombination reaction than the (100) step, based on its lesser binding strength. Based on the same difference in binding strength it is also less likely to get poisoned during the preparation of the nitrogen adlayer. This explains our model choice. To the best of our knowledge there has been only one report on a surface reconstruction of Rh(111) induced by nitrogen atoms. A (2x1) reconstruction was suggested for local nitrogen coverages of 0.5 ML or higher and in the joint presence of oxygen [24].

Please note that the reaction mechanism proposed here is different from the one proposed in Ref. 1. In this reference desorption from the perimeter of nitrogen islands was proposed, the reaction at steps was deemed less likely. With respect to this other mechanism we would like to note that the nitrogen island formation proposed by the authors still awaits experimental confirmation. The desorption product in  $^{14}\text{N}/^{15}\text{N}$  isotope exchange experiments mainly consists of  $^{14}\text{N}^{15}\text{N}$ . This is cited by the authors to support the hypothesis of nitrogen desorption from the perimeter of the nitrogen islands. This observation can also be explained by the step mediated desorption mechanism. From electronic structure calculations and STM images [15, 23] it is clear that the nitrogen atom formed in the dissociation reaction of NO is preferentially deposited at the bottom of the step, while the oxygen atom is deposited on top of the step. If  $^{14}\text{N}$  is already present on the terrace and a small amount of  $^{15}\text{NO}$  is dissociated on the step, then close to the bottom of the step there will be mainly  $^{15}\text{N}$ , while at the top of the step there will be mainly  $^{14}\text{N}$  (if the oxygen is somehow removed). The dinitrogen species formed by recombinative desorption at the step will therefore mainly consist of  $^{14}\text{N}^{15}\text{N}$ , as was also observed experimentally. The supposed limited mobility of the nitrogen atoms quoted by the authors of Ref. 1 is not very realistic since both STM and electronic structure calculations have indicated a low diffusion

barrier for nitrogen [8, 14].

### 6.3 OPTIMISATION TECHNIQUES

Optimisation in high-dimensional systems is notoriously difficult, especially when a noisy stochastic method is used. We have therefore followed the following optimisation procedure. First, an Evolutionary Strategy method was used to efficiently explore phase space. Next, the optima found in this procedure were refined with a Simplex optimisation. The advantage of the Evolutionary Strategy is that it is well able to avoid local optima (which are many in multidimensional parameter space) in search for a global optimum, thanks to the mutations and crossovers during the process. Also, it is able to deal with noisy responses, which is necessary since the kinetic Monte Carlo simulations are stochastic. The Simplex optimisation is very useful to refine the optimum.

#### 6.3.1 EVOLUTIONARY STRATEGY OPTIMISATION

The Evolutionary Strategy (ES) we have used [25, 26] works with a set of chromosomes  $x_i$ . Each chromosome  $x_i$  encodes a set of  $n$  kinetic parameters (listed in Table 6.1, these are sometimes referred to as genes) to be optimised; it can therefore be seen as a vector of size  $n$  with each element storing a possible value of a kinetic parameter. Each chromosome  $x_i$  has a counterpart  $\sigma_i$  which stores for each of the kinetic parameters how fast they change during the optimisation procedure. All chromosomes together ( $i = 1, 2, \dots, \mu$ , where  $\mu$  is the total number of chromosomes) form a population.

To optimise the fitness  $F$  in the simulation (and thus getting better parameters), we generate  $\lambda$  new chromosomes by modifying the  $\mu$  old chromosomes. The modification process involves crossover and mutation. The new chromosomes are evaluated by doing a simulation, and graded accordingly. Next, we retain only the  $\mu$  best chromosomes of the offspring, and generate  $\lambda$  new chromosomes from them.

The crossover process is characterised by the fact that information of two chromosomes is combined to make a new chromosome: the values of the kinetic parameters they encode are averaged to form a new chromosome. This kind of crossover, where the values of the genes are averaged, is referred to as intermediate crossover. In the case of mutation, a single parent chromosome is taken, and the value of one kinetic parameter it encodes is randomly changed. The size of the mutation changes during the optimisation; early in the optimisation large changes are preferred to cover large areas of parameter space, but later on the changes need to be more subtle in order not to lose sight of the minimum found. This is what the  $\sigma_i$  vectors are used for: during the mutation step the kinetic parameter in  $x_i$  is changed by an amount proportional to the value for that parameter in  $\sigma_i$ . To be exact, the amount is equal to a random number drawn from a normal Gaussian distribution with width specified by the appropriate value in  $\sigma_i$ . Crossover and mutation are also applied to the  $\sigma_i$  vectors. Selection causes these vectors to be large at the beginning of an optimisation run, and small near

convergence. For details on the reason for this see Refs. 25 and 26. Typical values for during our optimisations include 50 generations of each  $\lambda = 128$  chromosomes, each encoding the  $n = 2 - 6$  parameters listed in Table 6.1. Half of the chromosomes is discarded after each step, from the other  $\mu = 64$  a new generation is created. Chromosomes from the parent generation are not allowed to pass on to the offspring unchanged.

### 6.3.2 SIMPLEX OPTIMISATION

An ordinary Simplex optimisation was used for refining the optima found. It had a Spendley style convergence criterion and start simplex [27, 28]; the reflection was determined using the Weight Centroid Method according to Ryan [29]. The choice for a Simplex optimisation was motivated by its easy and straight-forward implementation.

### 6.3.3 DEFINITION OF THE FITNESS

For the optimisation an error in the simulation results has to be defined, which can then be minimised. We have looked at different error definitions  $\chi$ :

$$\chi_{\text{sq}} = \frac{1}{N} \sum_{t=\Delta t}^{N\Delta t} (p(t)_{\text{exp}} - p(t)_{\text{sim}})^2 \quad (6.4)$$

$$\chi_{\text{abs}} = \frac{1}{N} \sum_{t=\Delta t}^{N\Delta t} |p(t)_{\text{exp}} - p(t)_{\text{sim}}| \quad (6.5)$$

$$\chi_{\text{rel}} = \frac{2}{N} \sum_{t=\Delta t}^{N\Delta t} \frac{|p(t)_{\text{exp}} - p(t)_{\text{sim}}|}{p(t)_{\text{exp}} + p(t)_{\text{sim}} + \varepsilon} \quad (6.6)$$

where  $\chi$  is the mean squared, absolute or fractional error in  $p(t)$ , the time dependent observable. The observable was chosen to be either the coverage of nitrogen or the desorption rate.  $\varepsilon$  (a small number) was introduced into the last formula to prevent near-zero values of the observable from completely dominating the value of the error. It functions as a cut-off for the case that the absolute value of the observable is small, and equal to the difference between the experimental and simulated value.

The observable  $p(t)$  was determined at  $N = 70$  time intervals during the experiment, and each measurement was compared to the simulated values at the corresponding simulated times. The sum is over the different times  $t = j \Delta t$ , with  $j = 1, 2, \dots, N$  and  $\Delta t = 5$  s.

The choice of the fitness criterium in the Evolutionary Strategy is quite important. In our case, the fitness only reflects the difference between experiment and simulation. The standard mean squared error value emphasises the largest outliers when comparing two traces. The other two error definitions, which are based on the absolute difference and the relative difference, are less dominated by the largest outliers. We considered these for a particular reason. The desorption trace we try to model

Table 6.1: Definition and domain of the kinetic parameter set used.

Parameter	Range	Unit	Description
x	-16 – 0	-	$\ln(k_{\text{Arrh}}) = \ln(\nu) - E_{\text{act}}/RT$
y	23 – 100	-	$\ln(\nu) + E_{\text{act}}/RT$
$\alpha$	0.2	-	BEP coefficient <sup>a</sup>
$\varphi_2$	-5 – +30	kJ/mol	second neighbour int.
$\varphi_3$	-5 – +30	kJ/mol	third neighbour int.
$\varphi_4$	-5 – +15	kJ/mol	fourth neighbour int.
$\varphi_5$	-5 – +15	kJ/mol	fifth neighbour int.

<sup>a</sup>Based on the values provided in Ref. 9

has five sharp desorption peaks, followed by plateaus where the desorption rate goes almost to zero again. Both features are important to reproduce in our model. By using absolute-difference or relative-difference based error values we were able to direct the algorithm search more on reproducing the drop in the desorption rate than on the sharp initial desorption spikes.

We circumvented the problem of reproducing the desorption spikes and the drop in the desorption rate simultaneously by not looking at the desorption rate, but at the coverage of nitrogen still left on the surface. The coverage of nitrogen as a function of time indicates what fraction has reacted. The difference in coverage between successive measuring points stores the average desorption rate in that interval. The previous definition based on the desorption rate only does not look at the history of the adlayer: a desorption peak is a desorption peak, independent of what fraction of the nitrogen has reacted so far. A coverage-based fitness value is therefore better (more specific) than a desorption-based fitness value, since aside from the momentary desorption rate it also contains information on the overall progress of the desorption process. The fitness function  $F$  used to optimise our parameter set was therefore chosen to be based on the mean squared error in the coverage

$$F = \chi_{\text{sq}}(\theta) = \frac{1}{N} \sum_{t=\Delta t}^{N\Delta t} (\theta(t)_{\text{exp}} - \theta(t)_{\text{sim}})^2. \quad (6.7)$$

The experimental coverages were calculated from the experimental desorption trace using the experimentally determined coverage at the beginning of the experiment.

## 6.4 THE MULTI-ISOTHERM

### 6.4.1 ANALYSIS OF THE MULTI-ISOTHERM

The solid line in Figure 6.4 shows a multi-isotherm for the model without lateral interactions, but with nitrogen recombination at the steps and an Arrhenius-type recombination rate constant. For low temperatures, the recombination rate is negligible



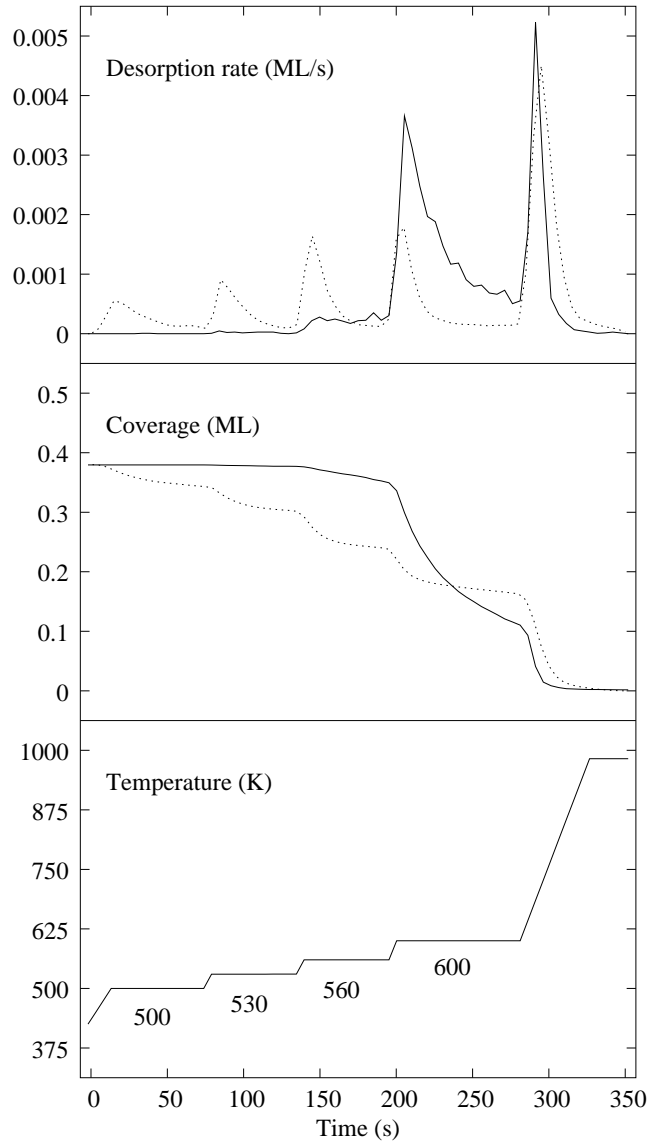


Figure 6.4: Multi-isothermal desorption trace (top) and atomic nitrogen coverage (middle) for the desorption of  $N_2$  from a Rh(111) surface. Experiment (dotted line) compared to a model with an Arrhenius type recombination rate constant and no adsorbate-adsorbate interactions (solid line). The surface was sequentially heated to 500, 530, 560, 600 and 1000 K (bottom). The initial coverage of atomic nitrogen was 0.38 ML. Experimental data from Ref. 1, mapped onto  $N + 1 = 71$  points.

and the coverage of nitrogen remains close to the starting coverage. When the temperature is stepped to a higher value, at some point the recombination rate becomes significant, and a small, almost constant desorption rate is seen in the desorption trace. The coverage decreases linearly with time. If the temperature is stepped once again, the recombination rate constant increases sharply, and the remaining nitrogen on the surface is quickly consumed. This results in a sharp decay in the coverage of nitrogen and also a sharp decay in the desorption rate. The only reason why the desorption rate decreases in this interval is that there is no nitrogen left over to desorb. The recombination reaction rate constant remains constant during the entire interval. Finally, if the temperature is stepped once more before all nitrogen has reacted, the remaining nitrogen leaves the surface, also in a sharp peak. Note that between the previous-to-last and last constant temperature plateau, the desorption rate does not go to zero. Since there is nitrogen left to desorb, the rate has a significant value. It is only after all nitrogen has reacted that the desorption rate becomes zero.

When we now look at the experimental trace (dotted line in Fig. 6.4), we see that at each temperature plateau we get a desorption peak, but this peak quickly decreases to zero. When the temperature is raised again we get another desorption peak, and this peak again decays quickly. This continues until there is no nitrogen left to react. Since at each of the constant temperature plateaus the coverage of nitrogen is larger than zero, the drop to zero of the desorption rate must be caused by a change in the recombination rate constant. The trace appears as a superposition of many simple temperature-step desorption traces, each with its own recombination rate constant. Since there remains an appreciable amount of nitrogen present on the surface, the desorption rate decreases by a change of the recombination rate constant.

The trace can be understood on the basis of the presence of significant lateral interactions. At high coverages, the nitrogen atoms repel each other strongly. This causes an increase in the recombination rate constant. So if we go to the first constant temperature plateau, nitrogen will start desorbing because of the strongly repulsive interactions. As a consequence of the desorption process, the coverage starts decreasing, and the nitrogen atoms can redistribute to avoid some of the repulsive interactions. This causes a decrease in the recombination rate constant, and the desorption rate drops close to zero. If we then increase the temperature again, the recombination rate constant increases. More nitrogen desorbs, and the repulsion between the nitrogen atoms further decreases. This causes again a reduction of the recombination rate constant, and the desorption rate again decreases to close to zero, even though there is still a lot of nitrogen left on the surface. This cycle is repeated until the repulsions between the nitrogen atoms become negligible (i.e., the coverage becomes low) and the effective recombination rate constant becomes approximately equal to the recombination rate constant without repulsive interactions. In this case the desorption rate will not drop until the coverage becomes zero. The multi-isotherm desorption trace can now be seen as a consecutive stripping of parts of the adlayer.

The decay of the desorption peak is then strictly speaking not single component

Table 6.2: Mean squared error in the coverage and optimised kinetic parameters as defined in Table 6.1 for models with different number of lateral interactions. The activation energy and lateral interactions are in kJ/mol, the prefactor in  $s^{-1}$ . The mean squared value of the experimental data is 0.064.

parameters	$\chi_{sq}(\theta)$	$E_{act}$	$\log \nu$	$\varphi 2$	$\varphi 3$	$\varphi 4$	$\varphi 5$
x, y	0.003	220	20.0	-	-	-	-
x, y, $\varphi 2$	$\leq 0.001$	60	4.8	21	-	-	-
x, y, $\varphi 2, \varphi 3$	$\leq 0.001$	165	14.7	20	17	-	-
x, y, $\varphi 2, \varphi 3, \varphi 4$	$\leq 0.001$	158	14.1	26	18	7	-
x, y, $\varphi 2, \varphi 3, \varphi 4, \varphi 5$	$\leq 0.001$	156	13.5	22	15	6	5

but bi- or multi-component

$$\frac{d\theta_{total}}{dt} \approx -k'(\theta')^2 - k''(\theta'')^2 - \dots \quad (6.8)$$

where  $\theta'$  is the coverage of nitrogen atoms that experience lateral interactions, giving rise to an increased effective recombinative desorption constant  $k'$ , and  $\theta''$  is the coverage of nitrogen “feeling” fewer lateral interactions, giving rise to a smaller recombinative desorption constant  $k''$ . Since  $k'' \ll k'$ , the individual components are separated into different desorption peaks.

#### 6.4.2 MODEL WITHOUT INTERACTIONS

The calculation presented in the beginning of Section 6.4.1 was a model with the best fitness found for the case without lateral interactions. The values for the activation energy, the pre-exponential factor and the mean squared error for this model are listed in Table 6.2. This table also summarises the results for the more elaborate model with lateral interactions. The pre-exponential factor and the activation energy for the recombinative desorption model without interactions are unusually large. Typical values reported in literature based on TPD analysis are  $10^{10.5} s^{-1}$  and 120 kJ/mol [20–22]. These parameters are well able to reproduce a conventional TPD, but result in a premature desorption compared to experiment when performing a multi-isotherm (Figure 6.5). The much higher values obtained by our optimisation cause the desorption trace to match the experimental one better. It is important to realise here that while the conventionally reported values of 120 kJ/mol and  $10^{10.5} s^{-1}$  do reproduce the normal TPD, they do not at all properly reproduce the multi-isotherm, and are therefore just as unrealistic as the values reported in Table 6.2 for the model without interactions.

#### 6.4.3 MODELS WITH INTERACTIONS

The models with lateral interactions show a better fit to the experiment than the model without interactions. The first question one should ask is how many interactions would

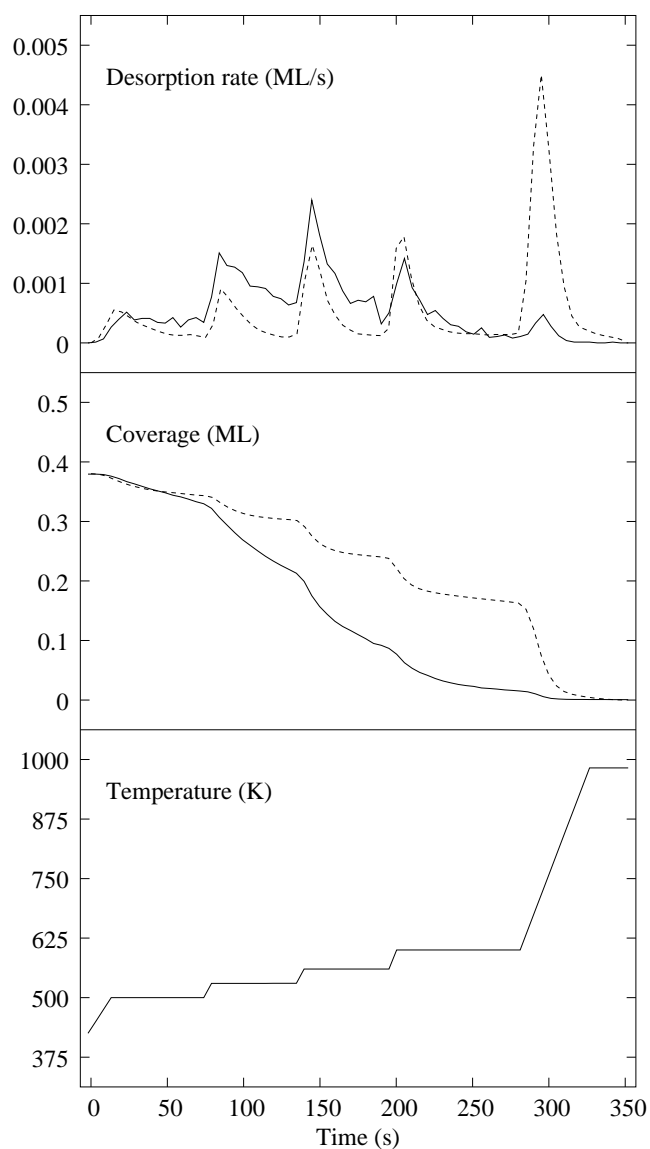


Figure 6.5: Multi-isothermal desorption trace (top) and atomic nitrogen coverage (middle) for the desorption of  $N_2$  from a Rh(111) surface. Experiment (dotted line, from Ref. 1) compared to a model with an Arrhenius type recombination rate constant using the literature values of the activation energy (120 kJ/mol) and the prefactor corrected for the amount of steps ( $30 \times 10^{10.5} \text{ s}^{-1}$ ) (solid line). No adsorbate-adsorbate interactions were taken into account. The surface was sequentially heated to 500, 530, 560, 600 and 1000 K (bottom). The initial coverage of atomic nitrogen was 0.38 ML.

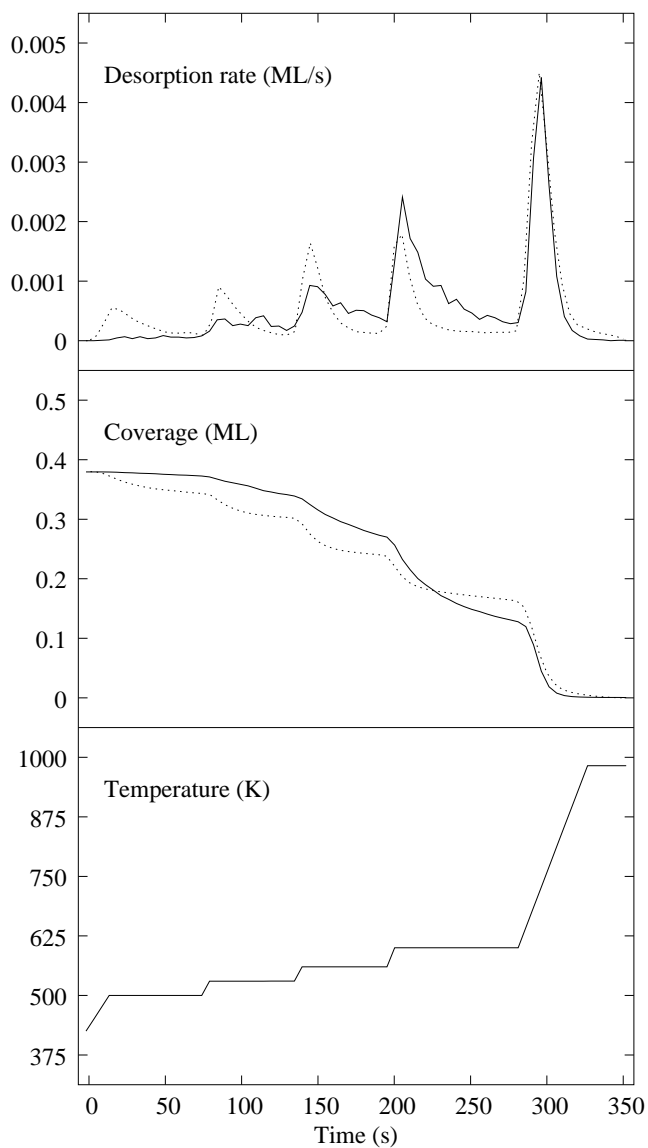


Figure 6.6: Multi-isothermal desorption trace (top) and atomic nitrogen coverage (middle) for the desorption of  $N_2$  from a Rh(111) surface. Experiment (dotted line, from Ref. 1) compared to a model with an Arrhenius type recombination rate constant and four adsorbate-adsorbate interactions  $\varphi_2$ ,  $\varphi_3$ ,  $\varphi_4$  and  $\varphi_5$  (solid line). The surface was sequentially heated to 500, 530, 560, 600 and 1000 K (bottom). The initial coverage of atomic nitrogen was 0.38 ML.

be needed to reproduce the experimental isotherm: can we do with less? The answer to this question is given by the experimental isotherm. Upon heating to 600 K, there is a desorption peak which again decreases to zero, indicating that at the beginning of the temperature plateau there were still interactions present in the adlayer. These have been removed at the end of the 600 K plateau. The coverage at the end of the plateau is 0.18 ML, so we know that for coverages larger than 0.18 ML there are interactions present in the adlayer. The longest-range interaction in our four-interaction model is over  $\sqrt{3}$  substrate lattice vectors, the next one spanning two substrate lattice vectors. So for coverages lower than 0.25 ML we do not expect to have interactions in our simulated adlayer, provided that it is well equilibrated. In other words, for coverages below 0.25 ML, we expect our system to behave like the model without interactions, and the decrease to zero of the desorption rates during the temperature plateaus is not expected to happen. We will therefore not be able to describe properly the right part of the multi-isotherm trace. The interesting range is therefore the low-temperature, high-coverage part of the multi-isotherm.

The models with one to four interactions all give a very reasonable fit to the experiment, as seen from the  $\chi_{\text{sq}}(\theta)$  value in Table 6.2. The model with only one interaction has an unreasonably small value for the prefactor, and the estimate should therefore be disregarded. The model fits with two to four interactions consistently yield activation energies between 155 and 165 kJ/mol, and a prefactor between  $10^{13}$  and  $10^{15} \text{ s}^{-1}$ . The lateral interactions are significant (15–25 kJ/mol) at close range, in agreement with previous DFT calculations, which yielded values of 40 and 22 kJ/mol respectively [8]. At longer range the interactions are, as expected, smaller (5–10 kJ/mol) and they tend to go to zero with increasing distance. The decay to zero of the interactions at a distance close to two lattice vector compares well to the experimentally measured decay of the interactions between nitrogen atoms on Ru(001) [30]. The range of values for the activation energy of 155–165 kJ/mol agrees well with the DFT estimate of 155 kJ/mol [9]. Since we know that experimentally lateral interactions are present for coverages down to 0.18 ML, we will discuss below our results for the model with four interactions.

#### 6.4.4 MODEL WITH FOUR INTERACTIONS

The low-temperature, high-coverage part of the multi-isotherm fit for four interactions shows some similarities to the experimental isotherm (Figure 6.6). The problem here is that the fitness we defined judges the entire multi-isotherm (including the part we can not reproduce), and not specifically on the first part, which we might expect to reproduce better. The best traces we obtain are therefore a balance between getting the first part right, and reducing the lack of fit in the second part. Nevertheless, we do want to point out some features in these traces (Fig. 6.6). First of all, the first desorption peak (at 500 K) in the simulated multi-isotherm is missing. This first desorption peak, associated with close-range interactions, is expected to be present in our simulation as well. It is not found however. This may be due to a different (slightly higher) starting coverage in the experiment. If we increase the starting coverage in our simulations to

a value slightly higher than 0.38 ML, we can also reproduce the first desorption peak at 500 K (see the dotted line in Figure 6.7).

For the temperature plateau at 530 K, we see a distinct desorption peak, which is nearly constant in time. When the temperature is jumped to 560 K, the desorption rate increases, and then decays to some smaller non-zero value. These two peaks together are due to lateral interactions in the adlayer, and the decay in the peak at 560 K indicates that some of the interactions in the adlayer are removed by desorbing nitrogen. The decay in the peak at 560 K is not nearly as sharp as the experimental decay, however. For the temperature plateau at 600 K and the heating to 1000 K we see an ordinary recombinative desorption without lateral interactions present. Overall, the coverage as a function of time follows the experiment much better than for the more simple model depicted in Fig. 6.4.

As for the values for the kinetic parameters fitted from the experiment (Table 6.2), the activation energy and pre-exponential factor are very high in the absence of lateral interactions. With the inclusion of lateral interactions they get more reasonable values. The differences between the simulated multi-isotherm can be due to deficiencies in the model, but also due to the uncertainty in the experimental starting coverage ( $\pm 0.05$  ML) and a slight overshoot in the temperature program when stepping to the next plateau (5–10 K). Though there is a considerable lack of fit between our model and the experiment, we do want to show some implications of the model thus formulated.

The fact that the different peaks in the multi-isotherm are caused by nitrogen atoms experiencing lateral interactions can also be shown by repeating the multi-isotherm for different starting coverages. In this case, for lower coverages one expects the first desorption peaks (due to interactions) to become less intensive, while the other peaks (due to less or non perturbed nitrogen) remain the same. This is exactly what is shown in Figure 6.7 where the onset of desorption is shifted to higher temperatures for lower coverages.

The model including the interactions fitted for the multi-isotherm also properly describes the ordinary temperature programmed desorption trace with a constant heating rate. We therefore show the results for three different starting coverages of nitrogen for our model with all four interactions (Figure 6.8) and the model without any interactions (Figure 6.9). The experimentally observed substantial shift to lower temperatures of the desorption peak with higher coverages [1, 20–22] is much better reproduced by the model with the interactions than by the model without the interactions. This observation has also been made by the groups of Zhdanov and Weinberg when they modelled nitrogen desorption from Rh(111) [31, 32]. These models were respectively a mean field and a single lateral interaction Monte Carlo model. The approximate temperature range for the desorption is also comparable to the experimental one.

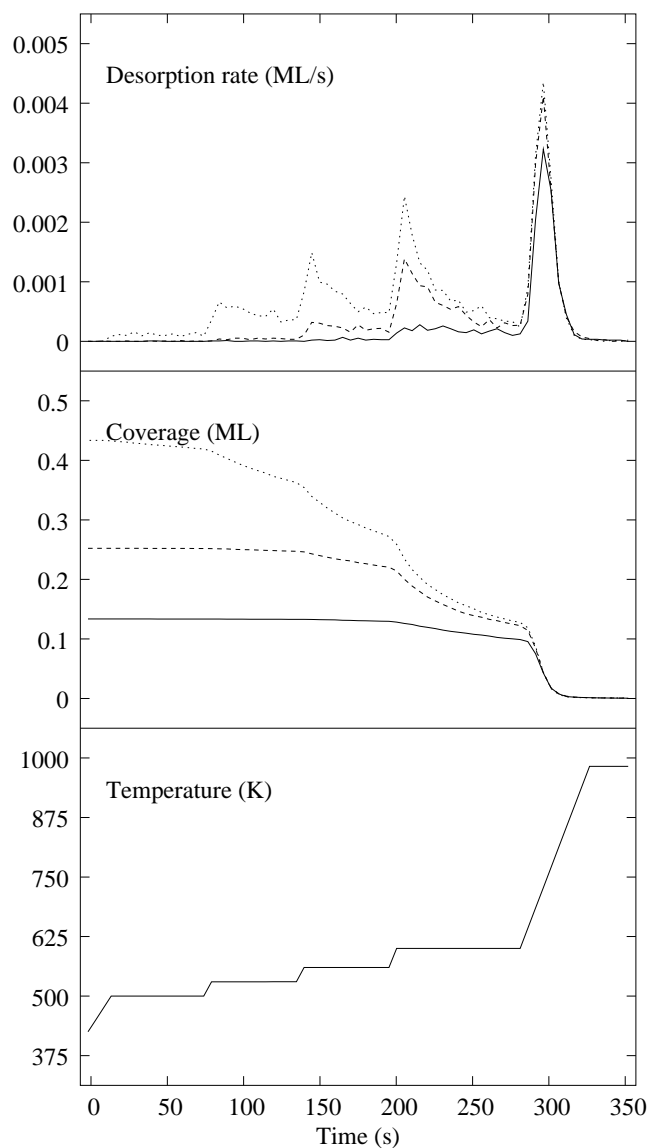


Figure 6.7: Multi-isothermal desorption trace (top) and atomic nitrogen coverage (middle) for the desorption of  $N_2$  from a Rh(111) surface. Model with an Arrhenius type recombination rate constant and four adsorbate-adsorbate interactions  $\varphi_2$ ,  $\varphi_3$ ,  $\varphi_4$  and  $\varphi_5$ . Different starting coverages of 0.13 ML (solid line), 0.26 ML (dashed line) and 0.43 ML (dotted line) were used. The surface was sequentially heated to 500, 530, 560, 600 and 1000 K (bottom).



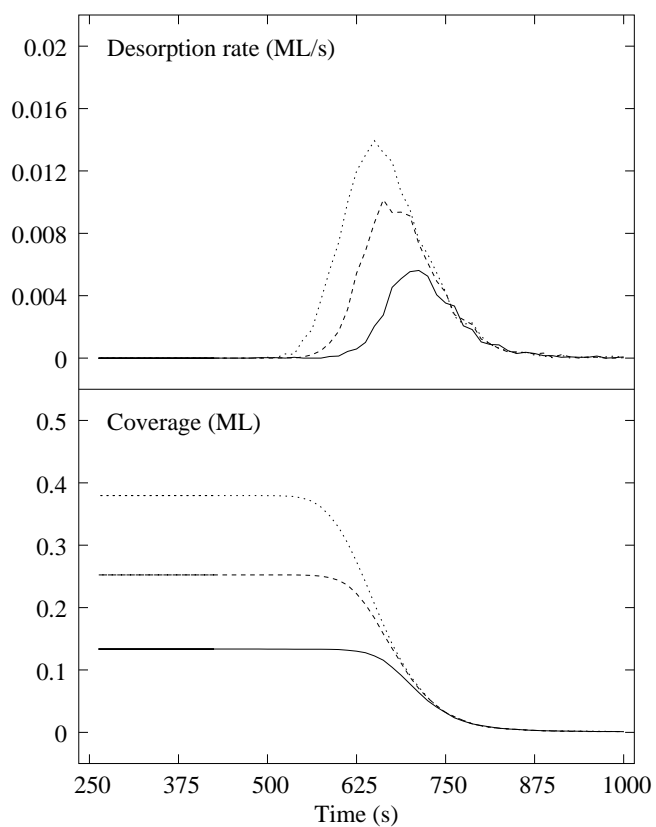


Figure 6.8: Simulated temperature programmed desorption traces for the model with four interactions, for three different starting coverages: 0.13 ML (solid line), 0.26 ML (dashed line) and 0.38 ML (dotted line). The heating rate was 10 K/s.

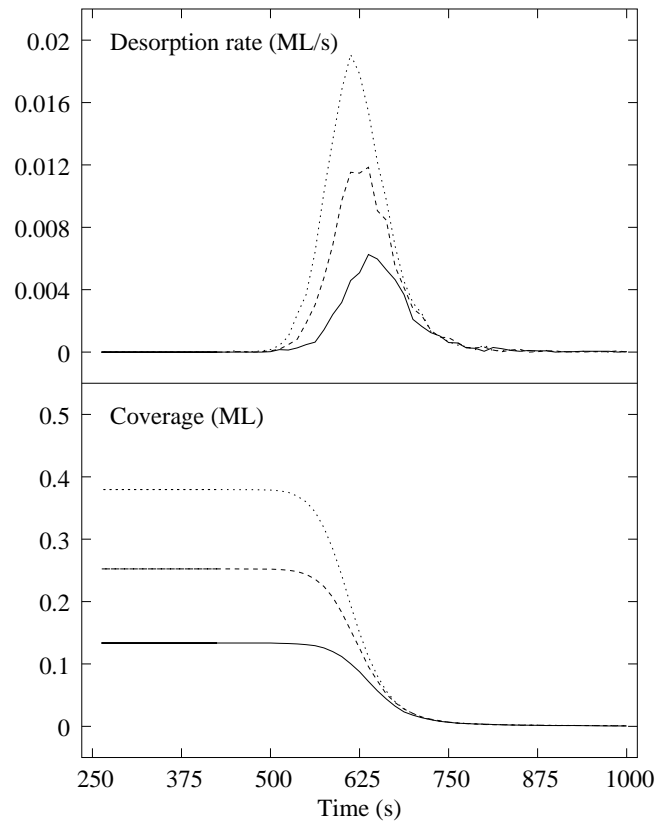


Figure 6.9: Simulated temperature programmed desorption traces for a model with an Arrhenius type recombination rate constant using the literature values of the activation energy (120 kJ/mol) and the prefactor corrected for the amount of steps ( $30 \times 10^{10.5} \text{ s}^{-1}$ ), for three different starting coverages: 0.13 ML (solid line), 0.26 ML (dashed line) and 0.38 ML (dotted line). No adsorbate-adsorbate interactions were taken into account. The heating rate was 10 K/s.

## 6.5 DISCUSSION

### 6.5.1 OTHER FACTORS THAT INFLUENCE DESORPTION

The recombinative desorption of nitrogen is influenced by many factors. We have attributed the shape of the multi-isotherm to lateral interactions solely. Below we discuss some additional factors, which do not explain the multi-isotherm shape.

A slow diffusion of nitrogen to the active (step) sites on the surface will cause a tailing in the desorption rate in the isothermal plateaus. This tailing is expected to be of the form of  $1/\sqrt{t}$ . The tailing observed in the multi-isotherm on the other hand shows a stronger decay. Also, when stepping the temperature to the next plateau, the diffusion rate is expected to increase, and the reaction is expected to be less diffusion limited. Based on these two arguments we can therefore conclude that the shape of the multi-isotherm is not caused by a diffusion limitation.

In our model we have assumed that the nitrogen recombines at the (111) step. If the nitrogen reacts instead at the (100) step, the reaction mechanism remains largely the same: the nitrogen has to diffuse to the step, and may react there under the influence of lateral interactions. The distribution of nearest neighbour sites is slightly different for the (111) step than for the (100) step, since in one case the reaction takes place between two fcc bound nitrogens, while in the other case one nitrogen is bound fcc and the other one hcp.

A different step density than the one we used will only affect the pre-exponential factor found. The “real” pre-exponential factor can be found by the following relation

$$\nu_{\text{real}} = \frac{f_{\text{model}}}{f_{\text{real}}} \nu_{\text{model}} \quad (6.9)$$

where  $f_{\text{model}}$  and  $f_{\text{real}}$  are the simulated and real step densities respectively. A different step density alone will not explain the shape of the multi-isotherm. The choice for a  $2^\circ$  miss-cut or a step density  $1/29$  was motivated by the desire to keep the diffusion length in our simulations reasonable, thus reducing simulation time. The actual miss-cut reported for the experiment was  $0.1^\circ$ , which is very low. The defect density of this crystal may be larger than this value due to crystal wear and tear.

In order to reproduce the multi-isotherm it is not necessary to assume desorption at the steps. A similar multi-isotherm can be generated by assuming desorption from the terrace (but with lateral interactions included!). The choice to model the desorption reaction at the steps is fully based on the strong indications in literature that it in fact takes place there. The resulting kinetic parameters obtained by modelling the desorption on the terraces will be similar except for the pre-exponential factor, which can be related to the pre-exponential factor for the step reaction if the diffusion of nitrogen is fast:

$$\nu_{\text{terrace}} = \nu_{\text{step}} f \quad (6.10)$$

where  $f$  is the fraction of step sites.

Recombinative desorption through a combination of the (100) step, the (111) step and the terrace is a possibility. In this case the total desorption rate is the sum of

the individual desorption rates connected to the basin of nitrogen on the terrace. This combined desorption process does not provide an explanation for the experimentally observed decay in desorption rate in the isothermal plateaus and can therefore be excluded.

A higher or lower bonding energy for nitrogen bound at the top or bottom of the steps will cause (non)preferential bonding at these sites. The influence on kinetics is that the probability of finding a nitrogen atom at one of these sites differs from the average probability of finding a nitrogen atom somewhere on the terrace. This effect results in a change in the effective pre-exponential factor derived from the experiment, but does not further influence the kinetics (or explain the multi-isotherm shape).

Since the lateral interactions are surface-mediated, they may well change across the surface. The interactions influencing the desorption rates are those at the steps. Little or no information can be derived on the interactions at the terrace, but by similarity to the step interactions we have taken them to be identical. The case of different interactions on the terrace and close to the steps is similar to the case of (non)preferential bonding to the steps in that it results in a different effective pre-exponential factor due to a non-isotropical chance of finding a nitrogen atom at a particular site on the surface.

A difference in binding energy has been observed for nitrogen bound to fcc and hcp sites. This will effectively cause one of the two to be preferred over the other one. Just as for the case of (non)preferential bonding to the steps, and differing interactions on the terrace and close to the steps, this will not greatly influence the kinetics.

Strongly bound nitrogen (at defects) is expected to desorb in a separate peak. This peak should be visible by, instead of ramping the temperature from 600 to 1000 K, using additional temperature plateaus. In this way it may be possible to discern defect-bound nitrogen, and maybe even to get a quantitative estimate of the amount of defects on a surface [7].

One could propose that the decrease in reaction rate on the isothermal plateaus is due to some poisoning process. This would involve blocking of the active step sites. The problem associated with this explanation is that after a temperature step the activity increases again, and then drops again. This then could be explained in two ways. (1) The poison is removed by the temperature step, and the activity is restored. Next, the step is poisoned anew. This does not seem very likely. (2) The poison is not removed by the temperature step, and the subsequent activity drop is due to a further poisoning of the active sites. This would imply that after four isothermal plateaus over 99.9% of the active sites would be poisoned. This explanation is therefore also not very likely.

For nitrogen on Rh(111) it is well-known that only the threefold hollow sites are occupied [33]. It is therefore not expected that the different peaks in the multi-isotherm are due to differently bonded nitrogen atoms, i.e., that for example one is due to top-bound nitrogen, the next due to bridge-bound nitrogen, and another one due to threefold-bound nitrogen. Although in this multi-isotherm we do not expect the shape to be influenced by occupation of different sites, for other molecules this may well be the case. For example, for NO on Rh(111), the top bound NO molecules

are known to be bound less strongly than the threefold bound NO molecules [8]. This would almost certainly cause two separate peaks in the multi-isotherm.

### 6.5.2 OTHER ISSUES

The advantage of using a multi-isotherm is that it contains more information than a conventional TPD. The disadvantage is that the values for the different kinetic parameters can not be extracted directly from the experimental trace. This is due to the fact that the simple models that are assumed to get these values from the TPDs are not valid for the more difficult case discussed here. The quality of the obtained parameters highly depends on the quality of data it is based on, and the quality of the model it is fitted to. In this work we have taken experimental data which are more suited than ordinary TPD traces, and fitted it to a more realistic model. The fitting process then yields parameters which look reasonable, but one has to keep in mind that many approximations were made (see previous section) in building the model. For an unequivocal determination of the kinetic parameters a critical comparison of these values to the ones obtained by other (experimental and theoretical) methods is essential.

Finally, it is interesting to note a similarity to electrochemistry. In the electrochemical equivalent of a temperature-programmed desorption trace, called linear sweep voltammetry, the potential is linearly increased, yielding a current which is due to reactions on the surface studied. A different technique referred to as potential-step experiments involves a change in the potential to some value, where it is kept until the current decreases to zero. After this the potential may be stepped to a higher potential. In electrochemistry it has long been accepted that the potential-step experiments (which are equivalent to our multi-isotherms) yield much more information on the kinetics of the surface reactions than the linear sweep voltammetry.

## 6.6 CONCLUSIONS

We have analysed the shape of an experimentally measured desorption experiment of nitrogen on Rh(111) with a particular temperature programmed desorption protocol, referred to as multi-isotherm. In this temperature program, the temperature is increased in a (semi)stepwise fashion to some temperature, followed by maintaining the temperature constant at this temperature for a prolonged time, after which the temperature is stepped to the next value. We attribute the shape of the experimental isotherm to the presence of lateral interactions between the nitrogen atoms on the surface. We have shown that the presence of these lateral interactions in the adlayer is very well discernible from these so-called multi-isotherms, much more so than for ordinary TPDs.

A similar multi-isotherm shape as observed experimentally can be generated using a Monte Carlo model by assuming that the recombination reaction takes place under influence of lateral interactions. The values of the kinetic parameters in this model (i.e., the pre-exponential factor, activation energy and lateral interactions) were fitted using an Evolutionary Strategy type optimisation algorithm, and are physically

reasonable. Since the lateral interactions in the experiment range up to three substrate lattice vectors, the experimental multi-isotherm was not fully reproduced by our model (which includes lateral interactions ranging up to two substrate lattice vectors). The kinetic parameter set fitted for the multi-isotherm reproduces a standard temperature-programmed desorption experiment with a constant heating rate. Though in principle values for kinetic parameters may be extracted by detailed modelling of an experimentally measured multi-isotherm, it is strongly recommended to verify these model dependent values using different independent techniques. Finally, it is worth noticing that a text-book standard reaction like recombinative desorption of nitrogen can still pose a significant challenge to modellers, when confronted with information-rich experimental data like multi-isotherms.

- [1] F. Zaera and C. S. Gopinath; Effect of coverage and temperature on the kinetics of nitrogen desorption from Rh(111) surfaces; *J. Chem. Phys.*, 116(3): 1128–1136, 2002.
- [2] C. M. Chan, R. Aris and W. H. Weinberg; An analysis of thermal desorption mass spectra.I.; *Appl. Surf. Sci.*, 1: 360–376, 1978.
- [3] A. M. de Jong and J. W. Niemantsverdriet; Thermal desorption analysis: comparative test of ten commonly applied procedures; *Surf. Sci.*, 233: 355–365, 1990.
- [4] A. M. de Jong and J. W. Niemantsverdriet; Comparative test of procedures for thermal desorption analysis; *Vacuum*, 41(1–3): 232–233, 1990.
- [5] D. L. S. Nieskens, A. P. van Bavel and J. W. Niemantsverdriet; The analysis of temperature-programmed desorption experiments of systems with lateral interactions; implications of the compensation effect; *Surf. Sci.*, 546: 159–169, 2003.
- [6] The term multi-isotherm was coined by A. P. van Bavel, Eindhoven University of Technology.
- [7] A. P. van Bavel; Work in progress; 2003–2004.
- [8] C. G. M. Hermse, F. Frechard, A. P. van Bavel, J. J. Lukkien, J. W. Niemantsverdriet, R. A. van Santen and A. P. J. Jansen; Combining density-functional calculations with kinetic models: NO/Rh(111); *J. Chem. Phys.*, 118(15): 7081–7089, 2003.
- [9] J. K. Nørskov, T. Bligaard, A. Logadottir, S. Bahn, L. B. Hansen, M. Bollinger, H. Bengaard, B. Hammer, Z. Sljivancanin, M. Mavrikakis, Y. Xu, S. Dahl and C. J. H. Jacobsen; Universality in heterogeneous catalysis; *J. Catal.*, 209: 275–278, 2002.
- [10] H. A. C. M. Hendrickx, A. Hoek and B. E. Nieuwenhuys; Influence of the surface structure on the adsorption of nitrogen on rhodium; comparison with Pt, Ir, Pd and Ni; *Surf. Sci.*, 135: 81–92, 1983.
- [11] M. Ikai, N. M. H. Janssen, B. E. Nieuwenhuys and K. Tanaka; Spatial distribution of N<sub>2</sub> and NO desorbing from a Rh(533) surface; *J. Chem. Phys.*, 106(1): 311–320, 1997.
- [12] J. I. Colonell, K. D. Gibson and S. J. Sibener; Dynamics of NO reduction by H<sub>2</sub> on Rh(111): Velocity and angular distribution of the N<sub>2</sub> product; *J. Chem. Phys.*, 104(17): 6822–6833, 1996.
- [13] S. Dahl, A. Logadottir, R. C. Egeberg, J. H. Larsen and I. Chorkendorf; Role of steps in N<sub>2</sub> activation on Ru(0001); *Phys. Rev. Lett.*, 83(9): 1814–1817, 1999.
- [14] H. Xu and K. Y. S. Ng; Direct observation of competitive adsorption of NO, O and N on Rh(111) surface by scanning tunneling microscopy; *Appl. Phys. Lett.*, 68(4): 496–498, 1996.
- [15] B. Hammer; Adsorption, diffusion and dissociation of NO, N and O on flat and stepped Ru(001); *Surf. Sci.*, 459: 323–348, 2000.
- [16] B. Hammer; Bond activation at monatomic steps: NO dissociation at corrugated Ru(0001); *Phys. Rev. Lett.*, 83(18): 3681–3684, 1999.
- [17] F. Esch, A. Baraldi, C. Comelli, S. Lizzit, M. Kiskinova, P. D. Cobden and B. E. Nieuwenhuys; Atomic nitrogen on steps: A fast x-ray photoelectron spectroscopy study of the NO uptake on Rh(533), Rh(311) and Rh(111); *J. Chem. Phys.*, 110(8): 4013–4019, 1999.
- [18] N. M. H. Janssen, A. R. Cholach, M. Ikai, K. Tanaka and B. E. Nieuwenhuys; The interaction of NO with stepped Rh surfaces; *Surf. Sci.*, 382: 201–213, 1997.
- [19] L. A. DeLouise and N. Winograd; Adsorption and desorption of NO from Rh(111) and Rh(331) surfaces; *Surf. Sci.*, 159: 199–213, 1985.
- [20] D. N. Belton, C. L. DiMaggio and K. Y. S. Ng; N + N → N<sub>2</sub> reaction rates on Rh(111); *J. Catal.*, 144: 273–284, 1993.
- [21] Martijn van Hardeveld; *Elementary reactions in the catalytic reduction of NO on rhodium*

- surfaces*; PhD thesis, Eindhoven University of Technology, 1997.
- [22] R. M. van Hardeveld, R. A. van Santen and J. W. Niemantsverdriet; Formation of  $\text{NH}_3$  and  $\text{N}_2$  from atomic nitrogen and hydrogen on rhodium(111); *J. Vac. Sci. Tech. A*, 15(3): 1558–1562, 1997.
- [23] T. Zambelli, J. Winterlin, J. Trost and G. Ertl; Identification of the “active sites” of a surface-catalyzed reaction; *Science*, 273: 1688–1690, 1996.
- [24] H. Xu and K. Y. S. Ng; Molecular NO islands versus O and N islands on Rh(111) surface studied by scanning tunneling microscopy; *Surf. Sci.*, 365: 779–788, 1996.
- [25] PLATYPUS is an optimisation program for problems that can be handled by Genetic Algorithms (GA) or Evolutionary Strategies (ES). It is written in C++ by A. P. J. Janssen.
- [26] H.-P. Schwefel; *Evolution and optimum seeking*; Sixth generation computer technology series. John Wiley & Sons, 1995.
- [27] W. Spendley, G. R. Hext and F. R. Himsforth; Sequential application of simplex designs in optimisation and evolutionary operation; *Technometrics*, 4(4): 441–461, 1962.
- [28] J. P. M. Andries and A. B. de Vries; *Chemometrie*; Bohn Stafleu Van Loghum (te Houten), 1998.
- [29] P. B. Ryan, R. L. Barr and H. D. Todd; Simplex techniques for nonlinear optimization; *Anal. Chem.*, 52: 1460–1467, 1980.
- [30] J. Trost, T. Zambelli, J. Winterlin and G. Ertl; Adsorbate-adsorbate interactions from statistical analysis of STM images: N/Ru(0001); *Phys. Rev. B*, 54(24): 17850–17857, 1996.
- [31] V. P. Zhdanov; Simulation of kinetics of nitrogen desorption from Rh(111); *Catal. Lett.*, 37: 163–165, 1996.
- [32] B. Meng and W. H. Weinberg; Theoretical and simulation studies of recombinative temperature programmed desorption; *J. Chem. Phys.*, 102(2): 1003–1013, 1995.
- [33] D. Loffreda, D. Simon and P. Sautet; Molecular and dissociative chemisorption of NO on palladium and rhodium (100) and (111) surfaces: A density-functional periodic study; *J. Chem. Phys.*, 108(15): 6447–6457, 1998.



138 REFERENCES

## CHAPTER 7

# CONCLUDING REMARKS

### 7.1 ACHIEVEMENTS

We successfully modelled the effects of lateral interactions for several adsorbate-on-metal-surface systems. We explained the formation of the two experimentally observed ordered structures for the system of NO on Rh(111). Moreover, we explained that the occupation of top sites next to threefold sites at higher coverages was due to lateral interactions. Finally, we reproduced the suppression of the NO dissociation reaction in the presence of its dissociation products.

For the system of (*R,R*)-bitartrate on Cu(110) we were able to demonstrate that the lateral interactions are in part direct and in part through-surface. The direct interactions cause the ordered structure formed to be chiral for this molecule. A adsorption-induced stress along the copper rows results in empty troughs in the ordered structure for (*R,R*)-bitartrate. This adsorption-induced stress also explains the formation of empty-trough ordered structures for similar molecules like acetic and succinic acid.

For the system of the bridge-bound anion on a fcc(111) metal surface we found two peaks in linear sweep voltammetry. These two peaks correspond to adsorption in a disordered phase and a disorder-order transition in the adlayer. The shape of these peaks is greatly influenced by the presence of lateral interactions, changing the sweep rate, the presence of defects in the surface and the way the anion is discharged on the surface.

For the system of nitrogen recombination at step defects on Rh(111), we found that lateral interactions play a very important role. This is particularly clear from the multi-isotherm desorption experiments we compare our models to. These multi-isotherm experiments are temperature-programmed desorption experiments, in which the temperature is kept constant for some time, after which the temperature is increased in a stepwise (or semi-stepwise) fashion to a higher value. This is repeated until desorption is complete. By using an Evolutionary Strategy-type optimisation algorithm we were able to extract physically reasonable kinetic parameters from an experimentally measured multi-isotherm.

## 7.2 SHORTCOMINGS

In the methodology section we stated that by using the lattice-gas approximation we can circumvent inclusion of the fast internal motions of the molecules. This facilitates a description of our systems for much larger time scales. As a result, we found that there are processes occurring on the surface that differ significantly in time scale. Specifically, diffusion of the adsorbates is much faster than a reaction of the adsorbates in most cases. Here a reaction can be anything: adsorption, dissociation, recombination or desorption. The time scale for diffusion typically is in the range of milliseconds to microseconds, whereas the reactions (and thus the overall experiment) take place on the scale of seconds to minutes. The reason why diffusion is much faster than a typical reaction is that the activation energy barrier for moving to another site is much smaller than for a ‘real’ chemical reaction, where bonds are broken. A simulation of adsorbates on surfaces therefore mainly consists of moving adsorbates around on the surface, while only occasionally a reaction takes place. In practice we can argue that the adlayer is fully equilibrated by means of diffusion during the time between two subsequent chemical reactions. In our simulations we make use of this property to reduce the diffusion rate constant: we fix it to a certain value smaller than the original one. This is a proper procedure as long as the adlayer is still fully equilibrated between two subsequent reactions. One can estimate whether the adlayer is equilibrated by checking the ratio of the time scales for diffusion and reactions, or by increasing the diffusion rate in the simulations and checking whether the results change. Since we reduce the number of events we have to describe in our simulations by reducing the diffusion rate constant, we reduce the otherwise significant computational cost.

The defining property of a lattice-gas model is that the adsorbates are fixed to a certain site. This is a good approximation at low coverages. At high coverages this can create a problem. Adsorbates can only diffuse around in a lattice-gas model if a neighbouring site is empty and accessible. Adsorbates can not simply shift a little to allow other adsorbates to pass by at some penalty; either they can pass, or they can't. This causes the adlayer to be frozen in at high coverages: all the adsorbates are fixed to their positions and none can move. On the other hand, bonding to less favourable sites and other adsorption geometries of the molecule do allow diffusion even at high coverages. We encountered this complication for the case of NO on Rh(111). In this case inclusion of bridge-bound NO helps diffusion at coverages close to saturation. For the case of (*R,R*)-tartaric acid on Cu(110), we also saw a significant reduction in the diffusion rate at high coverages. A different adsorption geometry (e.g., diagonally across two copper rows) might circumvent this. Extending the model in such a way helps us prevent the adlayer from becoming frozen in at high coverages, but it has the severe drawback that it requires more complicated –and therefore less reliable– interaction potentials.

### 7.3 QUESTION MARKS

“You ought to worry about the potentials and models you use –and if you already do, you should worry *more*.” The reality of a Monte Carlo model is the consequence of a number of choices and approximations. Depending on how good these choices are, the model may resemble ‘the real world’ very strongly. Even if the model chosen has nothing in common with reality, it may fit the experiment nicely. John Harding’s entering remark\* on this subject clearly warns against accepting that everything a model produces is true.

We made a great effort to make our potentials reliable. We extensively describe each model, and we relate the choices that define our models to the relevant literature available. Where possible we have used kinetic parameters derived from experiments or electronic structure calculations. If the parameters were not known in advance, we obtained them using a robust fitting algorithm. Finally we tried to keep the models simple. The different models each display a certain level of intricacy, by having a certain number of accessible sites, a certain number interactions and the presence or absence of defects in the surface. The main simplifying factors in the model for NO on Rh(111) are that, although different sites and many interactions are used, the molecules are simple, and the interactions are isotropic. In the model for (*R,R*)-tartaric acid adsorption, the molecule is complicated, but restricted to only one adsorption geometry. This still makes estimation of the interactions possible. For the case of sulfate adsorption under electrochemical conditions, there is much speculation on the atomic detail. The model anion described in that chapter will therefore remain just that –a *model* anion. As regards the final study of nitrogen on Rh(111), we only have one simple adsorbate, which takes part in a well-studied reaction. This allows us to study the interactions in great detail.

Adsorbate-induced surface reconstructions will instantly invalidate most of the assumptions made in our models. Such reconstructions have been reported for high coverages of nitrogen and oxygen on Rh(111), for high coverages of acetic and formic acid (but not tartaric acid) on Cu(110), and for (bi)sulfate on Cu(111). For the low coverages of atomic species (less than half a monolayer) treated in our models we do expect to be safe from reconstructions, however.

### 7.4 FINAL THOUGHTS

The different models presented in this thesis aimed to improve our understanding of some well-defined experiments probing model catalyst surfaces. We have found that the ideal lattice gas picture with adsorption, diffusion, reaction, and desorption has its shortcomings. The interactions between the molecules greatly influence the behaviour of these systems. The lateral interactions may decrease a reaction rate, as for the case of NO dissociation, or increase it, as for the case of recombinative desorption

---

\*J. H. Harding, University College London, during the CCP5 Methods in Molecular Simulation Summer School 2003 at King’s College London

of nitrogen. The effect of lateral interactions on a reaction rate is also seen for the electrochemical case of anion adsorption, where lateral interactions strongly influence the shape of the voltammogram. Furthermore, these interactions can cause the adsorbates to order into islands, as shown for NO on Rh(111), and (*R,R*)-tartaric acid on Cu(110). Finally, the need to reduce interaction energies can cause the occupation of a more weakly bonding second type of adsorption site. We saw and modelled this for NO on Rh(111), which occupies top sites next to threefold sites at higher coverages. This shows how important the structure of the adlayer is for the kinetics of the adlayer. While lateral interactions are often masked in a conventional TPD, their effect is much more visible when conducting a multi-isotherm experiment. Reporting multi-isotherms next to the classical TPDs would therefore greatly improve the insight into whether adsorbate-adsorbate interactions are present in the experimental adlayer and in which coverage ranges.

If these lateral interactions are accounted for, as in our case in a lattice-gas kinetic Monte Carlo model, then most of the effects seen for the experimental systems can be explained. One may also use these models to make an educated guess at the outcome of similar experiments, or to investigate the possibility of different reaction mechanisms. Therefore the logical extension for describing experimental behaviour of adsorbates on surfaces lies in the inclusion of adsorbate-adsorbate interactions. This cannot be achieved using classical rate equations, but is very well feasible with kinetic Monte Carlo modelling, as shown by the examples in this thesis. An essential requirement in building these more detailed models is to provide enough information from other techniques to base this model on; if this information is not available the kinetic Monte Carlo model can not add any useful insight. Multi-technique studies and joint research of experimentalists and theoreticians are thus required to further elucidate the behaviour of adsorbates on surfaces.

# SUMMARY

In this thesis we analyse the effects of lateral adsorbate-adsorbate interactions on the properties of adsorbates on surfaces. Our models are based on the lattice-gas approximation; the evolution of our systems with time is described by means of a kinetic Monte Carlo algorithm. The lateral interactions can be decomposed into a hard contribution, since bonding to neighbouring sites is excluded for small adsorbate-adsorbate distances, and a soft contribution, in the form of an energetical penalty. This penalty corresponds to the reduction in binding energy of the adsorbate due to other adsorbates present. The kinetic Monte Carlo algorithm uses a set of rate constants to generate a time evolution of the system. The lateral interactions are accounted for by taking values of these rate constants that depend on the occupation of neighbouring sites. The values of the rate constants are then determined by means of the Brønsted-Evans-Polanyi relationship, which relates the energetical penalty due to bonding of neighbouring adsorbates to a change in the rate constant.

In the first model we describe how lateral interactions cause NO molecules to form ordered structures on the Rh(111) surface, and we describe how they force NO to occupy top sites next to threefold sites at higher coverages. We also show that at intermediate coverages lateral interactions suppress the dissociation of NO into nitrogen and oxygen atoms. The values for the different interactions and the binding energies for the different sites were estimated using electronic structure calculations, and then implemented in the kinetic Monte Carlo model. This system is of interest since rhodium particles are widely used to reduce NO emissions from car exhaust gases.

In the second model we describe how a large molecule, in this case (*R,R*)-tartaric acid, orders on the Cu(110) surface. The ordering is due to a combination of direct and through-surface interactions. The direct interactions are caused by hydroxyl groups of neighbouring adsorbed (*R,R*)-tartaric acid molecules interacting. These interactions have a low (but specific) symmetry and the ordered structure formed hence is chiral. The overall high symmetry of the surface and its reactive sites is thus reduced upon adsorption of (*R,R*)-tartaric acid. The values for the different interactions were estimated using electronic structure calculations. The fact that the symmetry of the surface is broken by adsorbing (*R,R*)-tartaric acid is exciting, since it may provide a way to perform enantio-selective catalysis on ‘ordinary’ heterogeneous catalysts.

In the third model we describe the adsorption of a bridge-bound anion on an

fcc(111) metal surface under electrochemical conditions. For this case we have shown that depending on the nature of the anion, the nature of the surface and the nature of the interactions between the anions, one has different kinetics of adsorption. In electrochemistry one can obtain a quantitative measure of the adsorption kinetics by measuring the current through the electrode. A comparison of the model's adsorption kinetics to experimental data therefore is possible. The model described here bears many similarities to adsorption from sulfuric acid solutions onto metal (111) surfaces. This has been extensively studied experimentally since perchloric acid and sulfuric acid are the main electrolytes in use.

In the last model we revisited the system of NO on Rh(111), and only focused on the recombinative desorption of nitrogen. Though conventional temperature-programmed desorption traces of this reaction are easily reproduced using an Arrhenius-type rate constant, this is not the case for other temperature programs. We show that for such a more informative temperature program, referred to as multi-isotherm, the presence of lateral interactions is immediately revealed. We also show that a more elaborate model including lateral interactions is required to correctly model these multi-isotherms. Since many interactions are present, these were fitted with an Evolutionary Strategy-type optimisation algorithm.

The overall picture of these systems is that lateral interactions have a large influence on the adsorption, desorption, reaction, site occupation and ordering of the adsorbates. Though modelling these interactions requires significant effort, explicit inclusion of these interactions is required to gain more insight into the behaviour of adsorbates on surfaces.

# SAMENVATTING

In dit proefschrift analyseren we het effect van laterale adsorbaat-adsorbaat interacties op de eigenschappen van adsorbaten op oppervlakken. Onze modellen zijn gebaseerd op de roostergasbenadering en de ontwikkeling van deze systemen in de tijd wordt beschreven door een kinetisch Monte Carlo algoritme. De laterale interacties kunnen worden opgedeeld in een harde component, aangezien het binden aan naburige adsorptieplekken uitgesloten is voor kleine adsorbaat-adsorbaat afstanden, en een zachte component, in de vorm van een energetische straf. Deze straf correspondeert met de vermindering van de bindingsenergie van het adsorbaat door de aanwezigheid van andere adsorbaten. Het kinetisch Monte Carlo algoritme gebruikt een set reactiesnelheidsconstanten om de tijdsontwikkeling van het systeem te genereren. De laterale interacties worden meegenomen in de simulaties door de waarden van deze reactiesnelheidsconstanten afhankelijk te maken van het al dan niet bezet zijn van naburige adsorptieplekken. De waarden van de reactiesnelheidsconstanten worden dan bepaald door middel van de Brønsted-Evans-Polanyi vergelijking, die de energetische straf door het binden van naburige adsorbaten relateert aan een verandering in de reactiesnelheidsconstante.

In het eerste model beschrijven we hoe laterale interacties NO moleculen geordende structuren doen vormen op het Rh(111) oppervlak. We beschrijven hoe laterale interacties bij hoge bedekkingsgraden NO dwingen ook bindingsplekken bovenop metaalatomen te bezetten, terwijl ze bij lage bedekkingsgraden alleen op bindingsplekken tussen drie metaalatomen gebonden zitten. We laten ook zien dat bij tussenliggende bedekkingsgraden laterale interacties de dissociatie van NO in stikstof- en zuurstofatomen onderdrukken. De waarden voor de verschillende interacties en de bindingsenergieën voor de verschillende bindingsplekken worden eerst afgeschat door gebruik te maken van elektronenstructuurberekeningen en vervolgens geïmplementeerd in het kinetisch Monte Carlo model. Dit systeem is interessant aangezien rhodium deeltjes veel gebruikt worden om de uitstoot van NO in autouitlaatgassen terug te brengen.

In het tweede model beschrijven we hoe grote moleculen, van in dit geval (*R,R*)-wijnsteenzuur, ordenen op het Cu(110) oppervlak. De ordening wordt veroorzaakt door een combinatie van directe interacties tussen de moleculen en interacties die door het oppervlak heen gaan. De directe interacties worden veroorzaakt door hydroxylgroepen van naburige geadsorbeerde (*R,R*)-wijnsteenzuurmoleculen die elkaar



afstoten. Deze interacties hebben een lage (maar specifieke) symmetrie en de geordende structuur die gevormd wordt is daardoor chiraal. De hoge symmetrie van het hele oppervlak met zijn reactieve bindingsplekken is dus verlaagd door adsorptie van (*R,R*)-wijnsteenzuur. De waarden voor de verschillende interacties worden afgeschat door gebruik te maken van elektronenstructuurberekeningen. Het feit dat de symmetrie van het oppervlak gebroken wordt door (*R,R*)-wijnsteenzuur te adsorberen is spannend aangezien het een manier kan zijn om enantioselectieve katalyse uit te voeren met conventionele heterogene katalysatoren.

In het derde model beschrijven we de adsorptie van een anion dat onder elektrochemische omstandigheden bruggend tussen twee metaalatomen bindt aan een fcc(111) metaaloppervlak. We laten voor dit geval zien dat men, afhankelijk van de aard van het anion, de aard van het oppervlak en de aard van de interacties tussen de anionen, een andere adsorptiekinetiek krijgt. In de elektrochemie is het mogelijk een kwantitatieve maat voor de adsorptiekinetiek te krijgen door de elektrische stroom door de elektrode te meten. Een vergelijking van de adsorptiekinetiek die we hebben gevonden voor ons model met experimentele resultaten is hierdoor mogelijk. Het model dat we hier beschrijven blijkt veel overeenkomsten te hebben met de adsorptie van anionen uit zwavelzuuroplossingen op metaal (111) oppervlakken. Dit is experimenteel uitgebreid bestudeerd aangezien perchloorzuur en zwavelzuur de meest gebruikte elektrolyten zijn.

In het laatste model hebben we het systeem van NO op Rh(111) opnieuw ter hand genomen en alleen gekeken naar de recombinatieve desorptie van stikstof. Hoewel conventionele temperatuurgeprogrammeerde desorptie resultaten voor deze reactie makkelijk gereproduceerd kunnen worden, is dit niet het geval voor andere, meer complexe, temperatuurprogramma's. We laten zien dat uit zo een meer informatief temperatuurprogramma, waarnaar we verwijzen als multi-isotherm, de aanwezigheid van laterale interacties meteen duidelijk is. We maken ook duidelijk dat een model met laterale interacties nodig is om deze multi-isothermen op een juiste manier te modelleren. Aangezien er veel interacties aanwezig zijn, zijn ze benaderd met een optimalisatiealgoritme van het type Evolutionaire Strategie.

Het overkoepelende beeld dat deze modellen geven is dat laterale interacties een grote invloed hebben op de adsorptie, desorptie, reactie, de bezetting van bindingsplekken en de ordening van adsorbaten. Hoewel het modelleren van dergelijke interacties een behoorlijke inspanning vereist, is het nodig interacties in het model mee te nemen om een goed inzicht te krijgen in het gedrag van adsorbaten op oppervlakken.

# LIST OF PUBLICATIONS

- C. G. M. Hermse, A. P. van Bavel, M. T. M. Koper, J. J. Lukkien, R. A. van Santen and A. P. J. Jansen; Modelling the butterfly:  $(\sqrt{3} \times \sqrt{7})$  ordering on fcc(111) surfaces; *Surf. Sci.*, accepted for publication, 2004.
- C. G. M. Hermse, A. P. van Bavel, A. P. J. Jansen, L. A. M. M. Barbosa, P. Sautet and R. A. van Santen; Formation of chiral domains for tartaric acid on Cu(110): a combined DFT and kinetic Monte Carlo study; *J. Phys. Chem. B* 108 (30): 11035–11043, 2004.
- A. P. van Bavel, C. G. M. Hermse, M. J. P. Hopstaken, A. P. J. Jansen, J. J. Lukkien, P. A. J. Hilbers and J. W. Niemantsverdriet; Quantifying lateral adsorbate interactions by kinetic Monte-Carlo simulations and density-functional theory: NO dissociation on Rh(100); *Phys. Chem. Chem. Phys.* 6 (8): 1830–1836, 2004.
- C. G. M. Hermse, F. Frechard, A. P. van Bavel, J. J. Lukkien, J. W. Niemantsverdriet, R. A. van Santen and A. P. J. Jansen; Combining density-functional calculations with kinetic models: NO/Rh(111); *J. Chem. Phys.* 118 (15): 7081–7089, 2003.
- M. T. M. Koper, N. P. Lebedeva and C. G. M. Hermse; Dynamics of CO at the solid/liquid interface studied by modeling and simulation of CO oxidation on Pt and PtRu electrodes; *Faraday Discuss.* 121: 301–311, 2002.
- C. G. M. Hermse and A. P. J. Jansen; Optimal structure of bimetallic catalysts for the A+B<sub>2</sub> reaction; *Surf. Sci.* 461 (1–3): 168–176, 2000.
- A. P. J. Jansen and C. G. M. Hermse; Optimal structure of bimetallic catalysts for the A+B reaction; *Phys. Rev. Lett.* 83 (18): 3673–3676, 1999.

148 LIST OF PUBLICATIONS

# DANKWOORD

Aan de oer-theoreten: Xavier en Luis, toen ik de groep binnenkwam zaten jullie daar al 's ochtends vroeg, met een mok koffie geschaard rond de sgi's. Ondertussen is er menig koffiezetapparaat gesneuveld, maar koffie wordt er nog elke morgen gedronken door een volgende en dáárop volgende generatie: Rob, Joyce, Joost, Bouke, Cristina, Adelaida en Sander. Het was en is nog steeds erg gezellig om zo wakker te worden en na te praten over elk bezoek aan Ef, Traf, Euro of Plaza.

Op sportief gebied vallen de poolprestaties in Lunteren en Eindhoven op. Velitchka, Paul, Peter en Alexey, samen hebben we bewezen dat topsport op een volle maag wel degelijk kan.

In Han zat ik op de een of andere manier altijd aan die luidruchtige tafel met de lege flessen, maar wel in uitstekend gezelschap, met jullie, Jeroen, Joost, Mark, Gé, Mirjam en Meta. Rikken was er altijd gezellig, en misschien vegen jullie dit jaar wel de vloer aan met die Vlamingen bij Machiavelli.

Verder wil ik ook alle andere theoreten aanhalen, ook al waren de meesten van jullie al lang klaar tegen de tijd dat ik halverwege was. Willy, Ojwang, Hiroshi, David, Rafael, Erik, Ionel, Danny, Robin, Eric en Ronald, bedankt.

Aan iedereen met wie ik tegenover gedrochten in imaginaire kelders heb gestaan: ik heb me rotgelachen, en als een zorvuldig uitgedacht plan weer eens meteen in duigen valt kun je er altijd nog heel hard op af stormen. Wouter, Peter, Roelant, Sander, Mark en Arnoud, en Bart, Maurice, Petra, Raf en Geralda, en Jeroen en Simon, doe maar even dobbelen.

Veel dank aan alle vaste koffie-, borrel- en colloquiumgangers: Jos, Thijs, Marije, Vincent, Eric, Michiel, Mabel, Eero, Ruben, Niek, Jarl, Tiny, Christoph, Christophe, Zhu en Gijsbert, door jullie overduidelijke aanwezigheid staat de sfeer binnen de groep nog steeds als een huis.

De gezellige potpourri die nu mijn proefschrift heet dank ik aan samenwerkingen met veel mensen. Frédéric, Hans, Luis, Philippe, Marc, Tom, Ben, Johan en Sander: dit boekje is jullie schuld. Tonek, heel hartelijk bedankt voor je onvoorwaardelijke steun en altijd precieze correcties door de jaren heen. Rutger, bedankt voor de interesse die je tussen alle bedrijven door toch altijd weer toont.

150 DANKWOORD

# CURRICULUM VITAE

Chrétien Hermse werd op 25 Juli 1977 geboren te Maastricht. Nadat hij daar aan het Trichter College in 1995 het VWO-diploma behaalde, begon hij aan de Technische Universiteit Eindhoven met de studie Scheikundige Technologie. In 2000 studeerde hij af in de capaciteitsgroep Anorganische Chemie en Katalyse. Daarop trad hij in dienst van de Technische Universiteit Eindhoven om zijn promotie-onderzoek, beschreven in dit proefschrift, uit te voeren.